AD NUMBER

AD915551

LIMITATION CHANGES

TO:

Approved for public release; distribution is unlimited.

FROM:

Distribution authorized to U.S. Gov't. agencies only; Test and Evaluation; DEC 1973. Other requests shall be referred to Air Force Propulsion Lab., Wright-Patterson AFB, OH 45433.

AUTHORITY

USAEDC ltr 9 Jan 1981

AN INVESTIGATION OF MODEL SCALING EFFECTS AT MACH NUMBERS FROM 0.60 TO 1.40

David E. A. Reichenau
ARO, Inc.

PROPULSION WIND TUNNEL FACILITY
ARNOLD ENGINEERING DEVELOPMENT CENTER
AIR FORCE SYSTEMS COMMAND
ARNOLD AIR FORCE STATION, TENNESSEE 37389

December 1973

Final Report for Period 13 March – 21 July, 1973

Prepared for

AIR FORCE PROPULSION LABORATORY (TBA)
WRIGHT-PATTERSON AFB, OH 45433

NOTICES

When U. S. Government drawings specifications, or other data are used for any purpose other than a definitely related Government procurement operation, the Government thereby incurs no responsibility nor any obligation whatsoever, and the fact that the Government may have formulated, furnished, or in any way supplied the said drawings, specifications, or other data, is not to be regarded by implication or otherwise, or in any manner licensing the holder or any other person or corporation, or conveying any rights or permission to manufacture, use, or sell any patented invention that may in any way be related thereto.

Qualified users may obtain copies of this report from the Defense Documentation Center.

References to named commercial products in this report are not to be considered in any sense as an endorsement of the product by the United States Air Force or the Government.

APPROVAL STATEMENT

This technical report has been reviewed and is approved.

Lamar R. Kissling

LAMAR R. KISSLING
Lt Colonel, USAF
Chief Air Force Test Director, PWT
Directorate of Test

Frank J. Passarello

FRANK J. PASSARELLO
Colonel, USAF
Director of Test

UNCLASSIFIED

SECURITY CLASSIFICATION OF THIS PAGE *(When Data Entered)*

REPORT DOCUMENTATION PAGE		READ INSTRUCTIONS BEFORE COMPLETING FORM
1. REPORT NUMBER AEDC-TR-73-202	2. GOVT ACCESSION NO.	3. RECIPIENT'S CATALOG NUMBER
4. TITLE *(and Subtitle)* AN INVESTIGATION OF MODEL SCALING EFFECTS AT MACH NUMBERS FROM 0.60 TO 1.40		5. TYPE OF REPORT & PERIOD COVERED Final Report-13 to 24 March 1973 6. PERFORMING ORG. REPORT NUMBER
7. AUTHOR(s) David E. A. Reichenau		8. CONTRACT OR GRANT NUMBER(s)
9. PERFORMING ORGANIZATION NAME AND ADDRESS Arnold Engineering Development Center Arnold Air Force Station, Tennessee 37389		10. PROGRAM ELEMENT, PROJECT, TASK AREA & WORK UNIT NUMBERS Program Element 63202F System 668A
11. CONTROLLING OFFICE NAME AND ADDRESS Air Force Propulsion Laboratory Wright-Patterson AFB, OH 45433		12. REPORT DATE December 1973 13. NUMBER OF PAGES 132
14. MONITORING AGENCY NAME & ADDRESS*(if different from Controlling Office)*		15. SECURITY CLASS. *(of this report)* UNCLASSIFIED 15a. DECLASSIFICATION DOWNGRADING SCHEDULE N/A

16. DISTRIBUTION STATEMENT *(of this Report)*

Distribution limited to U.S. Government agencies only; this report contains information on test and evaluation of military hardware; December 1973; other requests for this document must be referred to Air Force Propulsion Laboratory (TBA), Wright-Patterson AFB, OH 45433.

17. DISTRIBUTION STATEMENT *(of the abstract entered in Block 20, if different from Report)*

18. SUPPLEMENTARY NOTES

Available in DDC.

19. KEY WORDS *(Continue on reverse side if necessary and identify by block number)*

model tests	pressure drag	boundary-layer flow
subsonic flow	F-15 aircraft	
transonic flow	Reynolds number	

20. ABSTRACT *(Continue on reverse side if necessary and identify by block number)*

Wind tunnel investigations of three scale models were conducted to determine the effects of model scaling in the subsonic and transonic flow regimes. The models were 4.7-, 13-, and 17-percent scale F-15 fighter equivalent body models. The data were obtained at Mach numbers from 0.60 to 1.40 and free-stream Reynolds numbers from 1.0 to 5.3 x 10^6 for model angles of attack from 0 to 5 deg. The results show that at subsonic Mach

DD FORM 1 JAN 73 1473 EDITION OF 1 NOV 65 IS OBSOLETE

UNCLASSIFIED

SECURITY CLASSIFICATION OF THIS PAGE *(When Data Entered)*

20, Continued

numbers the zero-lift pressure drag coefficient of the basic configurations was a function of Reynolds number and Mach number. However, the pressure drag coefficient for the fuselage-alone configuration and the alternate wing configuration was essentially invariant with Mach number for Mach numbers below 0.90. The data obtained with the cylindrical afterbody model and integrated aft-end pressure drag increments show that the transonic interference resulting from model size was primarily confined to the contoured fuselage afterbody.

PREFACE

The work reported herein was conducted by the Arnold Engineering Development Center (AEDC), Air Force Systems Command (AFSC), under sponsorship of the Air Force Propulsion Laboratory (AFAPL/TBA), Wright-Patterson Air Force Base, Ohio, for the McDonnell Douglas Corporation. The results presented were obtained by ARO, Inc. (a subsidiary of Sverdrup & Parcel and Associates, Inc.), contract operator of AEDC, AFSC, Arnold Air Force Station, Tennessee. The work was done under ARO Project No. PA050, and the manuscript (ARO Control No. ARO-PWT-TR-73-140) was submitted for publication on October 26, 1973.

CONTENTS

ILLUSTRATIONS

Figure Page

Figure | Page

Figure Page

TABLE

1.0 INTRODUCTION

Wind tunnel investigations of three scale models were conducted in the AEDC Propulsion Wind Tunnel (16T) at Mach numbers from 0.60 to 1.40 and free-stream Reynolds numbers from 1.0 to 5.3 x 10^6 at angles of attack from 0 to 5 deg. The purpose of these tests was to determine the effects of model scaling in the subsonic and transonic flow regimes. The models were 4.7-, 13-, and 17-percent scale F-15 equivalent body models. The basic models had a body-of-revolution fuselage and constant-thickness wings with a scale F-15 planform.

In addition to the primary objective of determining the effect of model size on force and moment characteristics and on model pressure distributions, several related investigations were conducted to evaluate test conditions and flow phenomena which could influence the model scaling results. These included evaluation of boundary-layer characteristics, transition grit effects, support sting effects, and Reynolds number effects. In addition, the investigation included testing all the models with a cylindrical afterbody and also with the wings removed. Also, the 4.7- and 17-percent scale models were tested with an alternate wing configuration.

2.0 APPARATUS

2.1 TEST FACILITY

Tunnel 16T is a closed-circuit, continuous flow wind tunnel capable of operation at Mach numbers from 0.2 to 1.60. The test section is 16 by 16 ft in cross section and 40 ft long. The tunnel can be operated within a stagnation pressure range from 120 to 4000 psfa, depending on Mach number. Stagnation temperatures can be varied from an average minimum of about 80°F to a maximum of 160°F. Perforated walls in the test section allow continuous operation through the Mach number range with a minimum of wall interference. A more detailed description of the test facility is presented in the Test Facilities Handbook, Ref. 1. A sketch showing the model location in the test section is presented in Fig. 1.

2.2 TEST ARTICLES

2.2.1 Basic Models

Three scale body-of-revolution models were used in this investigation. The total area distribution of each model, body plus wings, approximated the scaled area distribution of the F-15 aircraft configuration including wings, tail surfaces, inlet fairings, and low Mach

number afterburning nozzles with cylindrical exhaust plumes. These models had constant-thickness wings with a planform similar to the F-15 aircraft configuration. The effective scale sizes of the three models, based on model length, were 4.7, 13, and 17 percent. A summary of model geometry is shown in Fig. 2, and a comparison of scale model characteristics is presented in Fig. 3. The normalized area distribution is shown in Fig. 4, and the radius distribution for the 17-percent model is tabulated in Table 1. Photographs of various model installations in Tunnel 16T are shown in Fig. 5.

All three models were sting mounted from the tunnel sting support system. The three stings had the same scale diameter at the exit plane of the models, and this diameter extended downstream for approximately eight sting diameters aft of the model exit plane. Aft of this point, the stings varied in configuration to facilitate using the tunnel sting adapter. An illustration of all three sting/adapter configurations is presented in Fig. 6.

Prior to model fabrication, model tolerances were specified to insure geometric similitude for the three models. A dimensional check verified that the fuselage radius distribution and wing dimensions were within ±0.003, 0.007, and 0.010 in. for the 4.7-, 13-, and 17-percent models, respectively. Inspection of the surface conditions on all of the models indicated surface finishes ranging between 8 and 14 microinches.

2.2.2 Fuselage

The axisymmetric fuselage of each model was constructed of aluminum, and each body had milled slots to accept the wings. When the models were tested with wings off, wing slot fillers were used as shown in Fig. 5e. The basic fuselage of each model had a contoured aft end, as shown in the model area distribution of Fig. 4. Cylindrical afterbodies were also made for each of the three models. These afterbodies altered the model area distribution as shown in Fig. 4. Each cylindrical afterbody consisted of two aluminum clamshells which were bolted onto the basic model afterbody. The cylindrical afterbody on the 4.7-percent scale model is shown in Fig. 5d.

2.2.3 Wings

The basic aluminum wings for each model had a semicircular leading edge and a 5-deg included taper angle on the trailing edge, as shown in Fig. 2. The wings were attached at the mid-wing position on each fuselage. The incidence angle between the wings and the fuselage axis was zero.

An alternate wing configuration was constructed for the 4.7- and 17-percent scale models. The alternate wing configuration had a planform identical to that of the basic

wing configuration and had a 12-deg included wedge angle on the leading edge instead of a semicircular leading edge. A sketch of the alternate wing configuration is shown in Fig. 3.

2.2.4 Boundary-Layer Rakes

Two boundary-layer rakes were mounted on both the 4.7- and the 17-percent scale model for a limited portion of the investigation. The wing rakes were mounted on the trailing edge at the mean aerodynamic chord, and the fuselage rakes were mounted on the top centerline at X/L = 0.70. In addition, to investigate boundary-layer separation, limited testing was accomplished on the 13-percent scale model using rakes from the 4.7-percent scale model. One rake was mounted on the fuselage top centerline at the base of the model, and the other was mounted on the wing trailing edge at the mean aerodynamic chord. The locations of the boundary-layer rakes for all three models are shown in Fig. 7. Each rake contained nine total pressure probes. The total pressure probe locations are presented in Fig. 8.

2.3 INSTRUMENTATION

The three model configurations were mounted on six-component strain-gaged balances to measure the model aerodynamic loads. Model angle of attack was measured by an internally mounted angular position indicator. A scanivalve assembly was used to measure the model surface and base pressures.

The 4.7- and 17-percent models each had 38 surface and 4 base pressure taps. The 13-percent model had 60 surface and 4 base pressure taps. All the surface taps were flush mounted. The locations of these taps are shown in Fig. 9. When each of the cylindrical afterbodies was installed, the aft surface pressure taps were used to measure "base" pressures for this configuration. This arrangement is shown in Fig. 10.

The 4.7- and 17-percent models used one 48-port scanivalve module with a 5-psid transducer. The 13-percent model used two 48-port scanivalve modules with 5-psid transducers.

Each sting was equipped with static pressure taps adjacent to the balance to measure model cavity pressures. In addition, pressure taps were located on the top centerline of the sting to measure the surface pressure distributions. The sting pressure tap locations shown in Fig. 11 correspond to positions 0, 0.5, 1.0, 1.5, 2.0, and 2.5 model base diameters downstream of the model.

The sting and cavity pressures were measured using 5-psid transducers. The boundary-layer rake total pressures were measured using 15-psid transducers. Static pressures from the stings and model cavities were referenced to the tunnel plenum pressure, and total pressures from the rakes were referenced to the tunnel total pressure.

Electrical signals from the balances, pressure transducers, position indicators, and tunnel instrumentation outputs were digitized and stored on magnetic tape as well as fed to a Raytheon 520 computer for on-line data reduction. Force, moment, and pressure data were also graphically displayed on a Cathode Ray Tube (CRT) during the test for on-line evaluation of data integrity.

3.0 PROCEDURE AND PRECISION OF MEASUREMENTS

3.1 GENERAL

The data presented in this report were obtained at nominal free-stream Mach numbers of 0.6, 0.7, 0.8, 0.9, 0.95, 1.00, 1.05, 1.10, 1.20, and 1.40 at free-stream Reynolds numbers from 1.00×10^6 to 5.3×10^6 per foot. The basic model configurations and most of the alternate configurations were tested at the same characteristic Reynolds number, Re_L, based on model length. For sonic and lower Mach numbers, the nominal testing condition was a constant $Re_L = 16 \times 10^6$. At higher Mach numbers, limitations precluded testing at $Re_L = 16 \times 10^6$ with the 4.7-percent scale model. Therefore, the highest characteristic Reynolds number which was achievable while testing the 4.7-percent scale model was used to determine the nominal characteristic Reynolds number schedule supersonically. The nominal characteristic and unit Reynolds number schedule as a function of Mach number is presented in Fig. 12. The angle-of-attack settings were varied from -1 to 5 deg with the 4.7- and 17-percent scale model basic configurations. The 13-percent scale model was tested from 0 to 5 deg angle of attack. Force, moment, and pressure data were obtained simultaneously throughout the test except when the boundary-layer rakes were installed. The pressure instrumentation tubing from the boundary-layer rakes was routed externally along the aft surface of the model, and consequently force, moment, and pressure data were not obtained during this portion of the test.

Boundary-layer transition strips were located on the fuselage nose and on the top and bottom surfaces of the wings for all models. These strips were 0.05 in. wide for the 4.7-percent model and 0.10 in. wide for the 13- and 17-percent models. For most of the testing, the fuselage transition strips were located at 0.75, 2.08, and 2.72 in. aft of the nose on the 4.7-, 13-, and 17-percent models, respectively. The basic wing transition strips were located aft of the leading edge at a distance equal to one half of the wing

thickness. On the alternate wing configurations (4.7- and 17-percent models), the transition strips were located 0.5 and 1.81 in. aft of the wing leading edge on the 4.7- and 17-percent models, respectively. The models were also tested without transition strips for a limited number of runs.

It was necessary to change grit size several times on each model because the test was conducted over a wide range of Reynolds numbers. Figure 13 shows the predicted required grit size as a function of Reynolds number (Ref. 2) for the fuselage transition strip with the circles denoting test configurations. Similar estimates were made for the wing. Grit sizes used during the test were always slightly larger than the estimated requirement.

3.2 DATA REDUCTION

The axial-force coefficients obtained with all model configurations were corrected to account for the pressures acting in the model cavity and on the base. The pressure tare force was calculated by subtracting free-stream static pressure from the average base and cavity pressures and integrating the differential pressures over the aft-projected area. This tare force was then subtracted from the measured axial force. When the cylindrical afterbody was tested, the axial force was also corrected for the differential pressure acting on the base of this afterbody.

Pressure data were integrated over the model afterbody so that aft-end drag increments from all three models could be compared. The area of integration extended from X/L = 0.784 to the base of the fuselage.

Friction drag estimates were made using the Frankl-Voishel skin friction equation (Ref. 3) for a fully turbulent boundary layer. These estimates were made for the fuselage using the characteristic Reynolds number based on model length and for the wings using the chord Reynolds number based on the mean aerodynamic chord. The estimated friction drag levels are shown in Fig. 14 for M_∞ = 0.60 and 1.20. The variation of friction drag with Mach number for the nominal characteristic Reynolds number schedule is shown in Fig. 15. Total model pressure drag was obtained by subtracting the estimated turbulent friction drag from the measured drag.

3.3 PRECISION OF MEASUREMENTS

An estimate of the precision of the data is presented below for Mach numbers 0.60, 0.90, and 1.20. The Taylor Series error propagation procedure was used to determine the precision errors for each model at characteristic Reynolds number conditions.

PRECISION ERROR									
Model, Mach No. / Parameter	4.7-percent Model			13-percent Model			17-percent Model		
	0.60	0.90	1.20	0.60	0.90	1.20	0.60	0.90	1.20
M_∞	±0.002	±0.004	±0.010	±0.002	±0.004	±0.010	±0.002	±0.004	±0.010
p_∞ psfa	±3.00	±3.0	±3.0	±3.0	±3.0	±3.0	±3.0	±3.0	±3.0
q_∞ psf	±3.00	±3.0	±3.0	±3.0	±3.0	±3.0	±3.0	±3.0	±3.0
C_{AF}	±0.0003	±0.0002	±0.0008	±0.0006	±0.0004	±0.0009	±0.0005	±0.0004	±0.0008
C_N	±0.0029	±0.0030	±0.0036	±0.0027	±0.0029	±0.0058	±0.0023	±0.0027	±0.0054
C_m	±0.0036	±0.0088	±0.0198	±0.0016	±0.0022	±0.0072	±0.0103	±0.0164	±0.0044
α	±0.05	±0.05	±0.05	±0.05	±0.05	±0.05	±0.05	±0.05	±0.05

Repeat data were taken periodically throughout the investigation to ensure the data integrity and to determine the data repeatability levels. Model parameter repeatability, judged on the basis of the analysis of these data for the three models, is summarized below.

Parameter	Mach Number		
	0.60	0.90	1.20
C_{AF}	±0.0005	±0.0002	±0.0003
C_N	*	±0.0020*	±0.0040*
C_m	±0.0010	±0.0010	±0.0010
$C_{D_{PAFT}}$	±0.0001	±0.0001	±0.0003*
C_p	±0.0030	±0.0050	±0.0070

The asterisks denote repeatability based on results from the 13- and 17-percent models only. Normal-force coefficient repeatability on the 4.7-percent model was found to be ±0.0090 at M_∞ = 0.90 and 1.20. There were not sufficient data to assess normal-force repeatability at M_∞ = 0.60. Pitching-moment coefficient repeatability for the 4.7-percent model at M_∞ = 1.20 was found to be ±0.004. It is felt that dynamic loadings on the 4.7-percent model were the cause of the poorer normal-force and pitching-moment repeatability. The repeatability numbers listed are applicable throughout the angle-of-attack and Reynolds number conditions for which each model was tested.

4.0 RESULTS AND DISCUSSION

4.1 BOUNDARY-LAYER PROFILES

In order to compare force and pressure data between model scales, it is essential that the geometric similitude and boundary-layer properties be correctly scaled. For this investigation, the geometric similarity was insured by fabricating the models within the tolerances specified in Section 2.2. In order to determine whether the boundary-layer profiles were properly scaled, boundary-layer rake data were obtained at the model locations shown in Fig. 7. The results from the 4.7- and 17-percent scale models are used for comparisons since the data obtained on the 13-percent scale model were limited to the lower portion of the boundary layer and were obtained at a different location on the fuselage.

The individual probe velocities are calculated using the total pressure measured by the probe and the tunnel static pressure. The velocities are ratioed to tunnel free-stream velocity.

The velocity profiles for the models are presented in Fig. 16. These boundary-layer profiles for the fuselage and wing trailing edge on the 4.7- and 17-percent scale models are presented for zero angle of attack. The scaled boundary-layer profiles for the fuselage position of X/L = 0.70 on the 4.7- and 17-percent models agree very well at all Mach numbers. At the wing trailing edge, the boundary layer on the 4.7-percent model is consistently thinner than that on the 17-percent model at the same characteristic Reynolds number. Also presented in Fig. 16 are velocity profiles measured at the trailing edge of the wing on the 13-percent model. Presented in Fig. 17 are velocity profiles measured at the base of the fuselage on the 13-percent model. As was the case for the 4.7- and 17-percent models, the velocity profiles for the 13-percent model do not exhibit inflections at the surfaces and, therefore, do not indicate flow separation at the fuselage base or at the trailing edge of the wing at the mean aerodynamic chord.

The effects of Reynolds number on the 17-percent scale model boundary-layer profiles are shown in Fig. 18. As would be expected at all the Mach numbers shown, the boundary layer becomes thinner with increasing Reynolds number.

4.2 EFFECT OF GRIT SIZE

Various grit sizes were required for transition on the three models. Since the grit size requirements were based on empirical estimates, it was necessary to determine if any

of the drag force was caused by the grit. Reference 4 shows a drag penalty because of grit if the grit height exceeds the boundary-layer height.

The effect of grit size on model drag for the three models at zero angle of attack is shown in Figs. 19 through 21. The estimated required grit size is also noted in each figure. For the basic model configurations, very little effect of grit was observed. This suggested either that the natural transition occurred well forward on the models with the grit off or that the grit did not provide effective transition. To obtain a better understanding of the transition phenomena on these models, an alternate set of wings was investigated on the 4.7- and 17-percent models. These wings were identical in planform to the basic wing configuration; however, instead of a semicircular leading edge, the alternate wing configuration had a 6-deg half-angle wedge leading edge. The data obtained for the alternate wing configuration are shown in Figs. 19 and 21. At subsonic Mach numbers, the drag coefficients increased by as much as 0.0014 and 0.0006 for the 4.7- and 17-percent alternate wing configurations, respectively. The trend with increasing grit size was different for the two models. The drag coefficient increased with increasing grit size on the 4.7-percent model, whereas the drag coefficient remained essentially constant with increasing grit size up to a No. 46 grit size on the 17-percent model. Additional investigation is required in order to better understand the nature of the transition phenomena since the grit study on the basic models and the alternate wing configurations is inconclusive. Insufficient test time was available to make an adequate grit study on the alternate wing configurations.

Throughout the remaining portion of testing the basic configurations, the transition grit sizes were selected based on the estimated grit size shown in Fig. 13. Therefore, it is concluded that for the basic model configurations there is no drag caused by grit size; however, the selected grit size may not have been adequate to trip the boundary layer. The alternate wing configurations were tested in later tunnel entries after the completion of testing the basic model configurations, and repeat data were also obtained for the basic configurations. The repeat data obtained for the 4.7- and 17-percent models are shown in Figs. 19 and 21, respectively.

4.3 ZERO-LIFT DRAG CHARACTERISTICS

4.3.1 Complete Model

Drag coefficient data obtained with the three basic model configurations at zero angle of attack are presented in Fig. 22, and pressure drag coefficient, determined by subtracting the estimated friction drag from the total drag force, is presented in Fig. 23. These data

are compared at the same characteristic Reynolds number at each Mach number. At subsonic Mach numbers, the 13- and 17-percent scale models have higher drag levels than the 4.7-percent model by as much as 13 drag counts (for the 17-percent model). (One drag count = 0.0001 in drag coefficient.) At subsonic Mach numbers, the drag coefficient increased slightly with increasing Mach number for all three models. Transonically, from Mach numbers 1.00 to 1.10, the larger models have substantially lower drag levels, indicating transonic interference effects. At Mach number 1.40, the drag levels for the three basic models are in good agreement.

Drag coefficients obtained with the 4.7- and 17-percent scale models with the alternate wing configurations are compared in Fig. 24. Pressure drag coefficients for the two models are compared in Fig. 25. The data show good agreement at subsonic Mach numbers and, in contrast to the basic configuration, have an essentially constant drag coefficient at Mach numbers from 0.6 to 0.8. The correlation between the 4.7-percent and the 17-percent model, however, may have been a coincidence since the Mach number sweep was made with No. 120 grit on the 4.7-percent model. A larger size grit would have resulted in higher drag, which is the reverse of the trend from the basic wing configuration. Transonically, from Mach numbers 1.00 through 1.10, the 17-percent model has a lower drag level, as was noted for the basic configurations. At Mach number 1.20, the two models were again in good agreement. It may be concluded from these data that the flow properties on the basic model configuration with the blunt leading-edge wing are affected by the viscous flow and the location of the boundaries between the various types of flow (separation, reattachment, transition, and shocks). It is therefore believed that the disagreement in drag obtained at characteristic Reynolds numbers between the basic model configurations is caused primarily by differences in skin friction drag with the blunt leading-edge wing. Unpublished data indicate that the tunnel turbulence is a function of unit Reynolds number and Mach number, and possible separation and reattachment at the wing leading edge would also be largely a function of unit Reynolds number. The consistently thinner boundary-layer profile for the 4.7-percent model shown in Fig. 16 is consistent with the lower drag of this model. The data in Fig. 26 show a comparison between the boundary-layer profiles of the 4.7- and the 17-percent basic model at characteristic Reynolds number, Re_L, and at constant unit Reynolds number, Re. As shown at M_∞ = 0.60, the wing boundary-layer profiles are in good agreement when compared at the same unit Reynolds number. Figures 27 and 28, which present pressure drag coefficient as a function of characteristic Reynolds number and unit Reynolds number, respectively, show that the pressure drag coefficient for the basic models actually correlates better with unit Reynolds number than with characteristic Reynolds number. (The flagged symbols shown in Figs. 27 and 28 represent data taken during the second tunnel entry.) Supersonically, the pressure drag is not a function of Reynolds number; however, there is a difference in pressure drag levels between the small model and the two larger models.

Variation in pressure drag coefficient with unit Reynolds number for the 4.7- and 17-percent models with the alternate wings is shown in Figs. 29 and 30, respectively. The data indicate little effect of Reynolds number on the pressure drag coefficient of the larger model with or without grit with the alternate wings. However, the 4.7-percent alternate wing configuration without transition grit obviously shows extensive laminar flow over the model for the lower unit Reynolds number value at M_∞ = 0.60, resulting in a negative pressure drag coefficient since the skin friction estimates were based on turbulent flow. The increase in pressure drag coefficient with increasing unit Reynolds number is possibly a result of the changing of the flow from laminar to turbulent and/or the inadequacy of the grit to trip the boundary layer at low Reynolds number conditions. There is also the possibility that grit drag may exist at the higher Reynolds number for this model. Additional testing of the 4.7-percent model alternate wing configuration with various grit sizes would be required to determine if the pressure drag for the configuration is invariant with Reynolds number.

As an alternate correlation, comparisons of pressure drag coefficient versus Mach number were made at the same unit Reynolds number conditions for the three basic model configurations. The results presented in Fig. 31 show that the three models are in better agreement at low subsonic Mach numbers than at the nominal characteristic Reynolds number conditions shown in Fig. 23. At M_∞ = 0.6, the pressure drag coefficient of the 17-percent model was four drag counts lower than that of the smaller models, whereas it was 13 drag counts higher when compared at the characteristic Reynolds number conditions. Also at transonic Mach numbers, the three models were in better agreement when compared at the same unit Reynolds number than when compared at the same characteristic Reynolds number. The error in Mach number required to bring the total zero-lift drag coefficient within agreement at Mach number 0.6 is an order of magnitude greater than the tunnel Mach number precision, and recent tunnel calibrations indicate that the calibration is not a function of unit Reynolds number over the range of these tests.

Comparisons of integrated aft-end pressure drag coefficient, $C_{D_{P_{AFT}}}$, at α = 0 are presented in Fig. 32. Subsonically, these results compared at nominal characteristic Reynolds number show that the aft-end drag levels of the 13- and 17-percent basic models are consistently lower than the aft-end drag level of the 4.7-percent model, although the discrepancy is small (within five drag counts). Transonically, the aft-end drag levels of the larger models are significantly lower than that of the 4.7-percent model. At a Mach number of 1.40, the aft-end pressure drag levels are in good agreement. The aft-end pressure levels versus Mach number are also compared at uniform unit Reynolds number conditions in Fig. 33. The results indicate good agreement at subsonic Mach numbers and at the

higher Mach numbers; the discrepancies noted at nominal characteristic Reynolds number conditions (see Fig. 32) are reduced when compared at the same unit Reynolds number.

4.3.2 Wings-Off Configuration

The drag characteristics measured with the wings-off configuration for all three models at α = 0 are presented in Fig. 34. The pressure drag characteristics are compared in Fig. 35. The 13- and 17-percent models have slightly higher drag coefficient levels than the 4.7-percent model at subsonic Mach numbers (approximately seven drag counts higher for the 17-percent model). This trend was also observed for the basic configuration, but the magnitude of the discrepancy is reduced for the wings-off configuration. A grit study was not made with the wings removed, and differences in drag may be attributable to improper grit size. Transonically, the drag coefficients for the larger models are lower than that for the 4.7-percent model. At M_∞ = 1.10, the 4.7- and 13-percent models are in good agreement, and at M_∞ = 1.20, the drag levels agree for all three models. Comparison of the wings-off data with the wings-on data presented in Figs. 22 and 23 shows that, with increasing free-stream Mach number, there is very little drag increase subsonically with wings off, whereas there is an apparant drag increase with the wings on.

A comparison of the integrated aft-end drag coefficients for the three models without wings is presented in Fig. 36. The subsonic drag levels of the larger models are lower than that of the 4.7-percent model by as much as six drag counts. It may also be noticed that the subsonic drag levels of the wings-on configurations presented in Fig. 32 are lower than the subsonic drag levels of the corresponding wings-off configuration shown in Fig. 36. The lower aft-end pressure drag level with wings on shows the effect of the pressure rise produced by the wing wake, and this effect is most pronounced at M_∞ = 0.95. Transonic interference effects are evident from Mach numbers 1.00 to 1.10.

4.3.3 Cylindrical Afterbody Configuration

The total drag and pressure drag coefficients for the three models with the cylindrical afterbody at α = 0 are shown in Figs. 37 and 38, respectively. These data show that the drag on the 13- and 17-percent models is again higher than that obtained on the 4.7-percent model at subsonic Mach numbers, as was noted with the basic model and wings-off configurations. However, at the transonic Mach numbers there were no large drag discrepancies at M_∞ = 1.00, 1.05, and 1.10 such as were observed with the basic and wings-off configurations shown in Figs. 22 and 34, respectively. This indicates that the large changes in drag coefficient at transonic Mach numbers are primarily the result of changes in the aft-end drag on the contoured afterbody.

4.3.4 Interference Effects

The effects of model size on pressure drag coefficient for the basic model configuration and the alternate wing configuration are presented in Fig. 39. The data are presented as pressure drag increments of the 17-percent model relative to the 4.7-percent model compared at unit Reynolds number and characteristic Reynolds number conditions. These increments show an obvious effect of model size at Mach numbers 1.00 and 1.05. The decrease in drag with increasing model size is typical of transonic interference, and the data at $M_\infty = 1.00$ indicate that neither of the larger models is free of interference effects. The effect of model size at subsonic Mach numbers is such that, when the basic configurations are compared at the same characteristic Reynolds number conditions, the larger models have a consistently higher pressure drag coefficient. However, the drag levels and trends agree favorably for the basic configurations compared at unit Reynolds number and for the alternate wing configurations, up to $M_\infty = 0.90$.

The effects of model size on the integrated aft-end drag increments for the basic model configuration are shown in Fig. 40. The trends at $M_\infty = 1.00$ through 1.10 show results similar to those noted in Fig. 39. This indicates that the primary interference effect on drag at the transonic Mach numbers is the result of changes in aft-end drag on the contoured afterbody. At subsonic Mach numbers, the differences noted in drag levels in Fig. 39 for the basic configurations at characteristic Reynolds number are not a result of aft-end pressure drag.

4.4 BASIC MODEL AERODYNAMIC CHARACTERISTICS

The axial-force, normal-force, and pitching-moment coefficient data obtained with the three basic model configurations are presented in Figs. 41 and 42 for nominal characteristic Reynolds number conditions. The normal-force and pitching-moment characteristics are summarized in Figs. 43 and 44. The slopes of the normal-force and pitching-moment coefficient curves were determined between 0 and 3 deg angle of attack. The larger scale models have slightly lower normal-force curve slope and pitching-moment curve slope characteristics than the 4.7-percent model at Mach numbers from 0.60 to 1.00. At higher Mach numbers, the larger models have slightly higher normal-force and pitching-moment curve slope characteristics.

4.5 MODEL PRESSURE DISTRIBUTIONS

4.5.1 Basic Model Configuration

The top centerline pressure distribution on the 13-percent basic model at various Mach numbers is shown in Fig. 45. At the subsonic Mach numbers the pressure variations intensify with increasing Mach number, and a very strong recompression is exhibited at approximately X/L = 0.90. The most negative aft-end pressures are exhibited at M_∞ = 1.00. These effects become less pronounced at higher Mach numbers, and the aft-body shock is located slightly aft of X/L = 0.90.

Comparisons of the top centerline pressure distributions on the three basic models are shown in Fig. 46. Forward of X/L = 0.70, the pressure coefficients on the 13- and 17-percent models are consistently less negative than those on the 4.7-percent model at the subsonic Mach numbers and zero angle of attack. At X/L = 0.70 and further aft on the models, the pressure coefficients generally agree at Mach numbers up to 0.90 and at Mach numbers 1.20 and 1.40. At Mach numbers 0.95, 1.00, 1.05, and 1.10, the results indicate that the body pressures are significantly influenced by transonic interference effects. The pressure distribution data shown in Fig. 47 indicate the effect of angle of attack on the 13-percent scale model.

4.5.2 Wings-Off Configuration

The effect of the wings on the 4.7-percent scale model body top centerline pressure distribution is shown in Fig. 48. At the subsonic Mach numbers, the pressure coefficients are more negative over the mid portion of the basic body with wings. Aft of the wing trailing edge, X/L = 0.79, the pressure coefficients are slightly more positive. At supersonic Mach numbers, the effect at the wing trailing edge is reversed. The effects of wings on afterbody pressure distributions are further illustrated in Fig. 49, which shows pressure coefficient as a function of circumferential position on the afterbody. The pressure disturbances from the wing wake (ϕ = 90 deg) produced significantly higher pressure coefficients.

4.5.3 Cylindrical Afterbody Configuration

The top centerline pressure distributions with and without the cylindrical afterbody on the 4.7-percent basic model are compared in Fig. 50. The leading edge of the cylindrical afterbody was attached to the fuselage at X/L = 0.784. The cylindrical afterbody produced

a positive shift in pressure over the middle portion of the fuselage at subsonic Mach numbers. However, at supersonic Mach numbers, this effect did not propagate upstream on the fuselage, and only the pressure tap located immediately in front of the cylindrical afterbody was affected.

4.6 MODEL BASE AND STING PRESSURE

Average base pressure coefficients for the three basic model configurations are presented as a function of Mach number in Fig. 51. The pressure levels for the three models are in good agreement except at Mach numbers 1.00 through 1.10. The disagreement at transonic Mach numbers was probably a result of transonic interference effects. The base pressure coefficients for the models are positive through Mach number 1.10 as a result of the strong flow-field recompression on the model afterbody.

Sting pressure distributions for the three basic model configurations are compared in Fig. 52 for Mach numbers from 0.60 to 1.40. Subsonically, the pressure distributions are in good agreement for all stings except for small differences (X_s/D_b = 1.0 at M_∞ = 0.95). As with the base pressures, for Mach numbers from 1.00 through 1.20, the discrepancies in sting pressure distributions are probably caused by transonic interference effects. At M_∞ = 1.40, the sting pressures are again in good agreement. In all cases, maximum positive pressures were measured one base diameter downstream of the model, indicating approximately the point of maximum flow-field recompression.

The comparisons of base pressure data and sting pressure distribution show that the subsonic flow field at the model aft end and downstream had the same characteristics for all three model sting installations. Transonically, the discrepancies were probably a result of transonic interference effects.

5.0 CONCLUDING REMARKS

Wind tunnel investigations of three different scale models were conducted to determine the effects of model scaling in the subsonic and transonic flow regimes. The models were 4.7-, 13-, and 17-percent scale F-15 fighter equivalent body models. Results are summarized as follows:

1. At subsonic Mach numbers, the zero-lift pressure drag coefficient of the basic configurations (blunt leading-edge wing) was a function of Reynolds number and Mach number.

2. Subsonically, the pressure drag coefficient for the fuselage-alone configuration and the alternate wing configuration (wedge leading-edge wing) was essentially invariant with Mach number for free-stream Mach numbers below 0.90.

3. Data obtained with the cylindrical afterbody model and integrated aft-end pressure drag differences show that the transonic interference resulting from model size is primarily confined to the contoured fuselage afterbody.

4. Drag characteristics obtained for the three models were in better agreement when compared at the same unit Reynolds number than when compared at characteristic Reynolds numbers.

5. The transition grit had very little effect on the basic model configurations.

REFERENCES

1. Test Facilities Handbook (Ninth Edition). "Propulsion Wind Tunnel Facility, Vol. 4." Arnold Engineering Development Center, July 1971.

2. Braslow, A. L. and Knox, E. C. "Simplified Method for Determination of Critical Height of Distributed Roughness Particles for Boundary-Layer Transition at Mach Numbers from 0 to 5." NACA TN 4363, September 1958.

3. Shapiro, A. H. The Dynamics and Thermodynamics of Compressible Fluid Flow, Vol. II. Ronald Press Co., New York, 1954.

4. Braslow, A. L., Hicks, R. M., and Harris, R. V., Jr. "Use of Grit-Type Boundary-Layer Transition Trips on Wind Tunnel Models." NASA TN D-3579, September 1966.

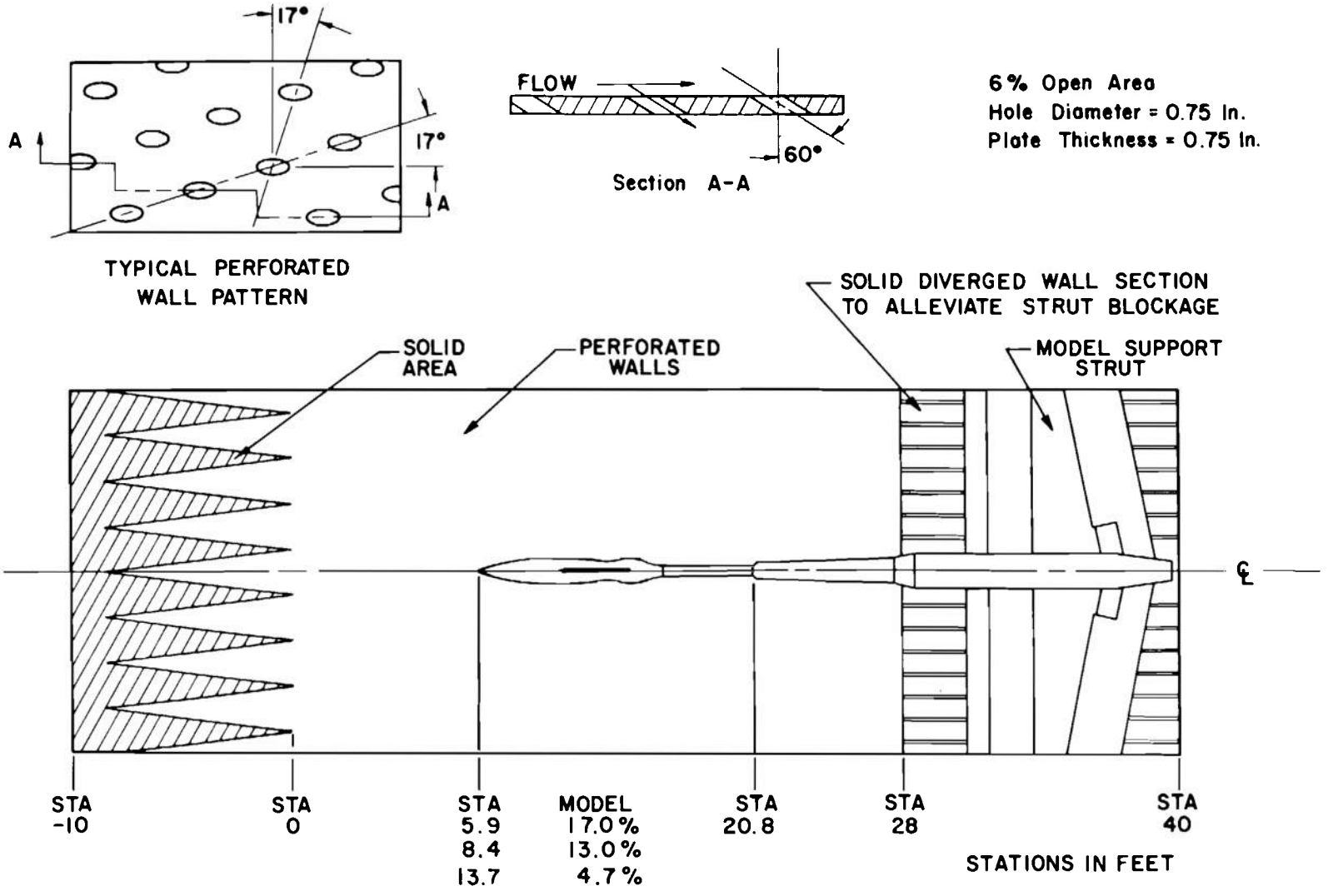

Figure 1. Location of models in test section.

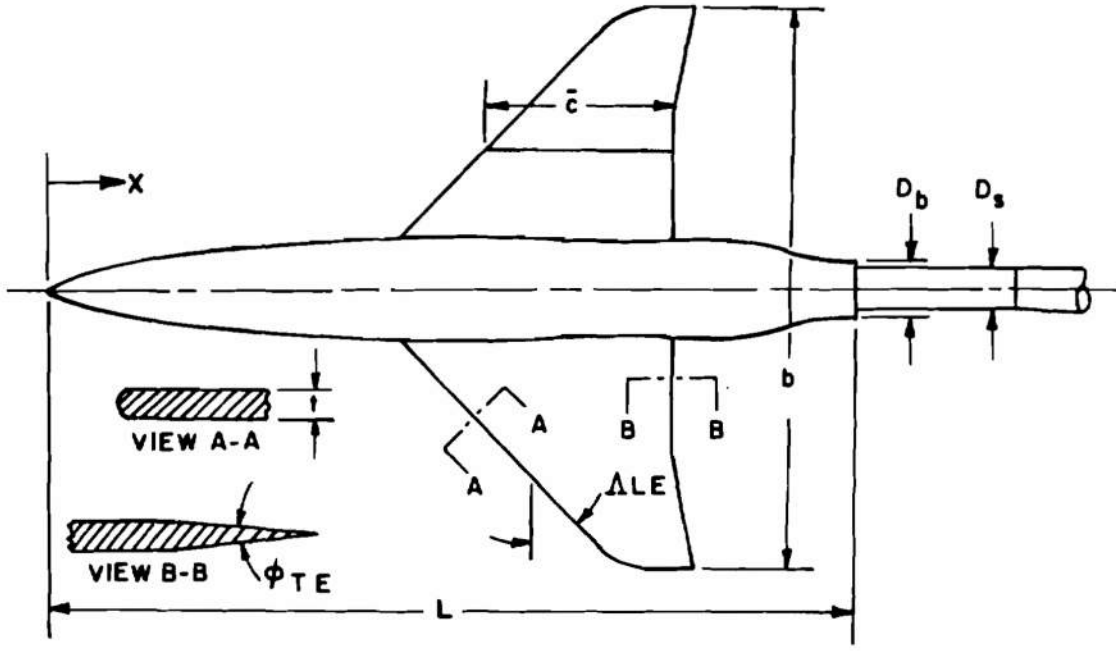

DIMENSIONS ARE FULL SCALE

L = 63.752 ft
b = 42.800 ft
$\bar{c}$ = 15.940 ft
t = 0.408 ft
ASPECT RATIO AR = 3.0
TAPER RATIO λ = 0.25
Λ_{LE} = 45°
ϕ_{TE} = 12°
WING REFERENCE AREA S = 608.00 ft^2
A_{BASE} = 13.750 ft^2
D_s/D_b = 0.703
WING WETTED AREA = 926.14 ft^2
FUSELAGE WETTED AREA = 1229.33 ft^2

Figure 2. Summary of basic model geometry.

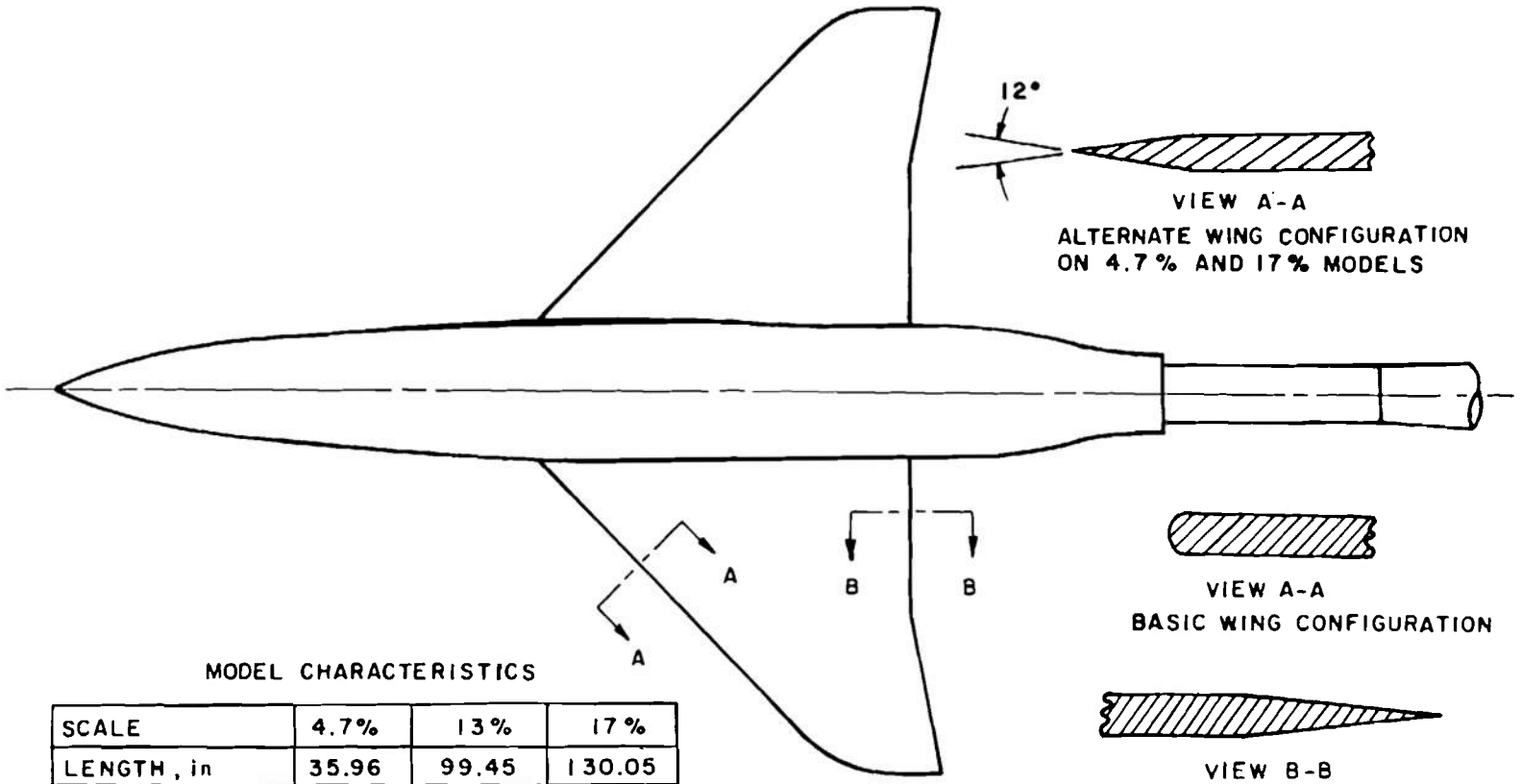

MODEL CHARACTERISTICS

SCALE	4.7%	13%	17%
LENGTH, in	35.96	99.45	130.05
MAX. DIAM, in	4.47	12.36	16.16
BLOCKAGE, $\frac{A_{MAX}}{A_{TUNNEL}}$	0.050%	0.381%	0.651%
$\frac{\text{WING SPAN}}{\text{TUNNEL WIDTH}}$	0.13	0.35	0.45

Figure 3. Comparisons of scale model characteristics.

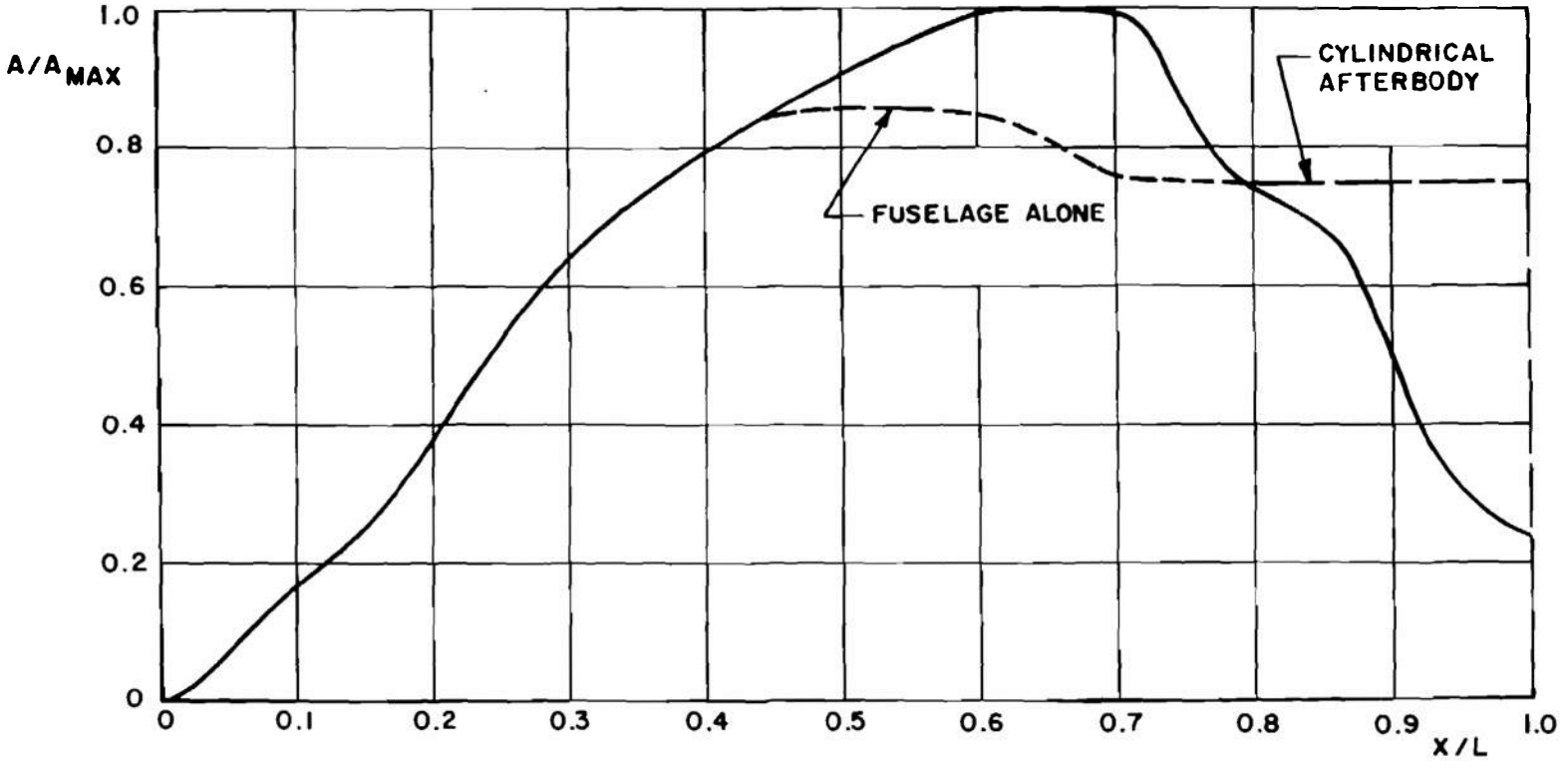

Figure 4. Model cross-sectional area distribution.

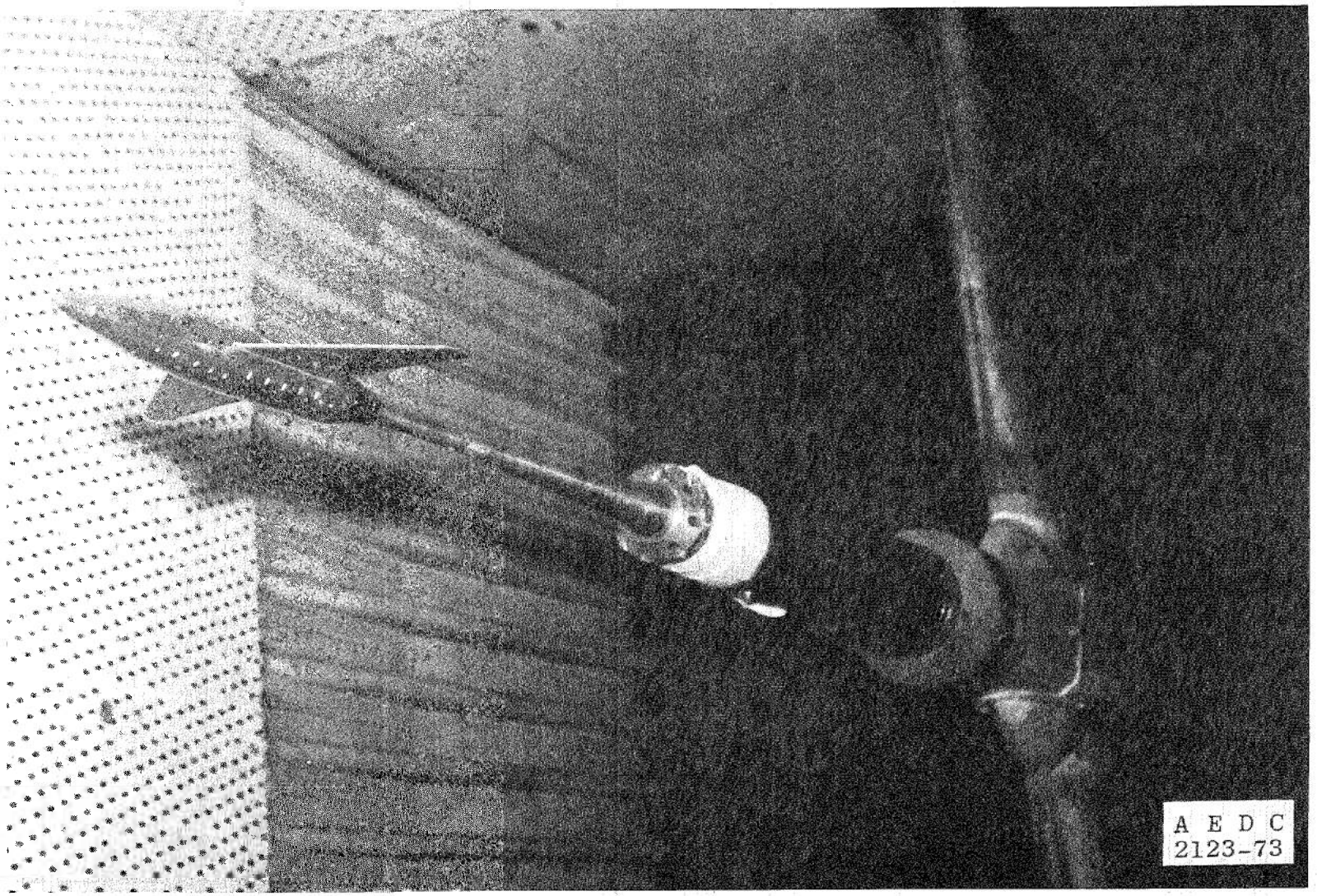

a. 4.7-percent scale model

Figure 5. Model installation photographs.

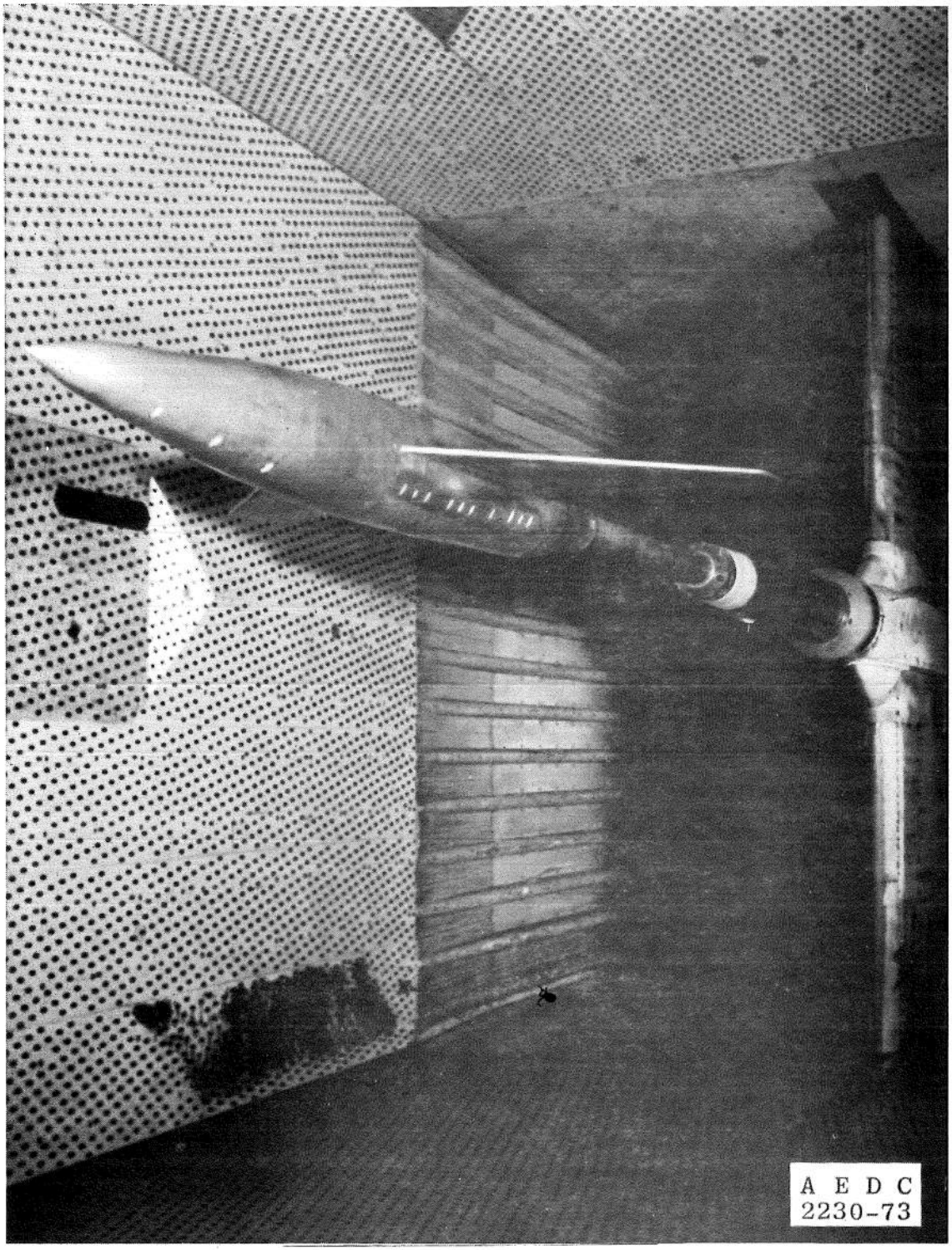

b. 13-percent scale model
Figure 5. Continued.

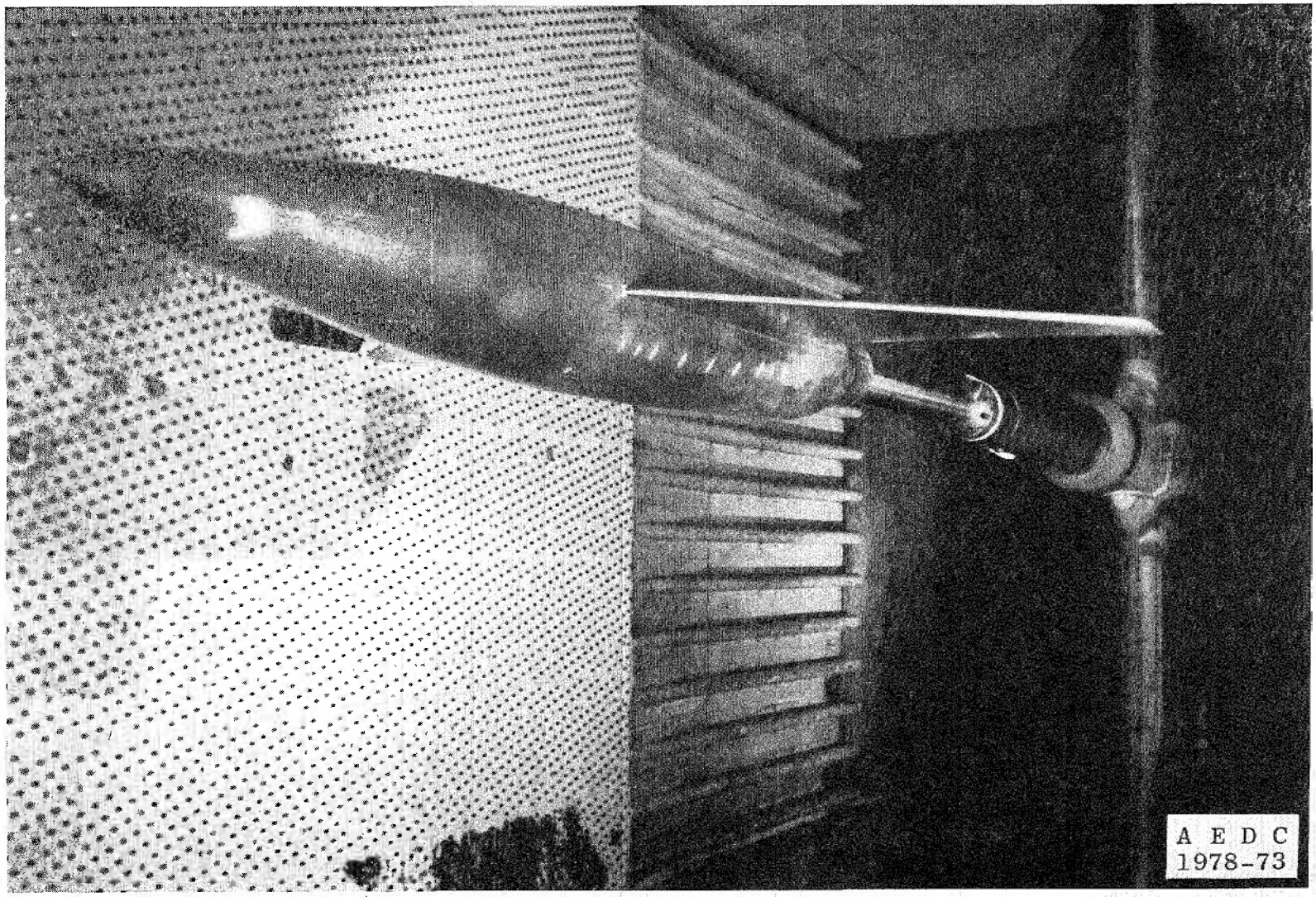

c. 17-percent scale model
Figure 5. Continued.

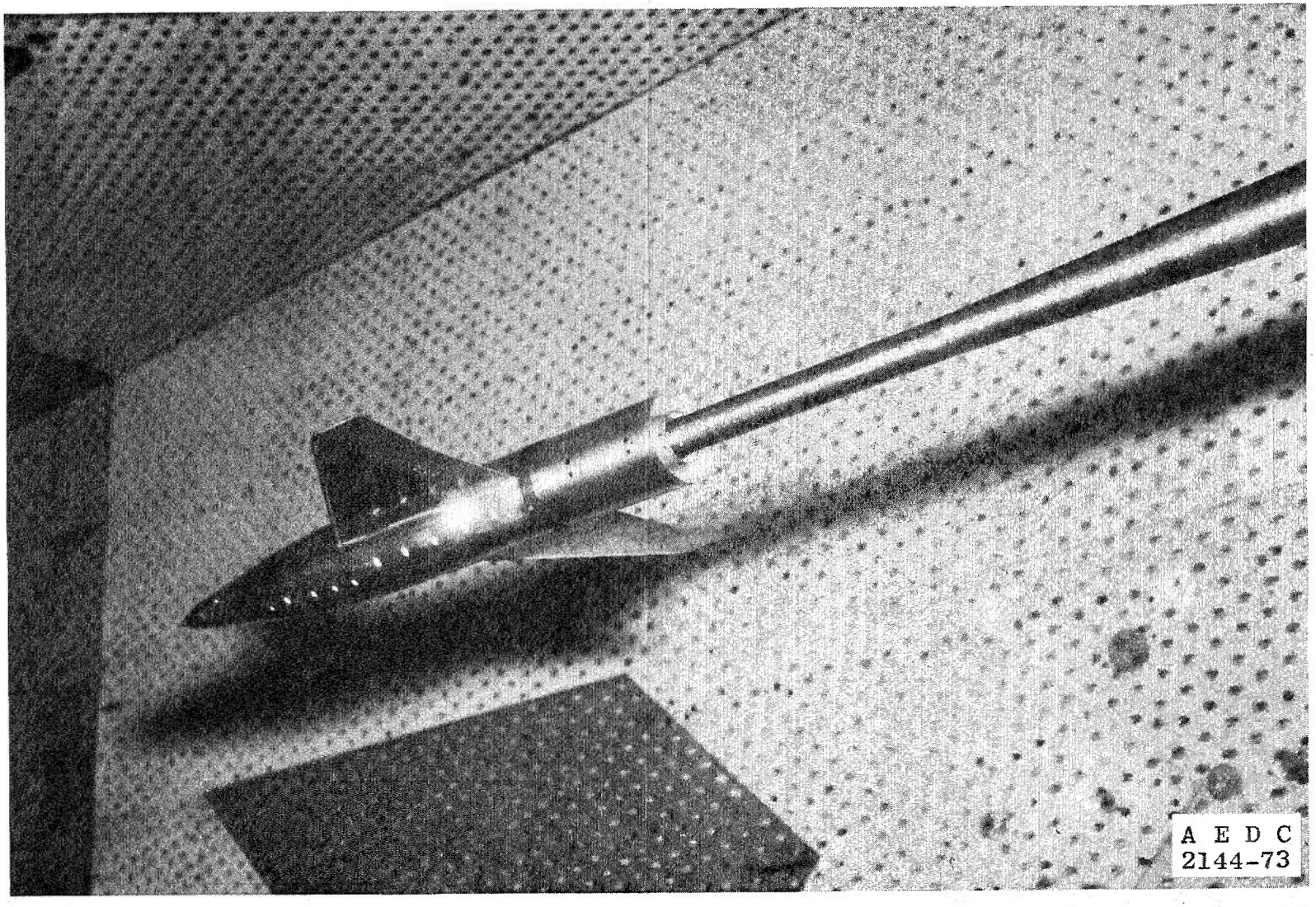

d. 4.7-percent scale model with cylindrical afterbody
Figure 5. Continued.

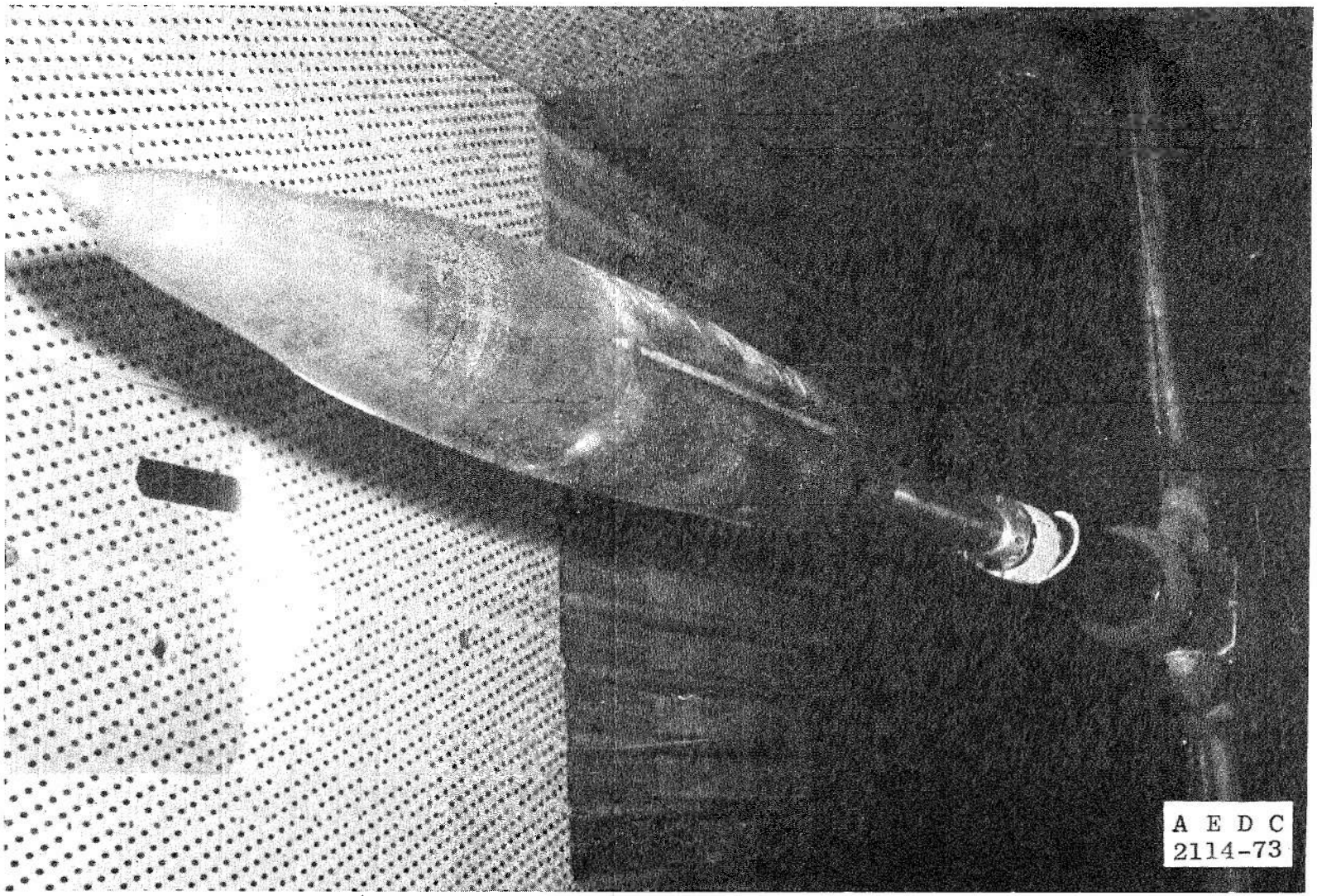

e. 17-percent scale model without wings
Figure 5. Concluded.

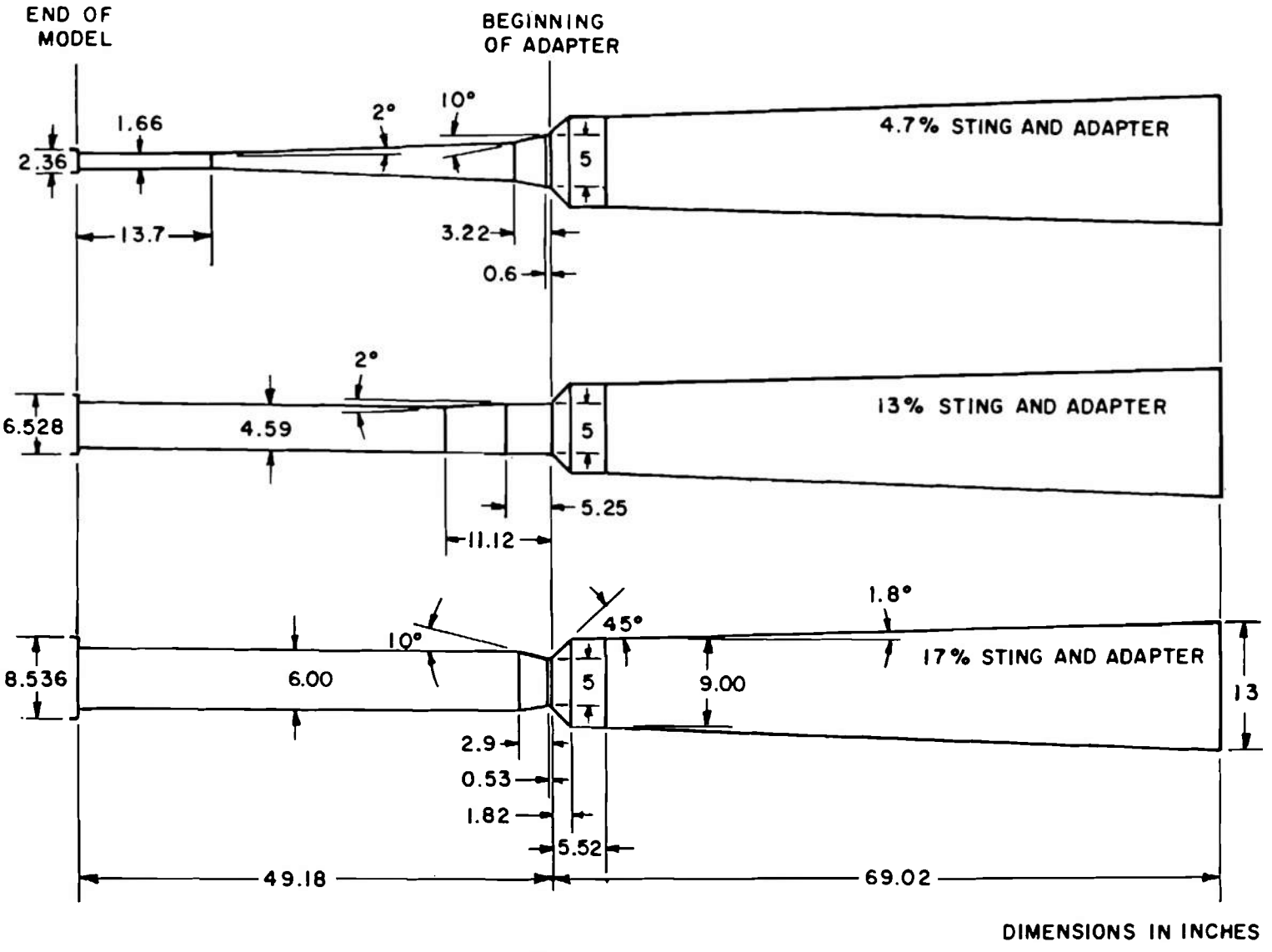

Figure 6. Sting and adaptor geometry.

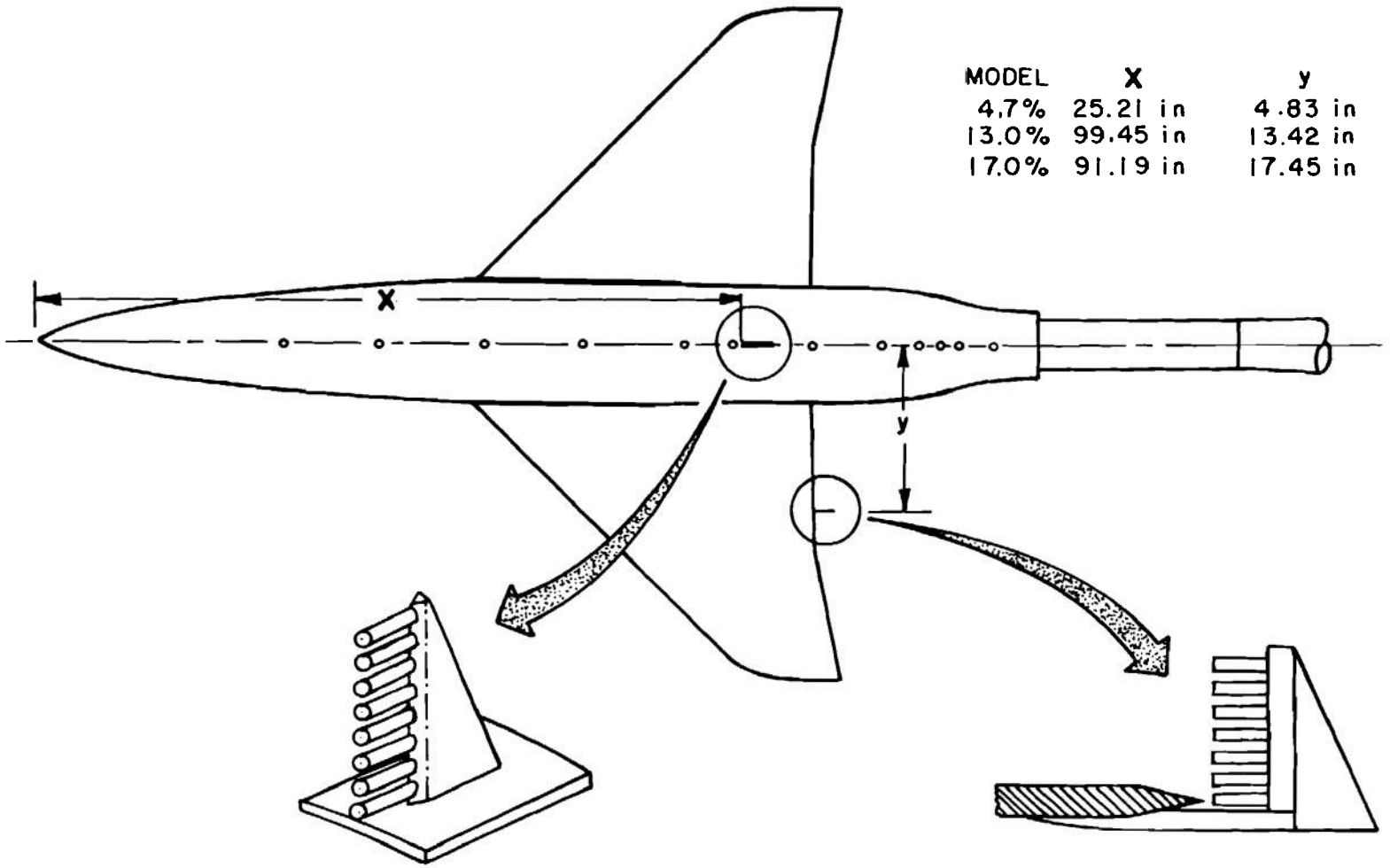

Figure 7. Boundary-layer rake location.

FUSELAGE RAKE

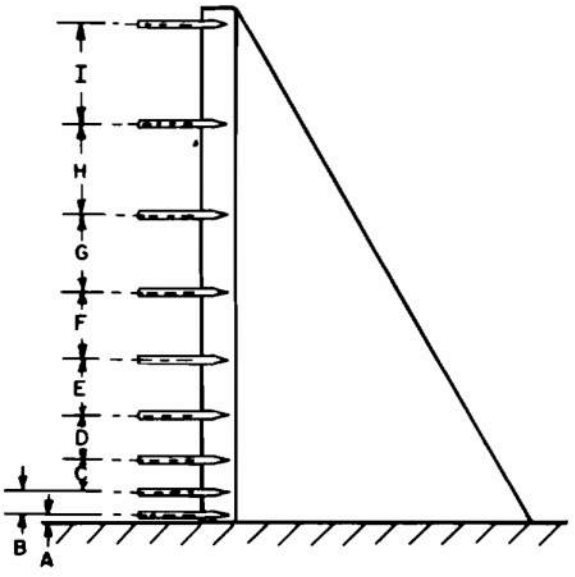

WING TRAILING-EDGE RAKE

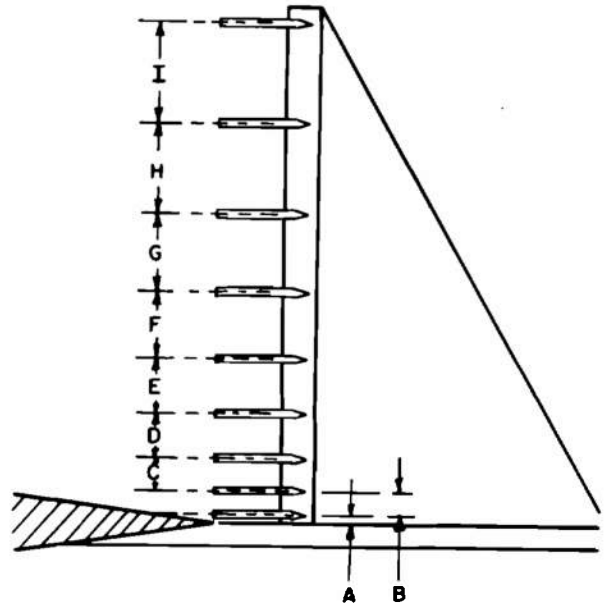

FUSELAGE RAKE DIMENSIONS

	4.7 % and 13% MODELS	17% MODEL
A	0.150	0.150
B	0.220	0.280
C	0.310	0.525
D	0.400	0.860
E	0.510	1.300
F	0.650	1.850
G	0.800	2.510
H	0.980	3.280
I	1.150	4.140

WING RAKE DIMENSIONS

	4.7% and 13% MODELS	17% MODEL
A	0.000	0.000
B	0.051	0.070
C	0.120	0.180
D	0.180	0.310
E	0.256	0.480
F	0.330	0.700
G	0.400	0.980
H	0.500	1.380
I	0.600	1.940

DIMENSIONS IN INCHES

Figure 8. Boundary-layer rake dimensions.

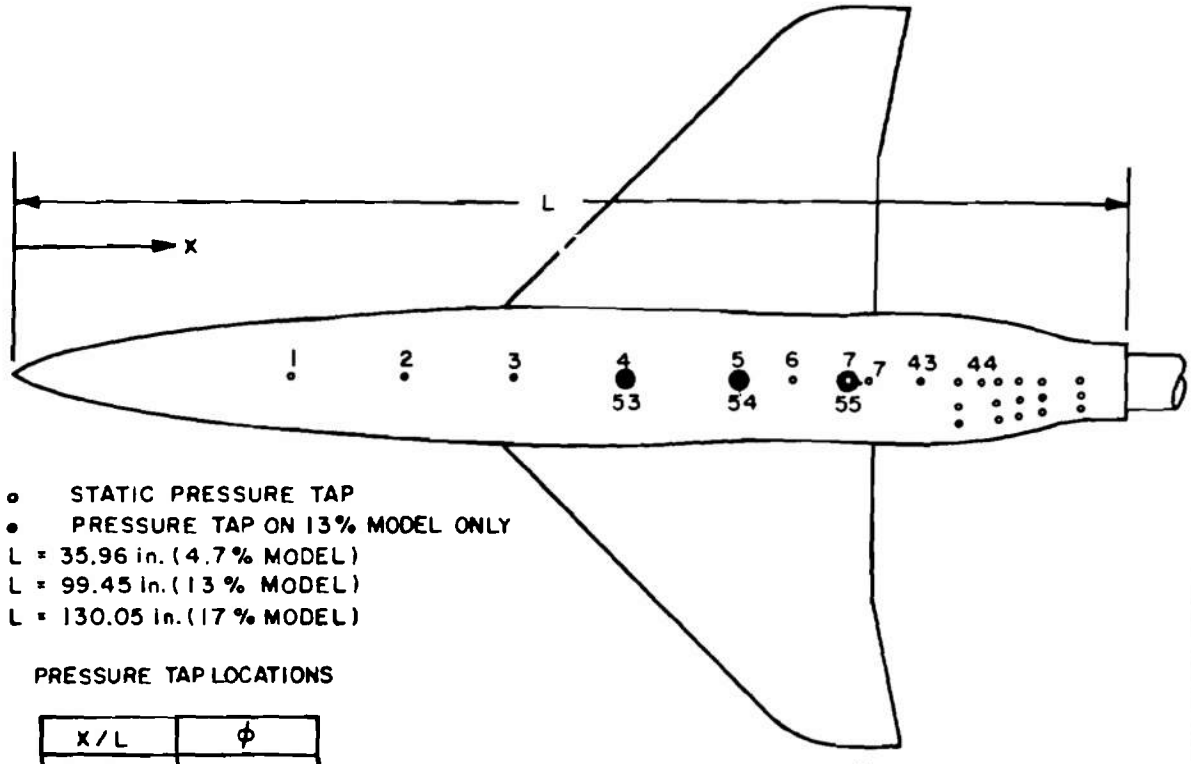

o STATIC PRESSURE TAP

• PRESSURE TAP ON 13% MODEL ONLY

L = 35.96 in. (4.7% MODEL)

L = 99.45 in. (13 % MODEL)

L = 130.05 in. (17 % MODEL)

PRESSURE TAP LOCATIONS

X/L	ϕ
0.2500	0°
0.3500	0°
0.4500	0°
0.5500	0°, 180°
0.6500	0°, 180°
0.7000	0°
0.7500	0°, 180°
0.7750	0°
0.8000	0°
0.8485	ϕ_1
0.8697	0°
0.8829	ϕ_1
0.9023	ϕ_1
0.9226	ϕ_1
0.9580	ϕ_2
1.0000	ϕ_3

ϕ_1 = 0°, 30°, 60°, 90°, 120°, 150°, 165°, 180°, 195°, 210°

ϕ_2 = 0°, 30°, 60°, 90°, 120°, 150°, 180°, 210°

ϕ_3 = 0°, 90°, 180°, 270°

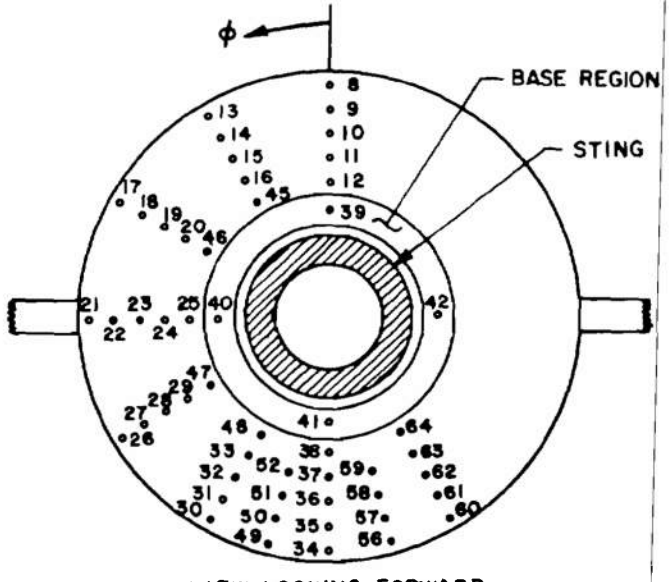

VIEW LOOKING FORWARD

Figure 9. Surface pressure instrumentation.

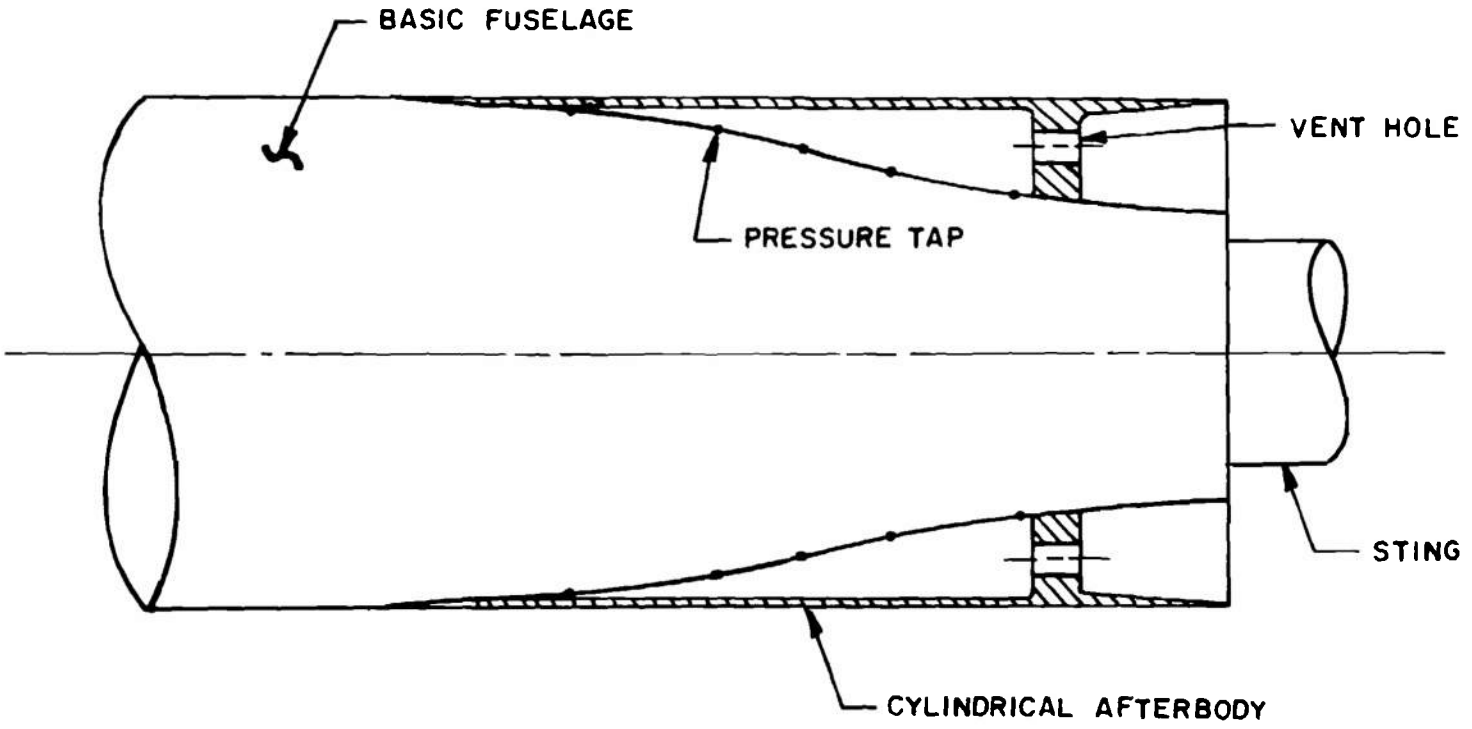

Figure 10. Cylindrical afterbody pressure instrumentation.

LOCATION OF STING SURFACE PRESSURE TAPS, X_s

MODEL	D_b	X_1	X_2	X_3	X_4	X_5	X_6
4.7%	2.36	0	1.18	2.36	3.54	4.72	5.90
13%	6.53	0	3.26	6.53	9.80	13.06	16.32
17%	8.54	0	4.27	8.54	12.80	17.08	21.35

DIMENSIONS IN INCHES

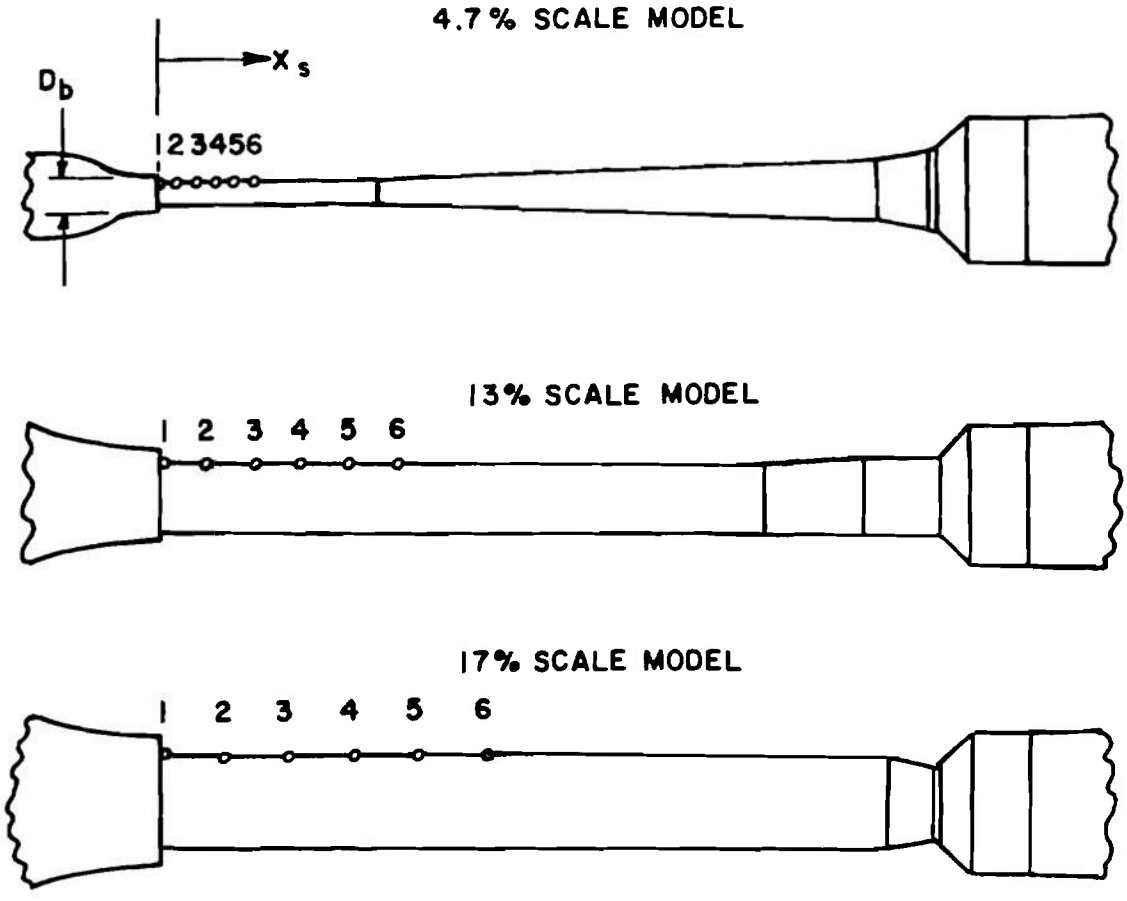

Figure 11. Location of sting surface pressure taps.

MACH NUMBER	CHARACTERISTIC REYNOLDS NUMBER, $R_{e_L} \times 10^{-6}$	REYNOLDS NUMBER, $R_e \times 10^{-6}$ ft^{-1}		
		4.7% MODEL	13% MODEL	17% MODEL
0.6 to 1.0	16	5.3	1.92	1.47
1.05	12	4.0	1.45	1.11
1.10	12	4.0	1.45	1.11
1.20	14	4.7	1.70	1.30
1.40	12	4.0	1.45	1.11

Figure 12. Nominal characteristic Reynolds number schedule.

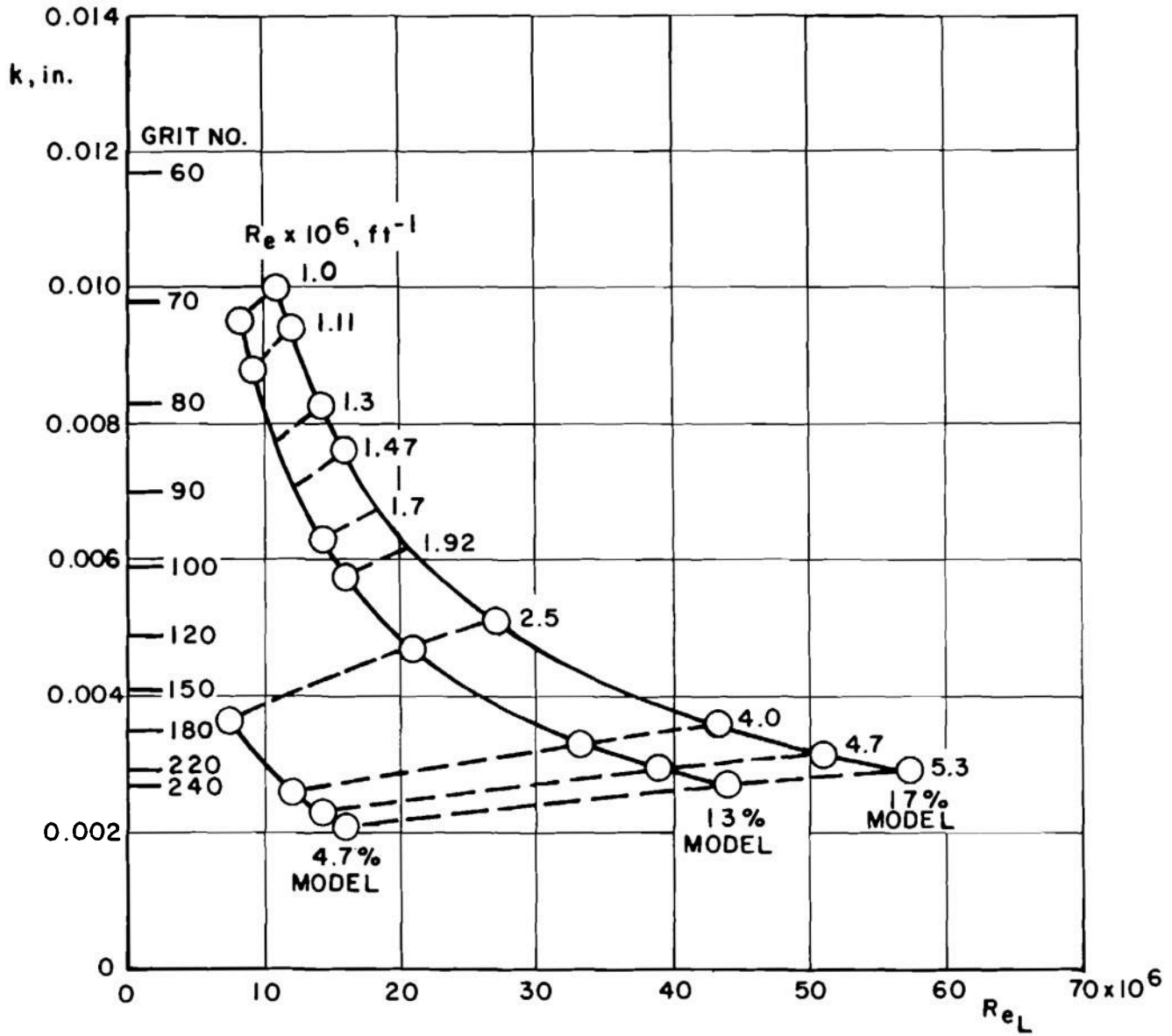

Figure 13. Minimum grit height to trip laminar boundary layer, nose grit located at X/L = 0.021.

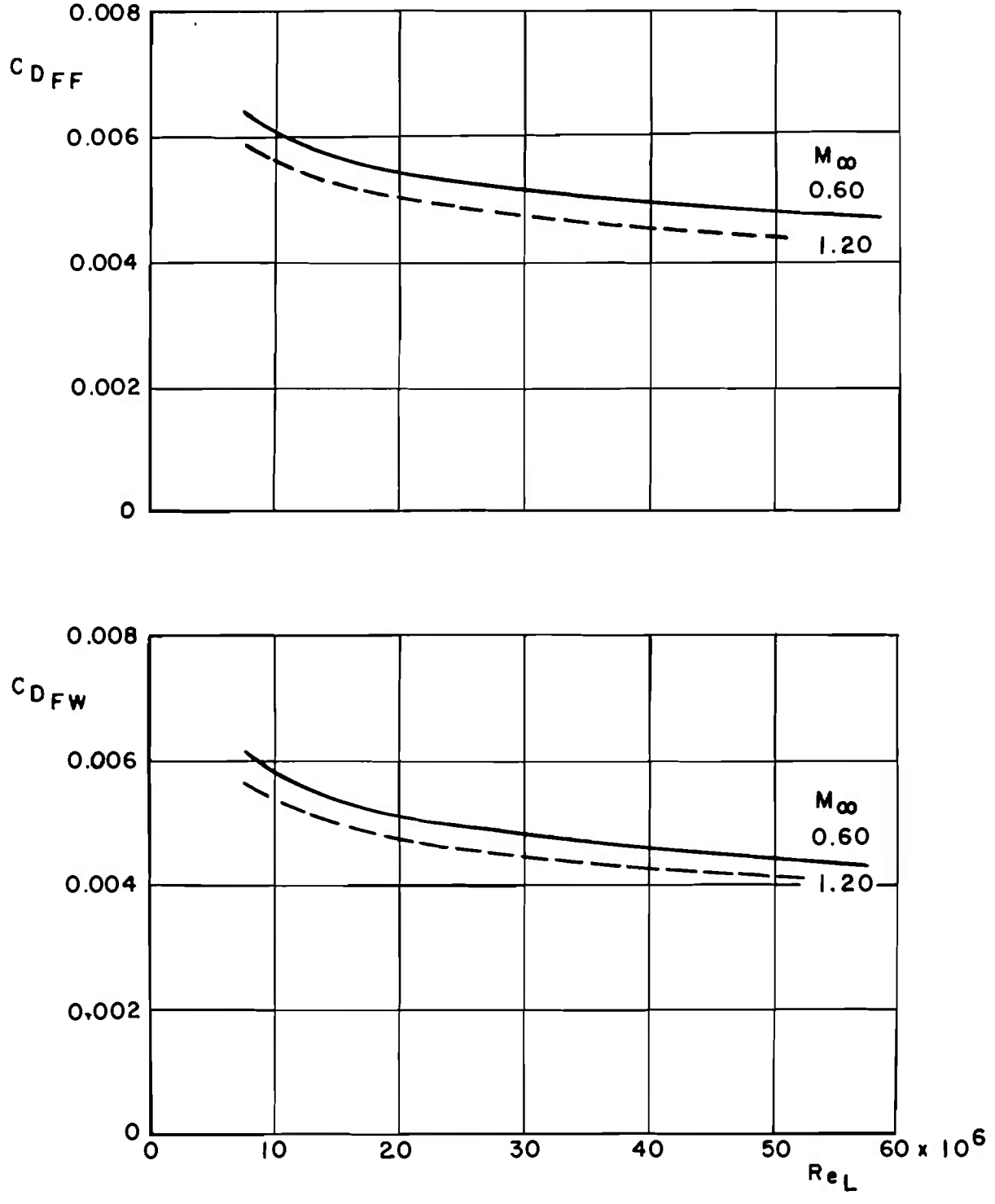

Figure 14. Friction drag estimates for fuselage and wing.

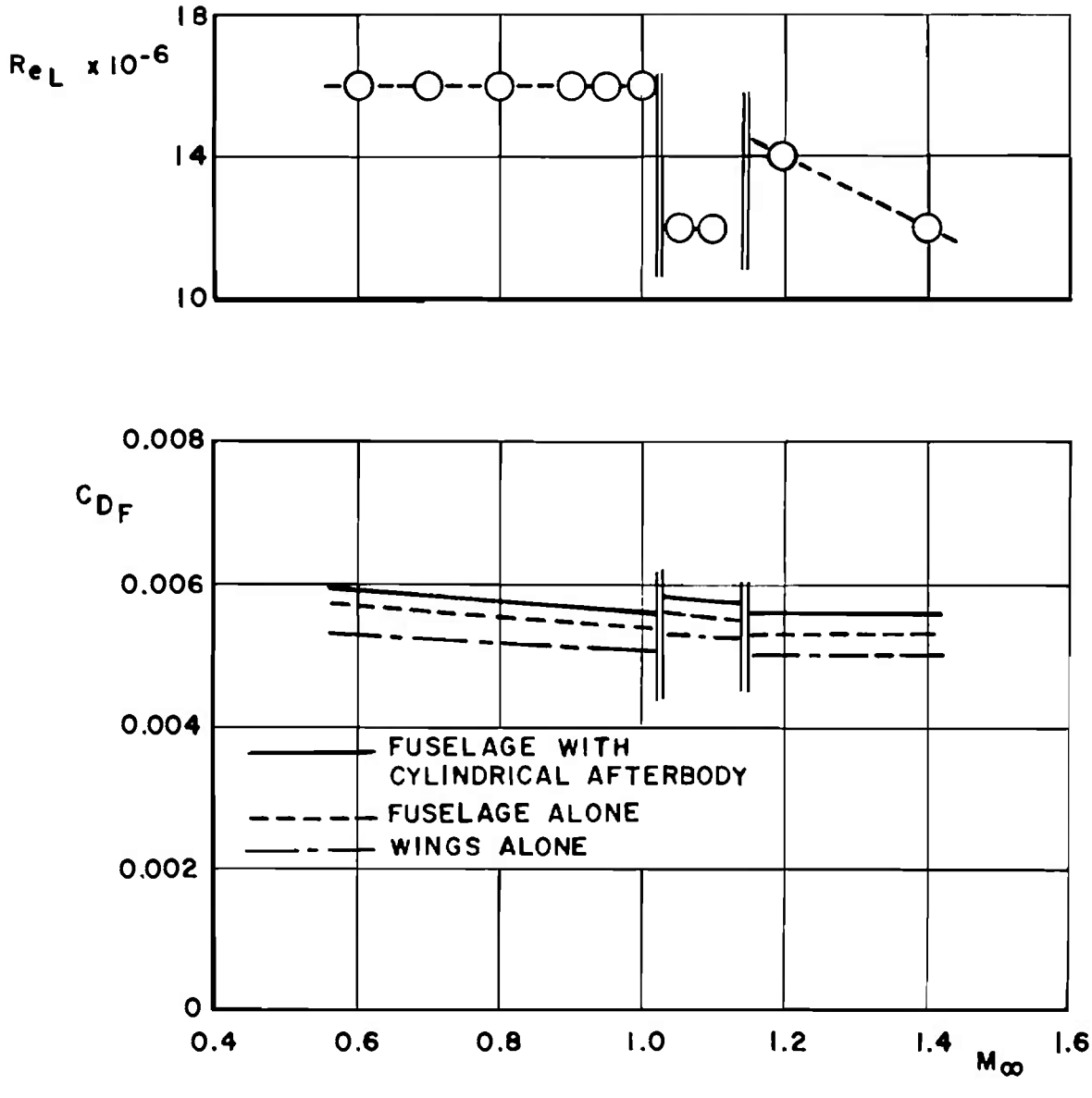

Figure 15. Nominal Reynolds number schedule and corresponding friction drag estimates.

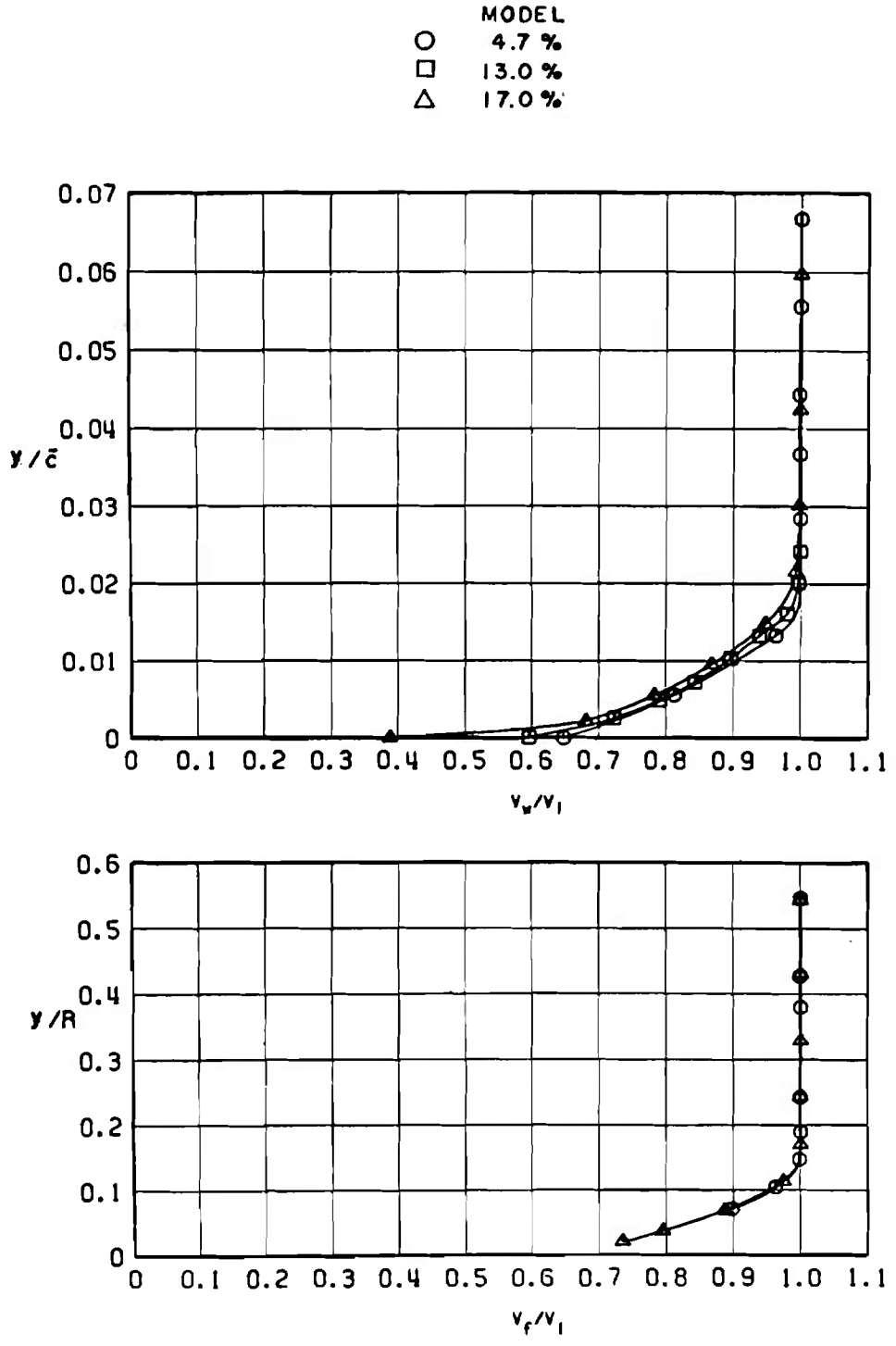

a. $M_\infty = 0.60$

Figure 16. Boundary-layer profiles for basic configuration at characteristic Reynolds number.

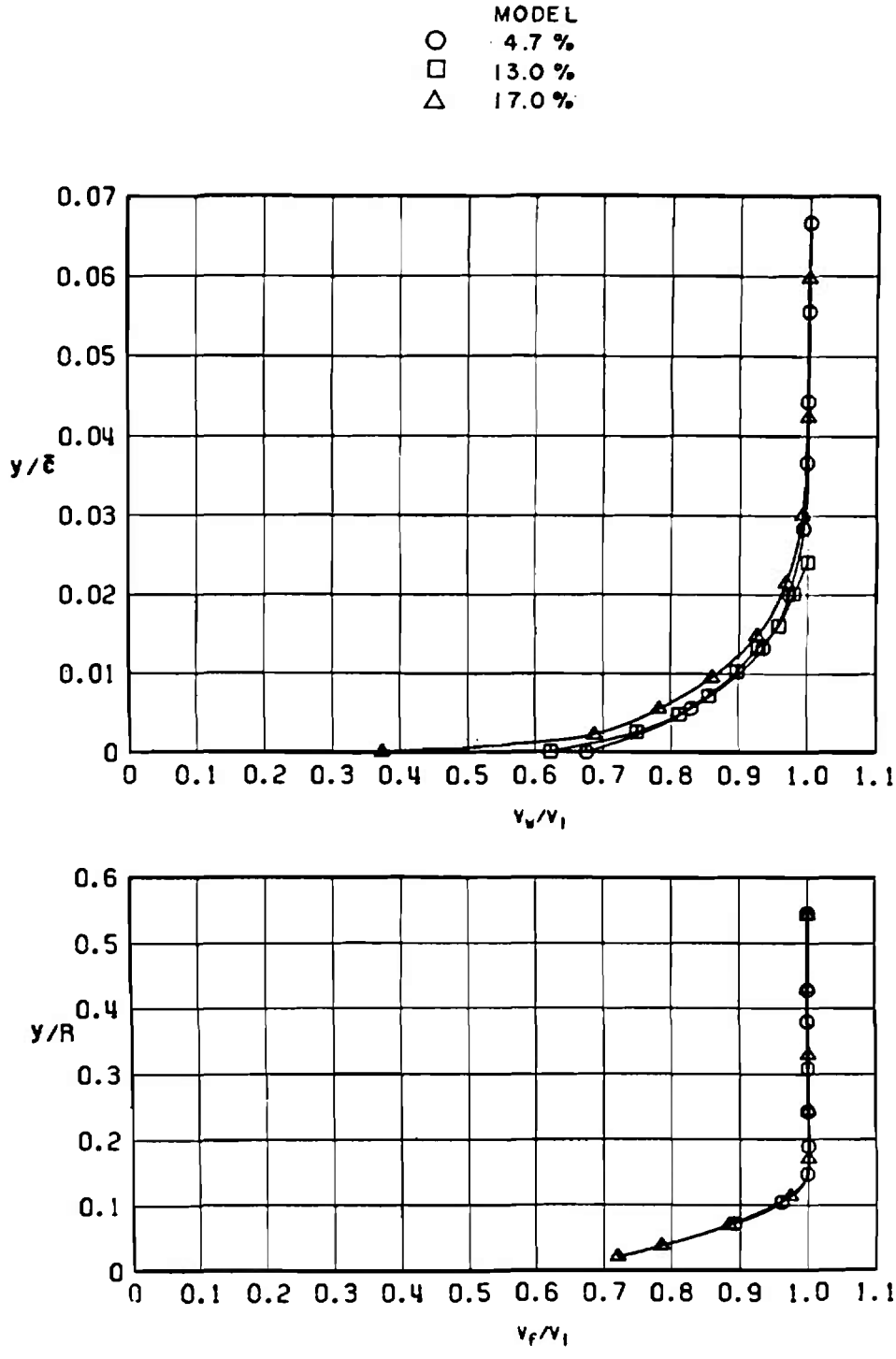

b. $M_\infty = 0.90$

Figure 16. Continued.

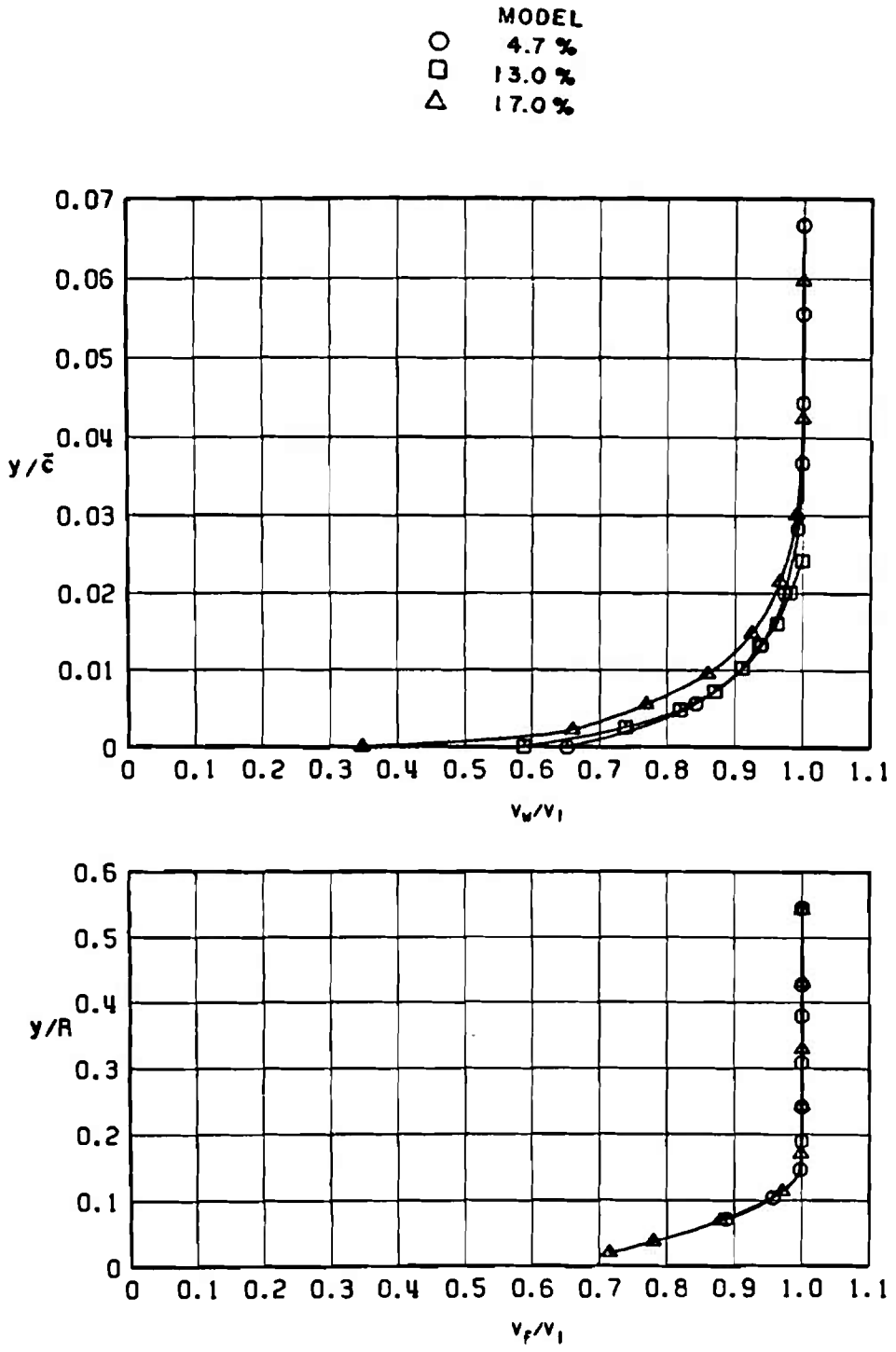

c. $M_\infty = 0.95$

Figure 16. Continued.

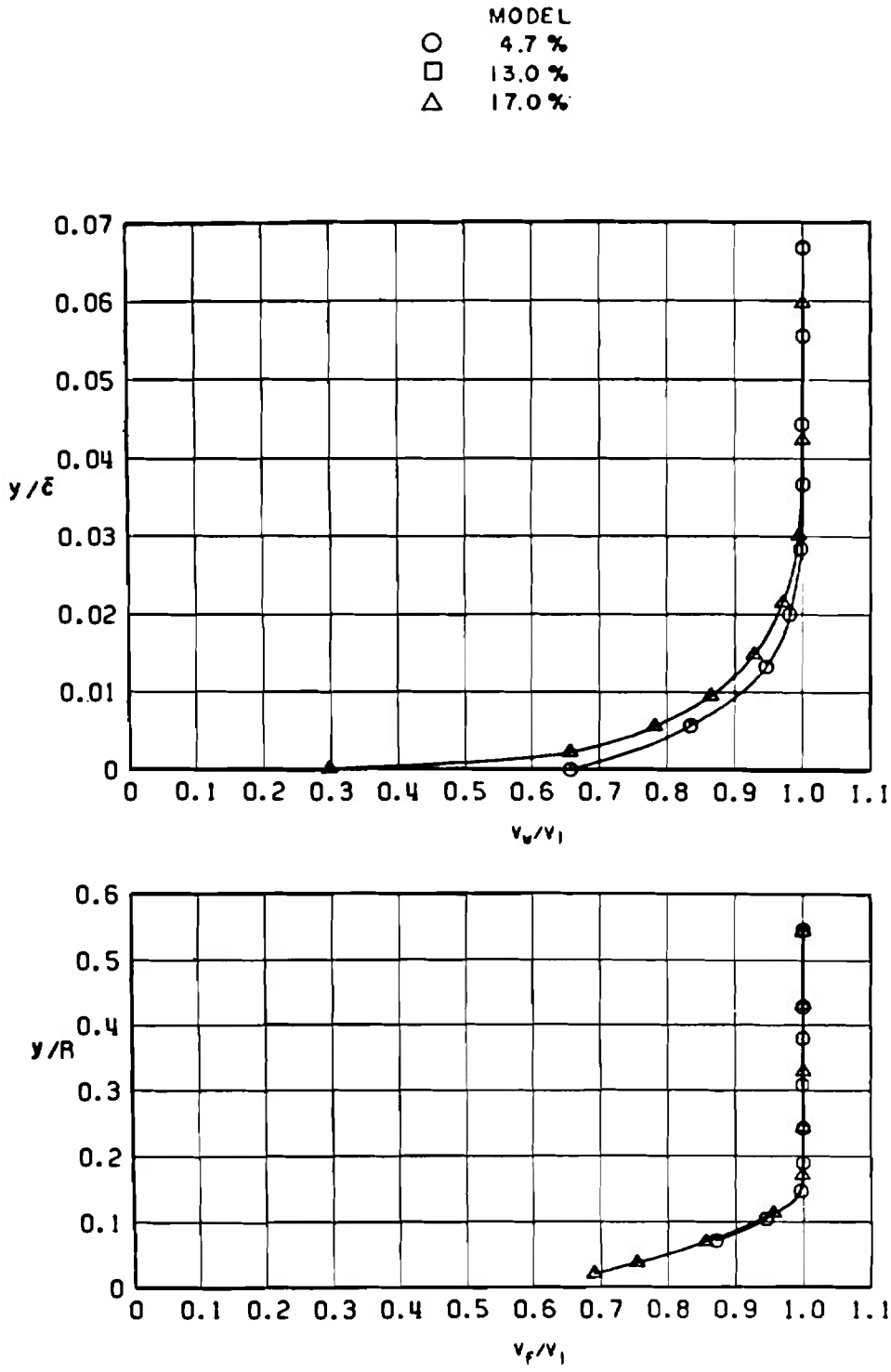

d. M_∞ = 1.05
Figure 16. Continued.

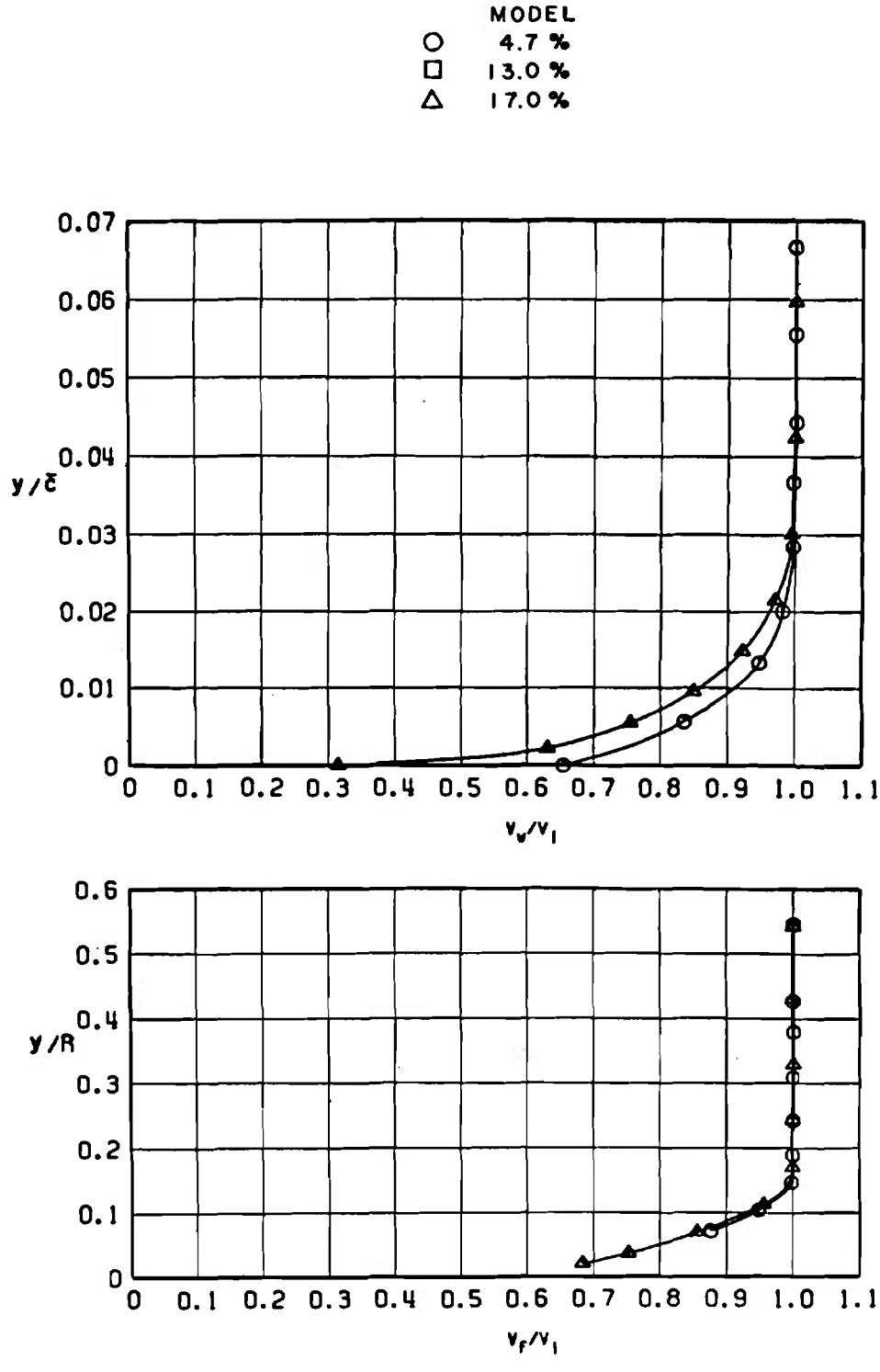

e. $M_\infty = 1.10$

Figure 16. Continued.

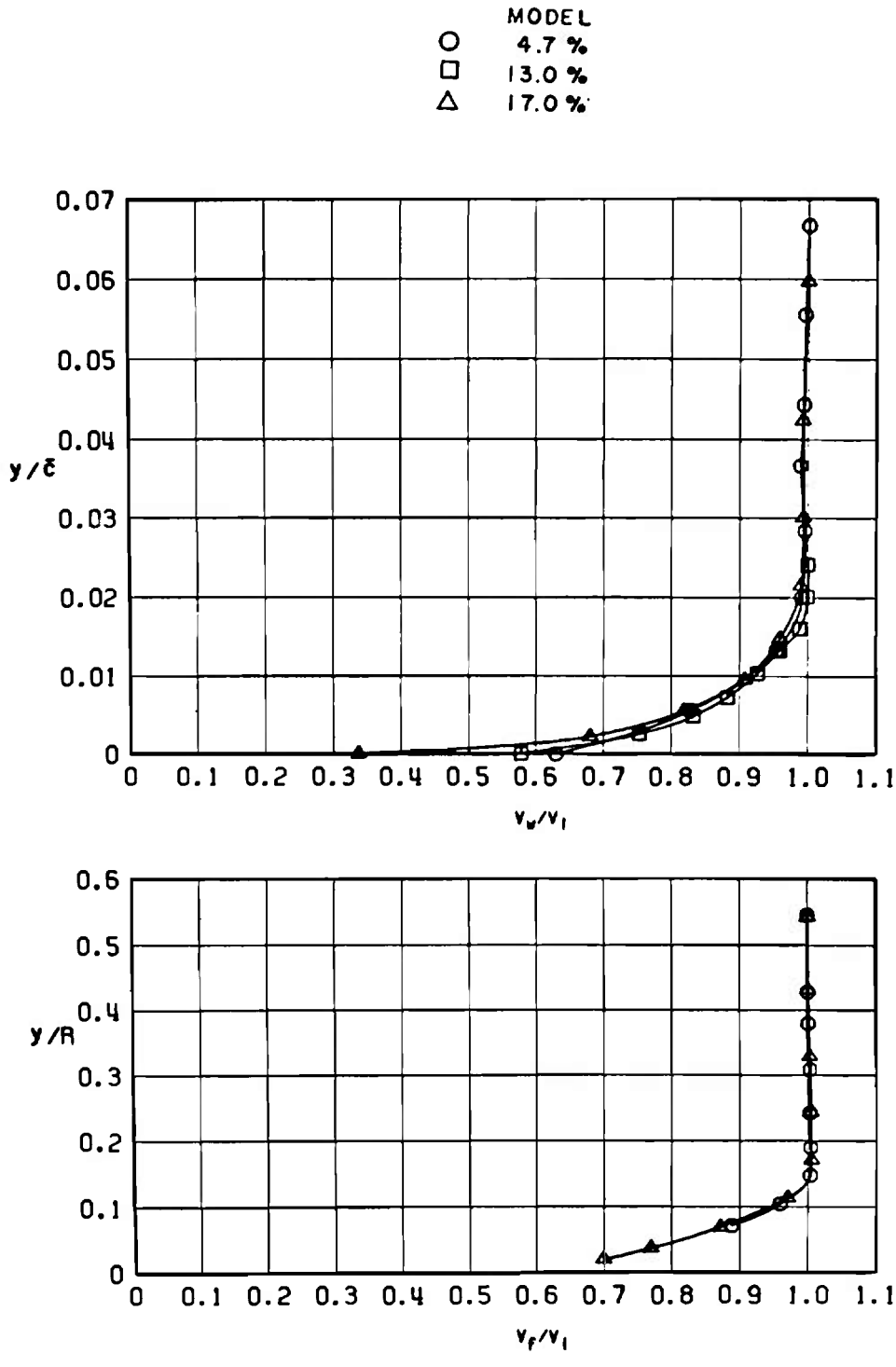

f. $M_\infty = 1.20$

Figure 16. Concluded.

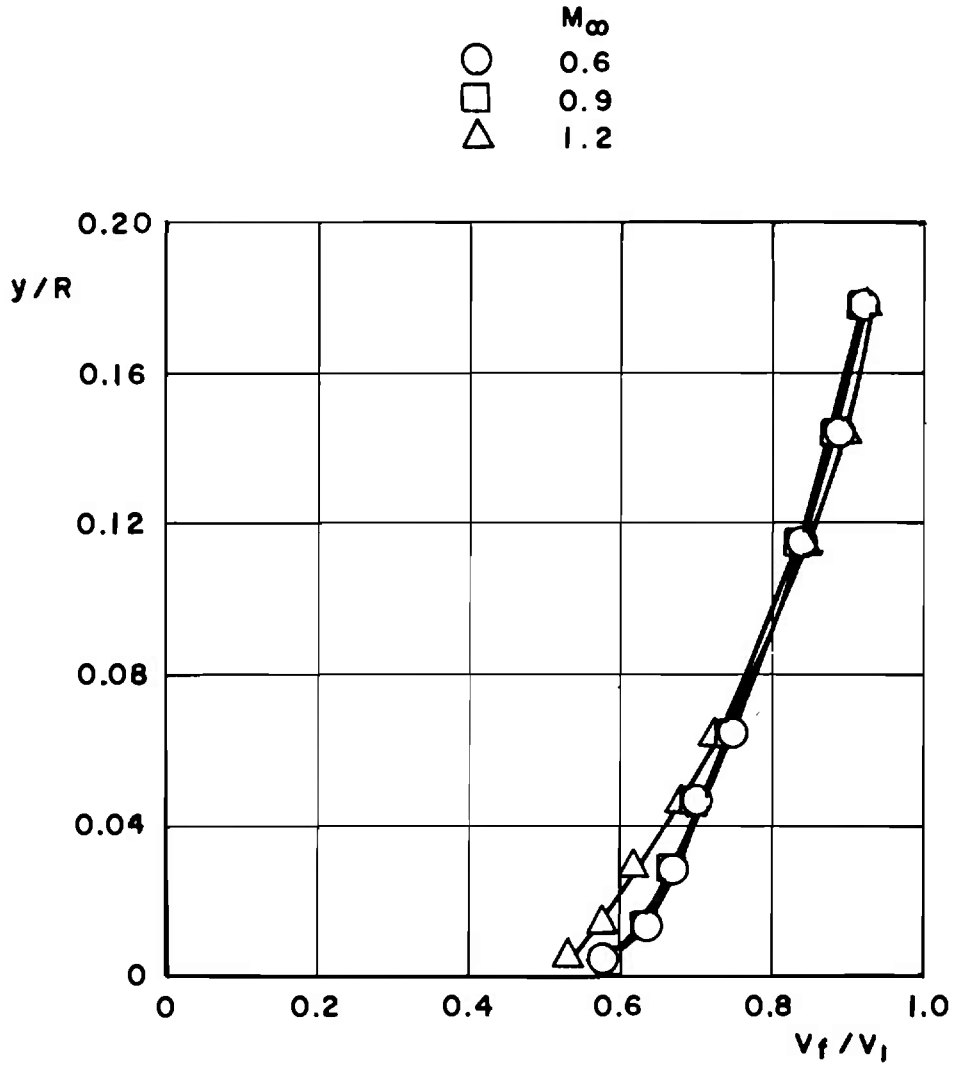

Figure 17. Boundary-layer profiles at the fuselage base, 13-percent scale basic model, Re_L = 21 x 10^6, α = 0.

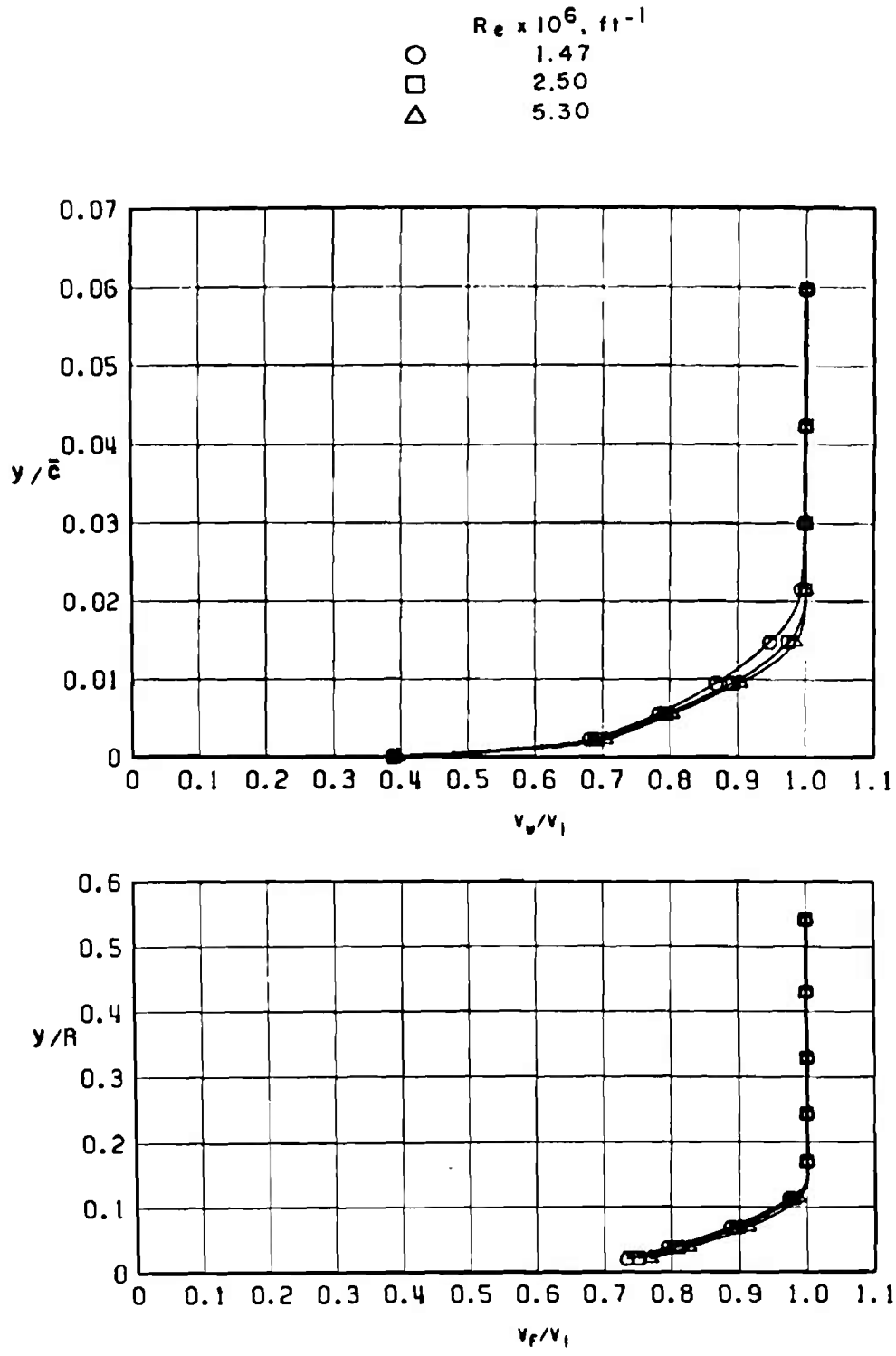

a. $M_\infty = 0.60$

Figure 18. Effects of Reynolds number on boundary-layer profiles, 17-percent basic model.

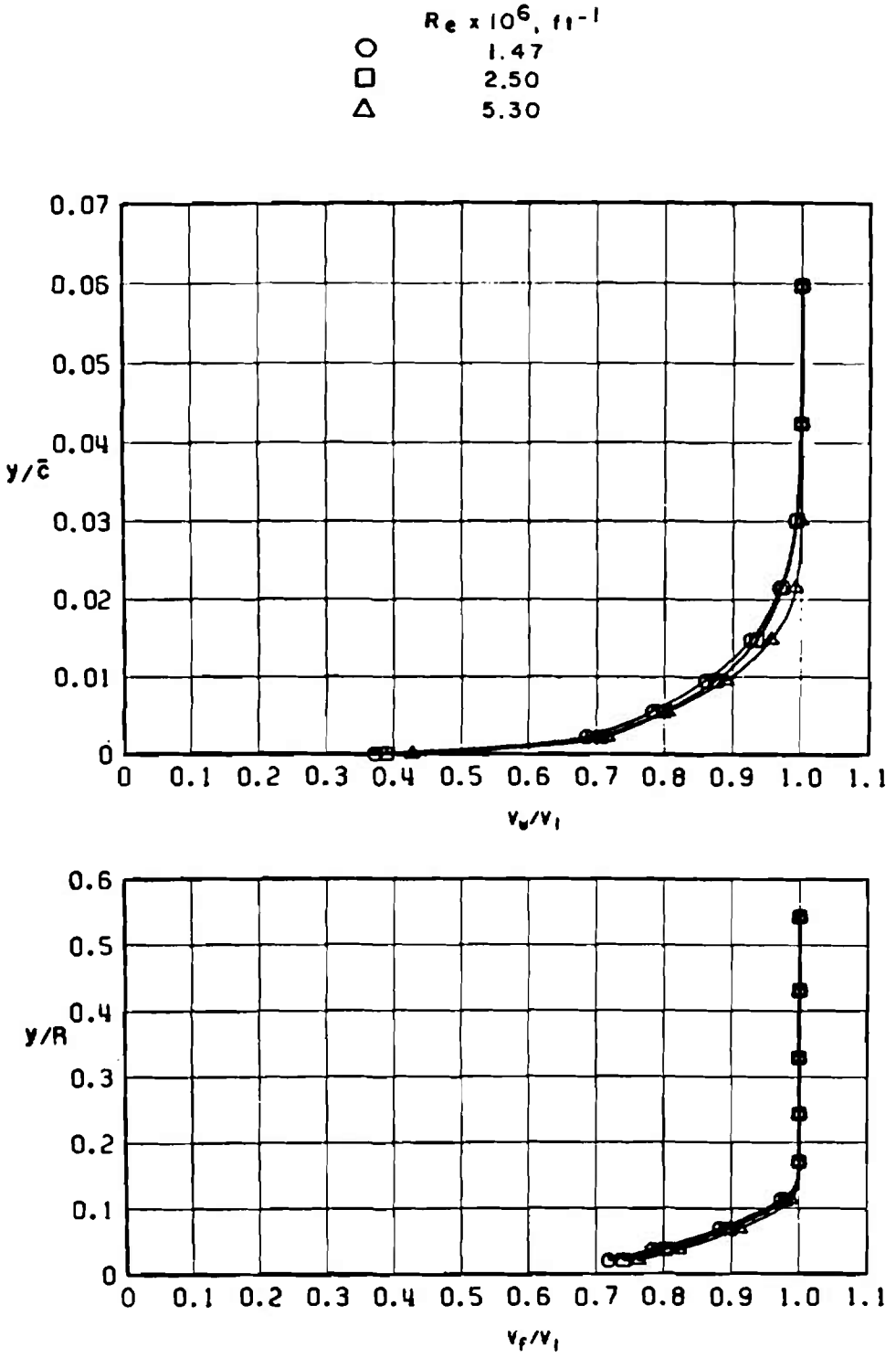

b. $M_\infty = 0.90$

Figure 18. Continued.

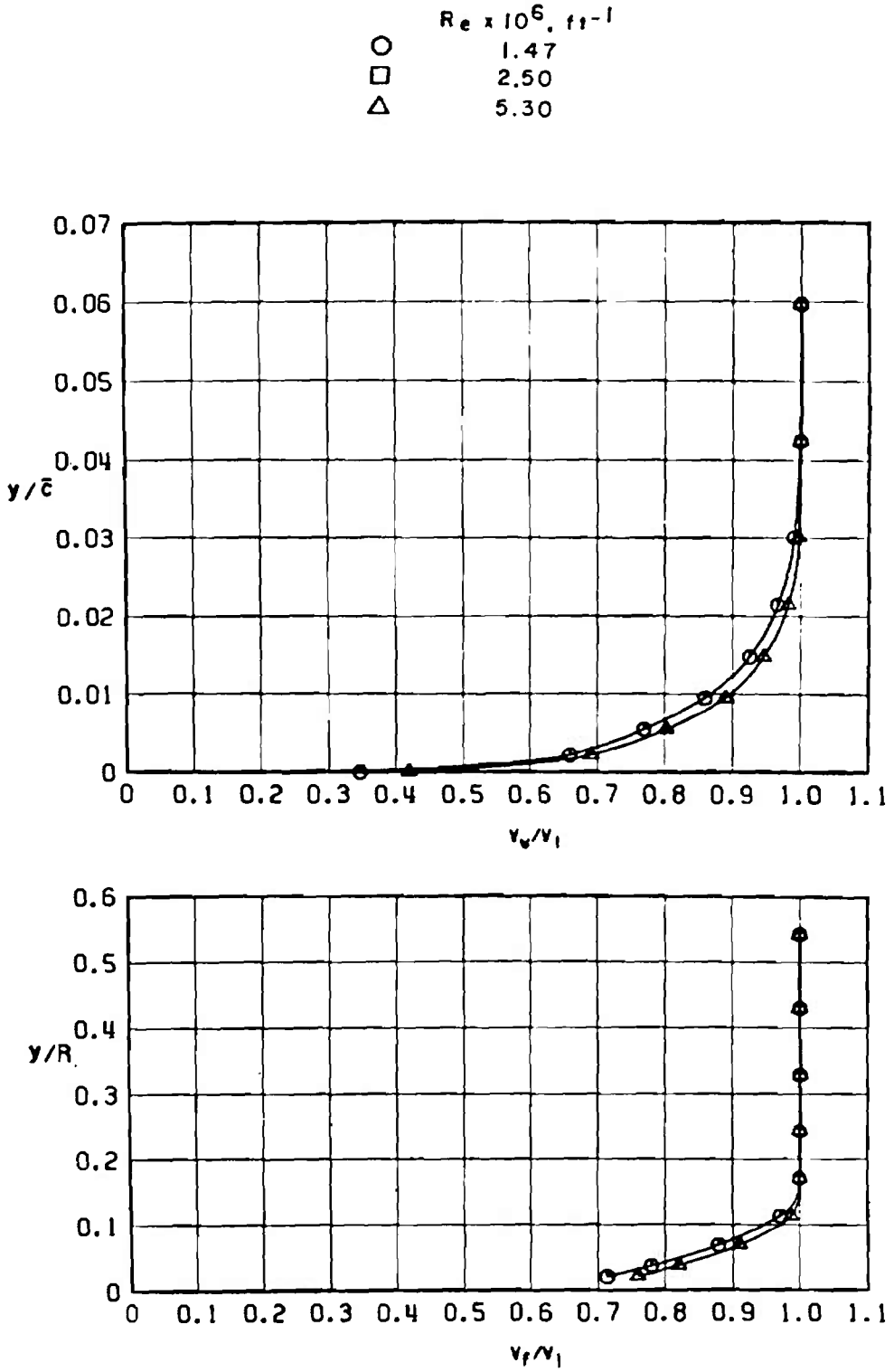

c. $M_\infty = 0.95$

Figure 18. Continued.

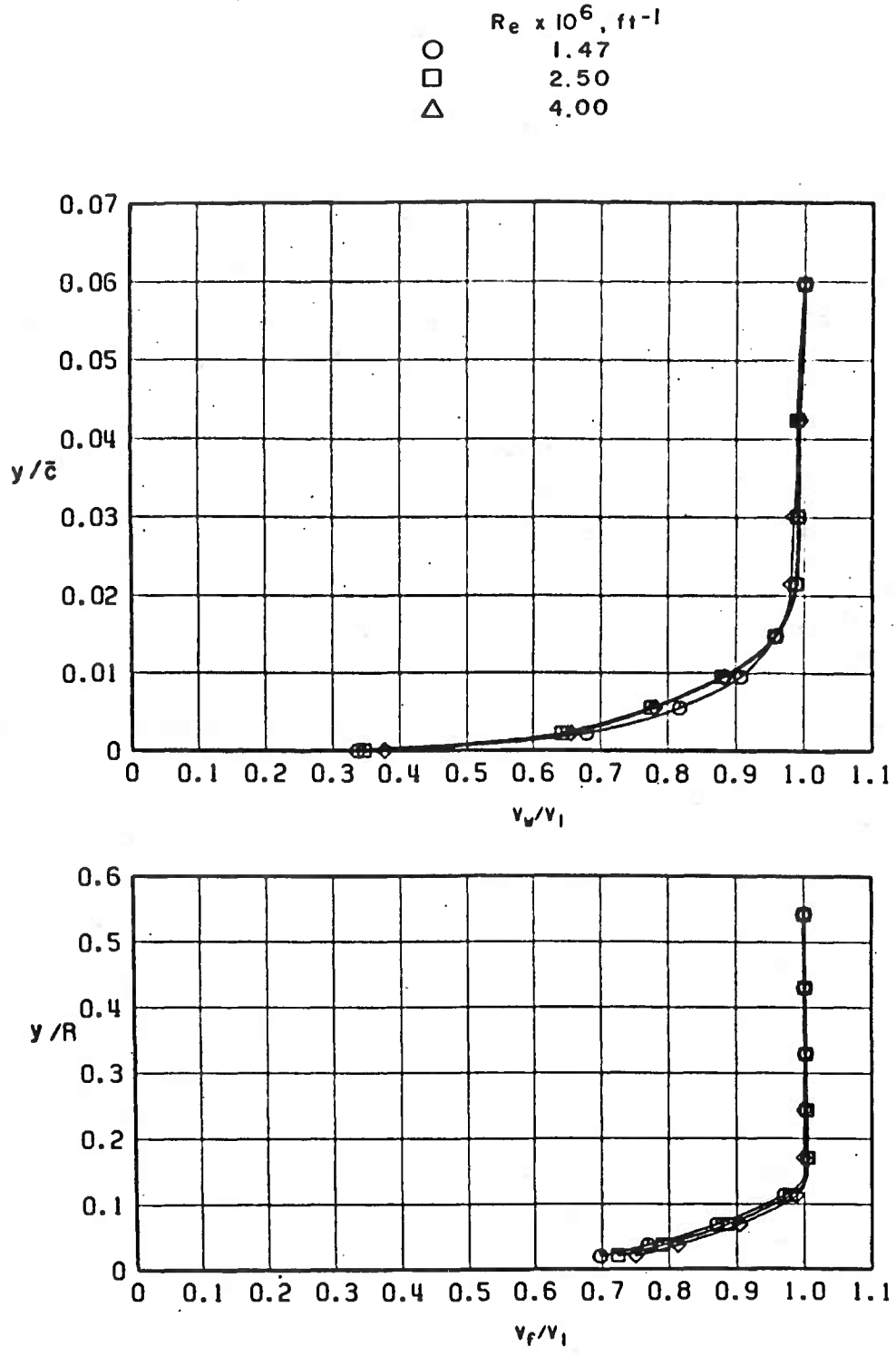

d. $M_\infty = 1.20$

Figure 18. Concluded.

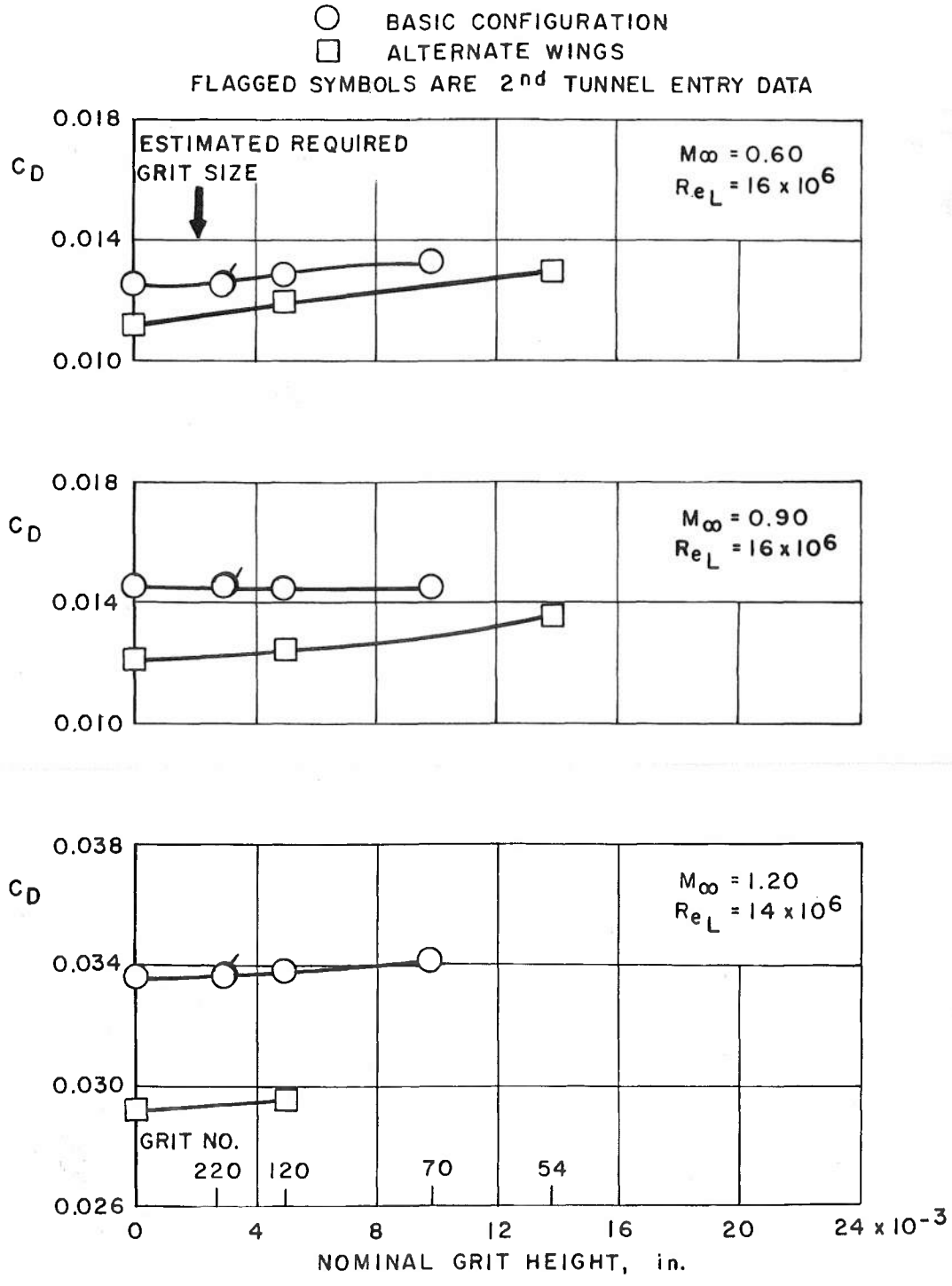

Figure 19. Effect of grit size on drag coefficient, 4.7-percent scale model, α = 0.

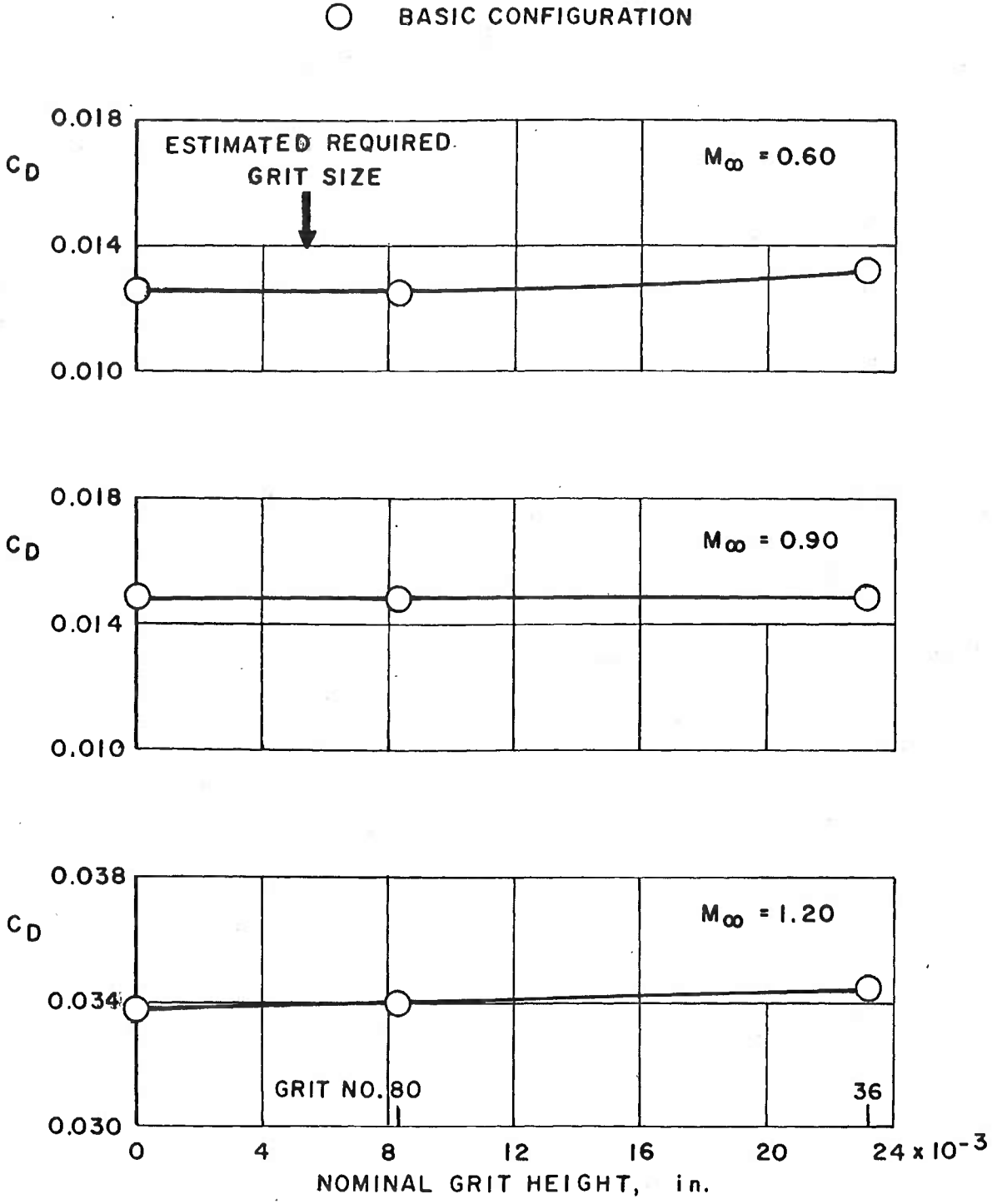

Figure 20. Effect of grit size on drag coefficient, 13-percent scale model, $Re_L = 21 \times 10^6$, $\alpha = 0$.

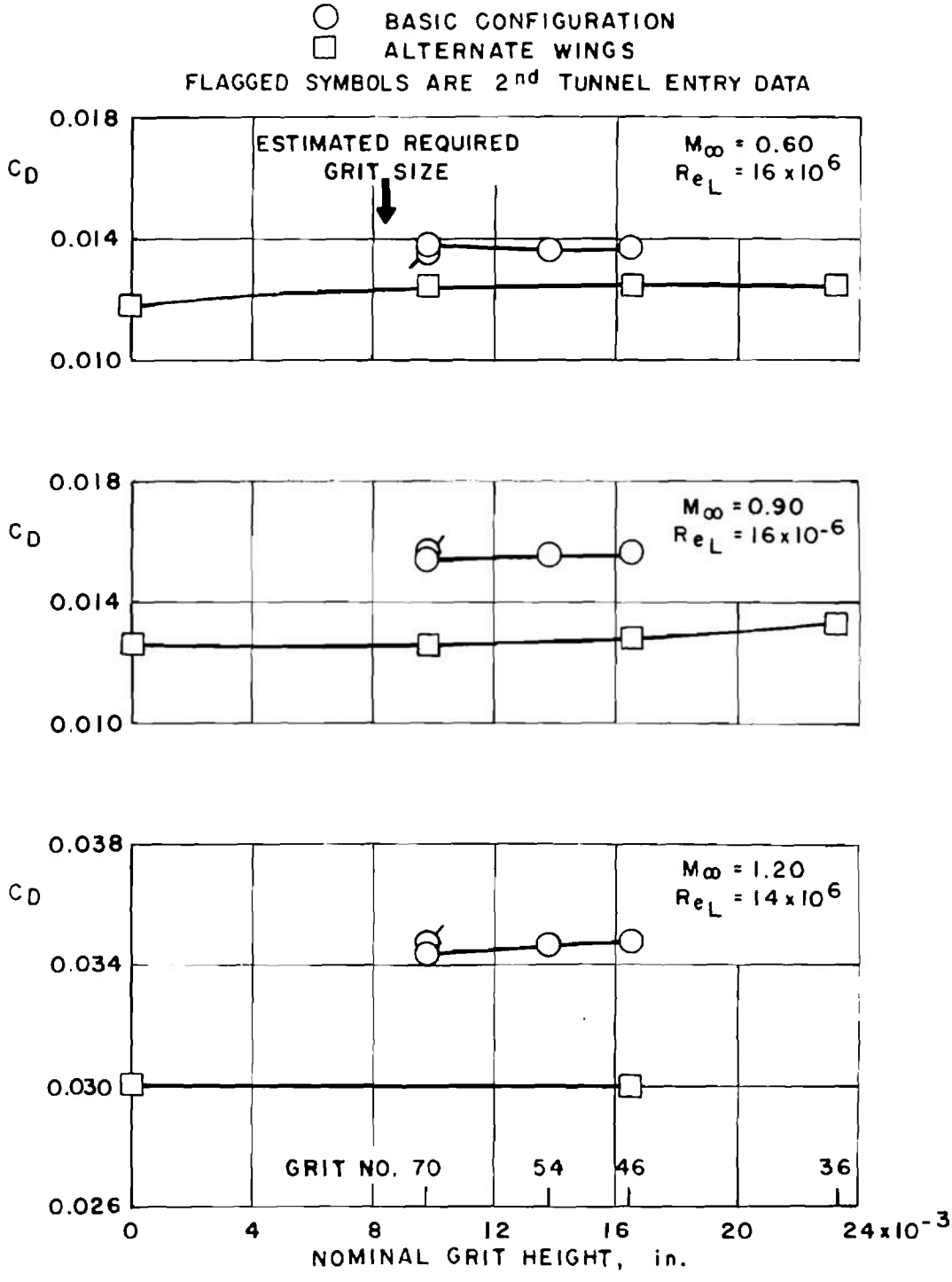

Figure 21. Effect of grit size on drag coefficient, 17-percent scale model, α = 0.

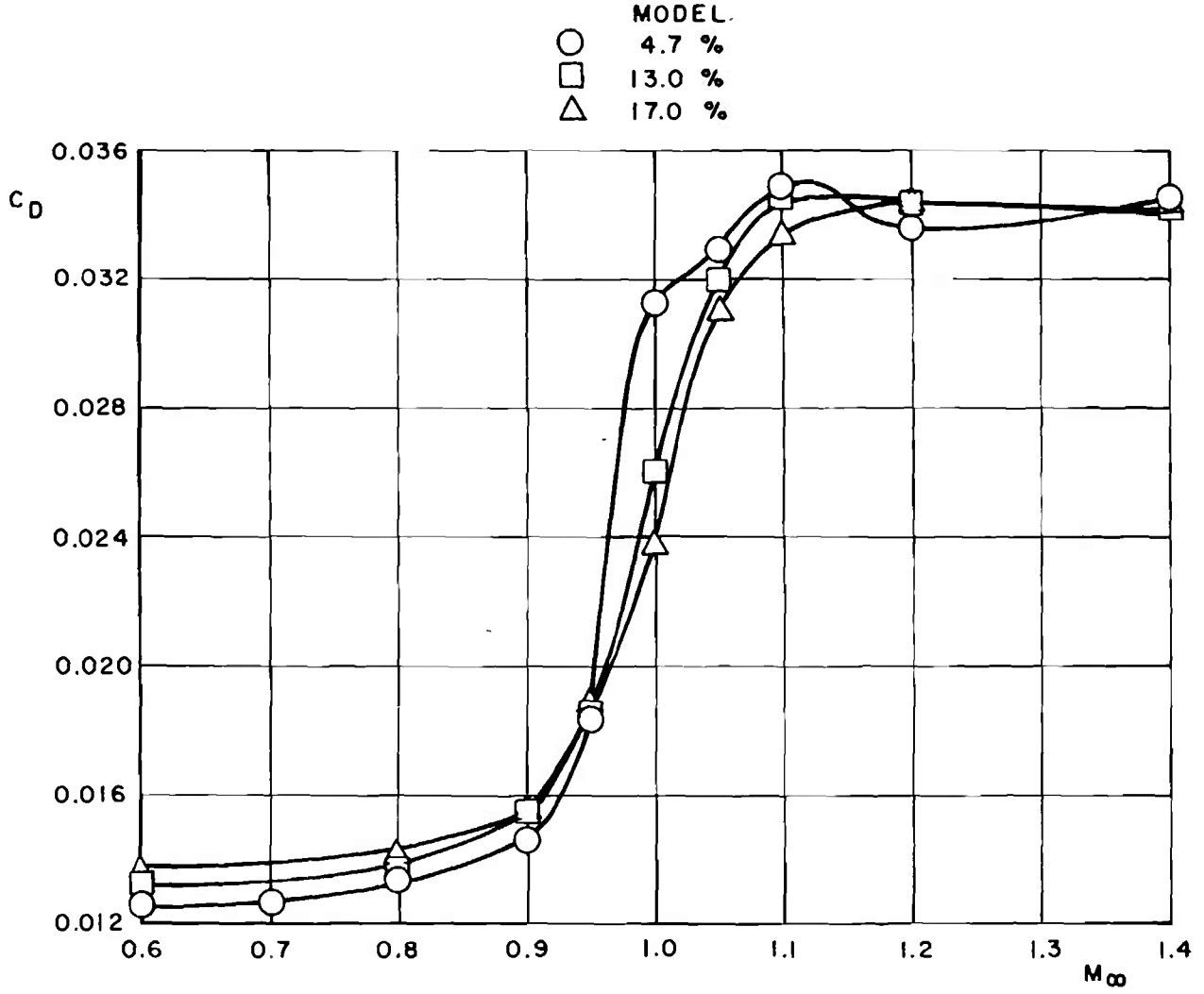

Figure 22. Drag coefficient for basic configuration, nominal characteristic Reynolds number schedule, α = 0.

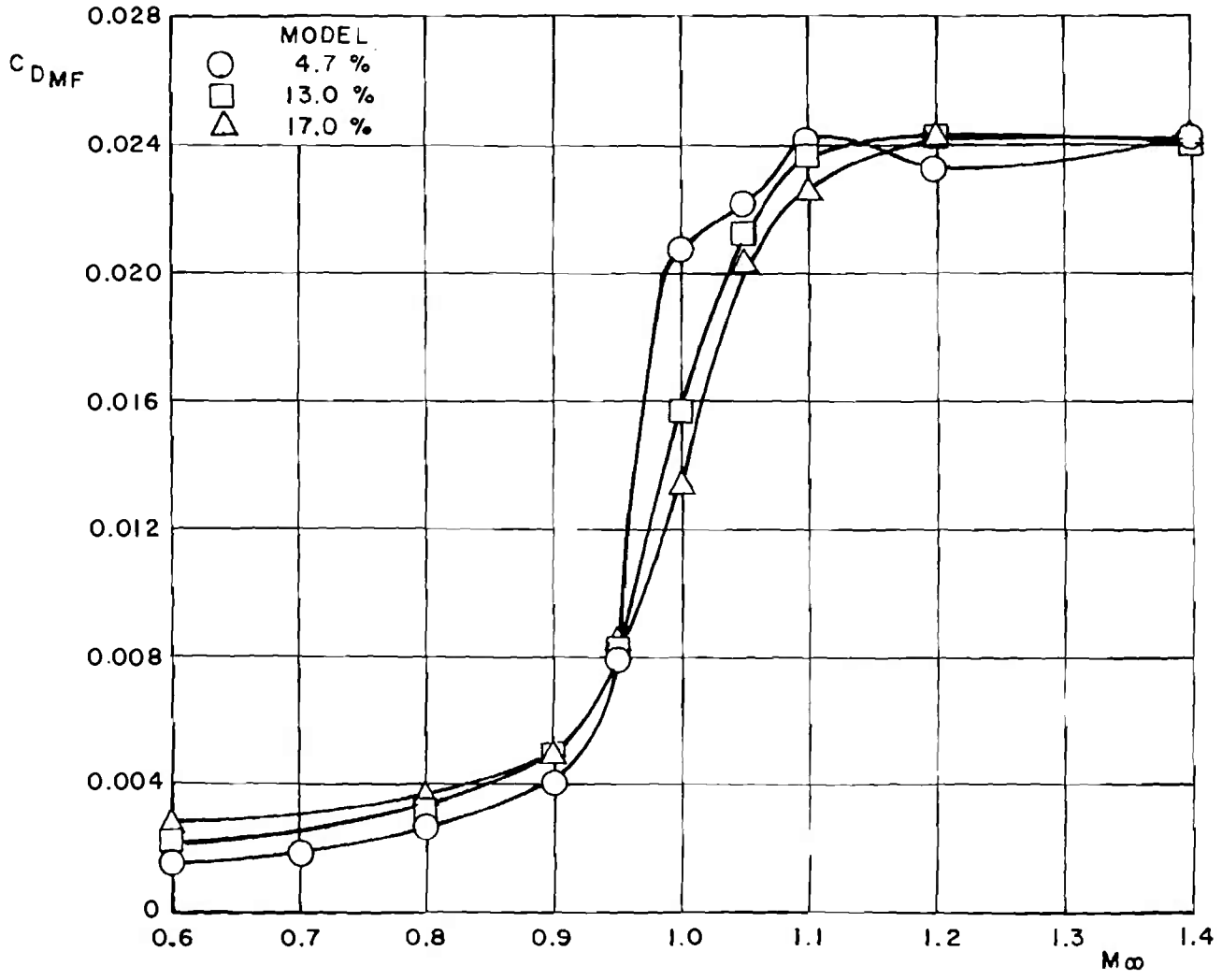

Figure 23. Pressure drag coefficient for basic configuration, nominal characteristic Reynolds number schedule, α = 0.

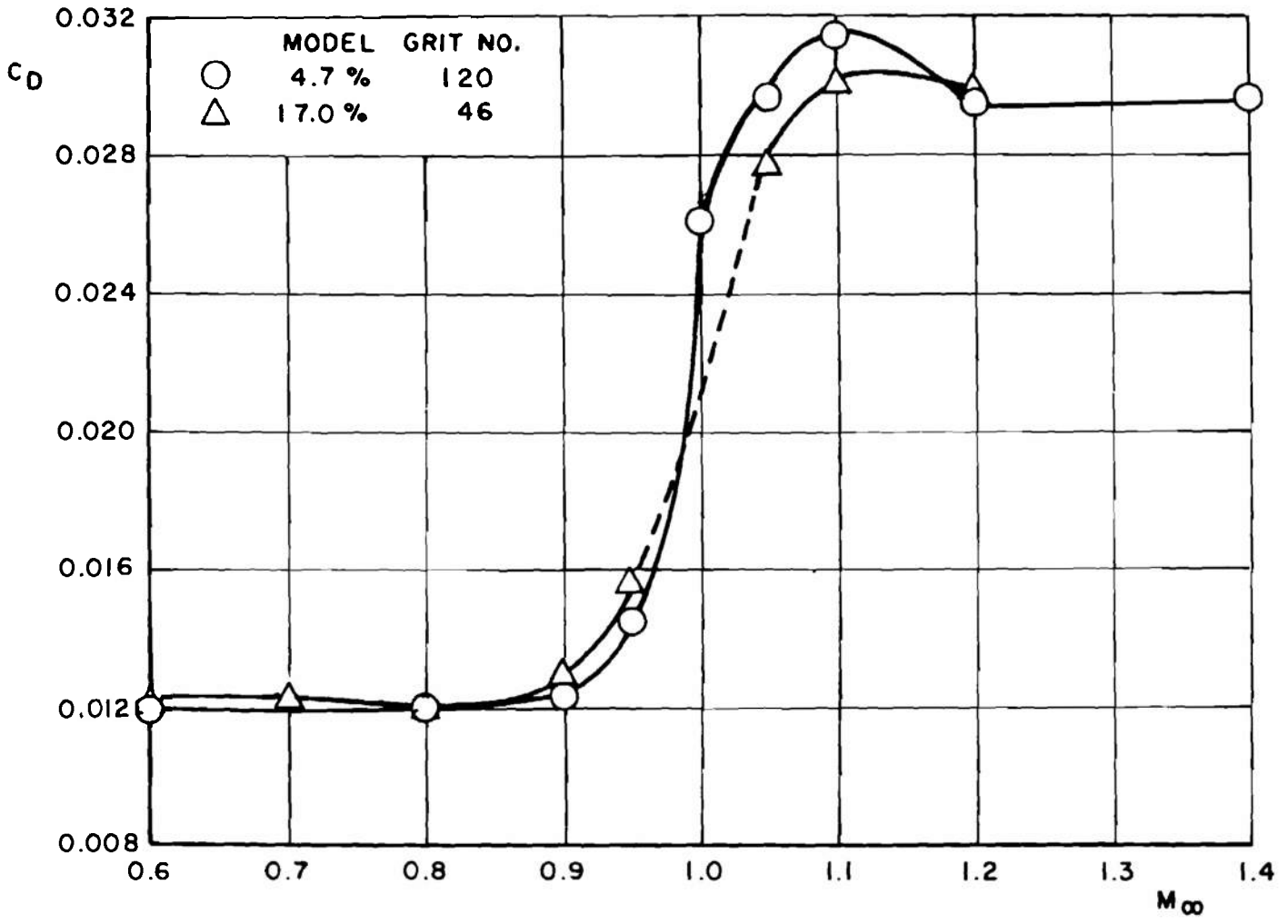

Figure 24. Drag coefficient for alternate wing configuration, nominal characteristic Reynolds number schedule, α = 0.

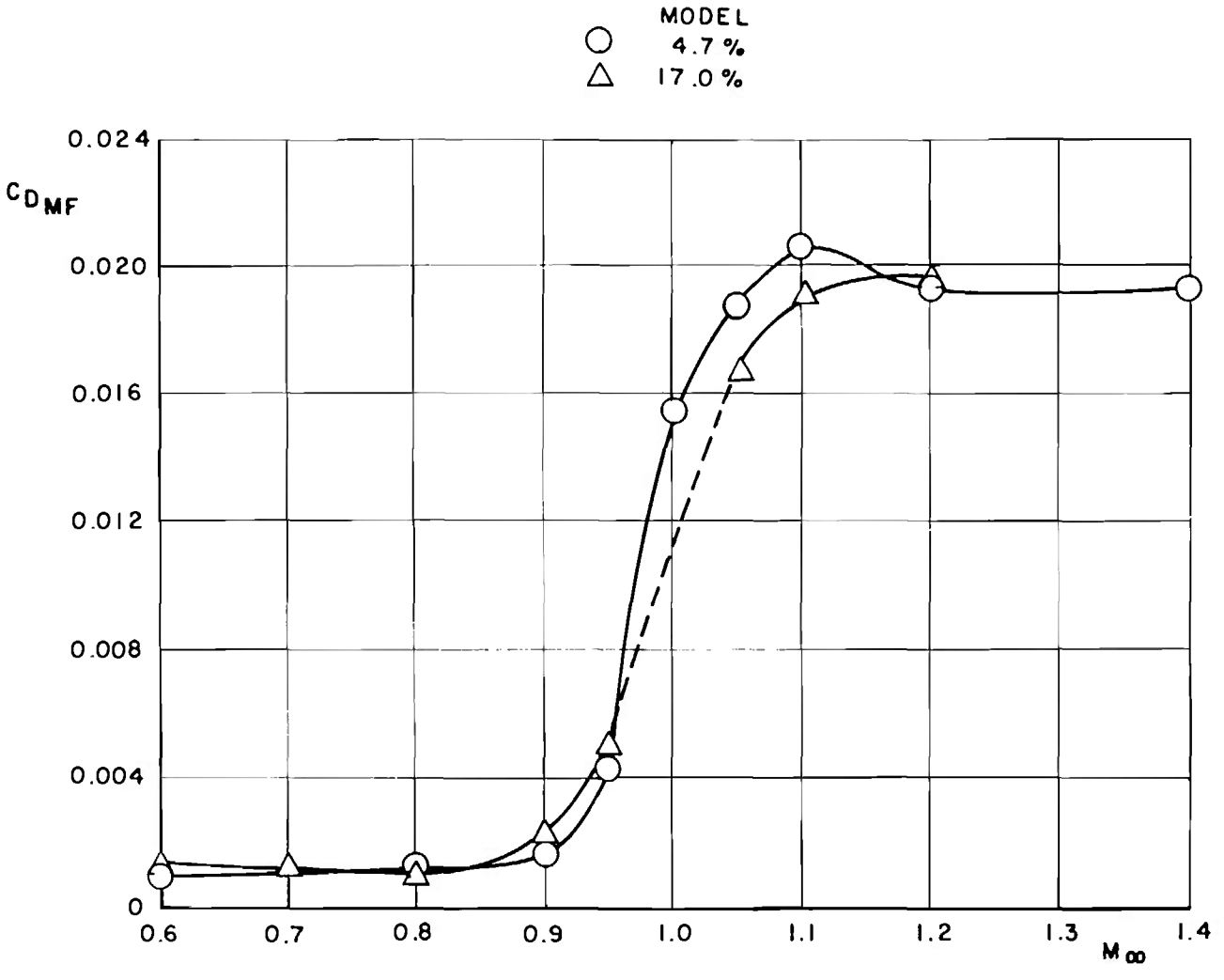

Figure 25. Pressure drag coefficient for alternate wing configuration, nominal characteristic Reynolds number schedule, α = 0.

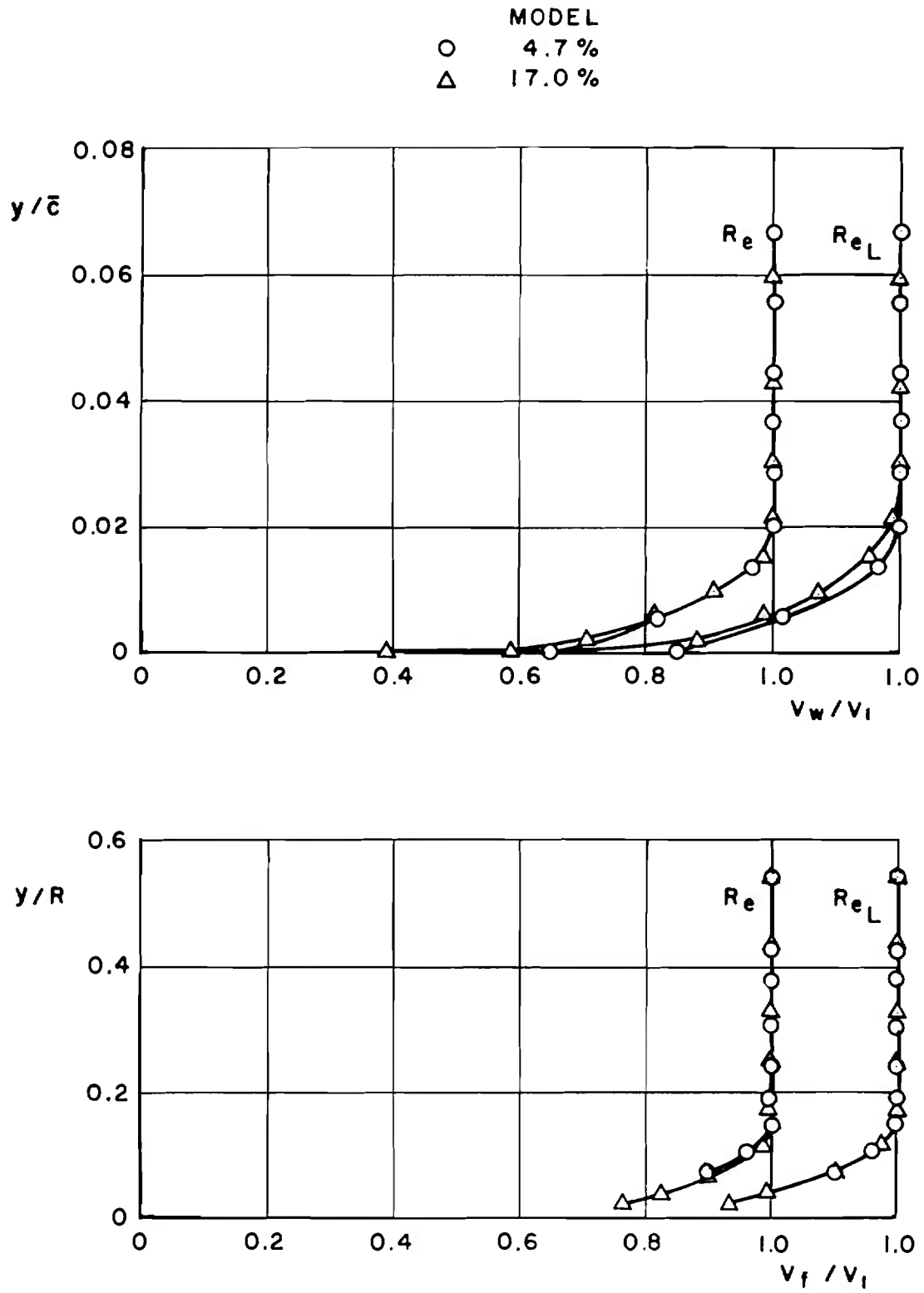

Figure 26. Boundary-layer profiles compared at characteristic Reynolds number = 16 x 10^6 and unit Reynolds number = 5.3 x 10^6 ft^{-1}, M_∞ = 0.6, α = 0.

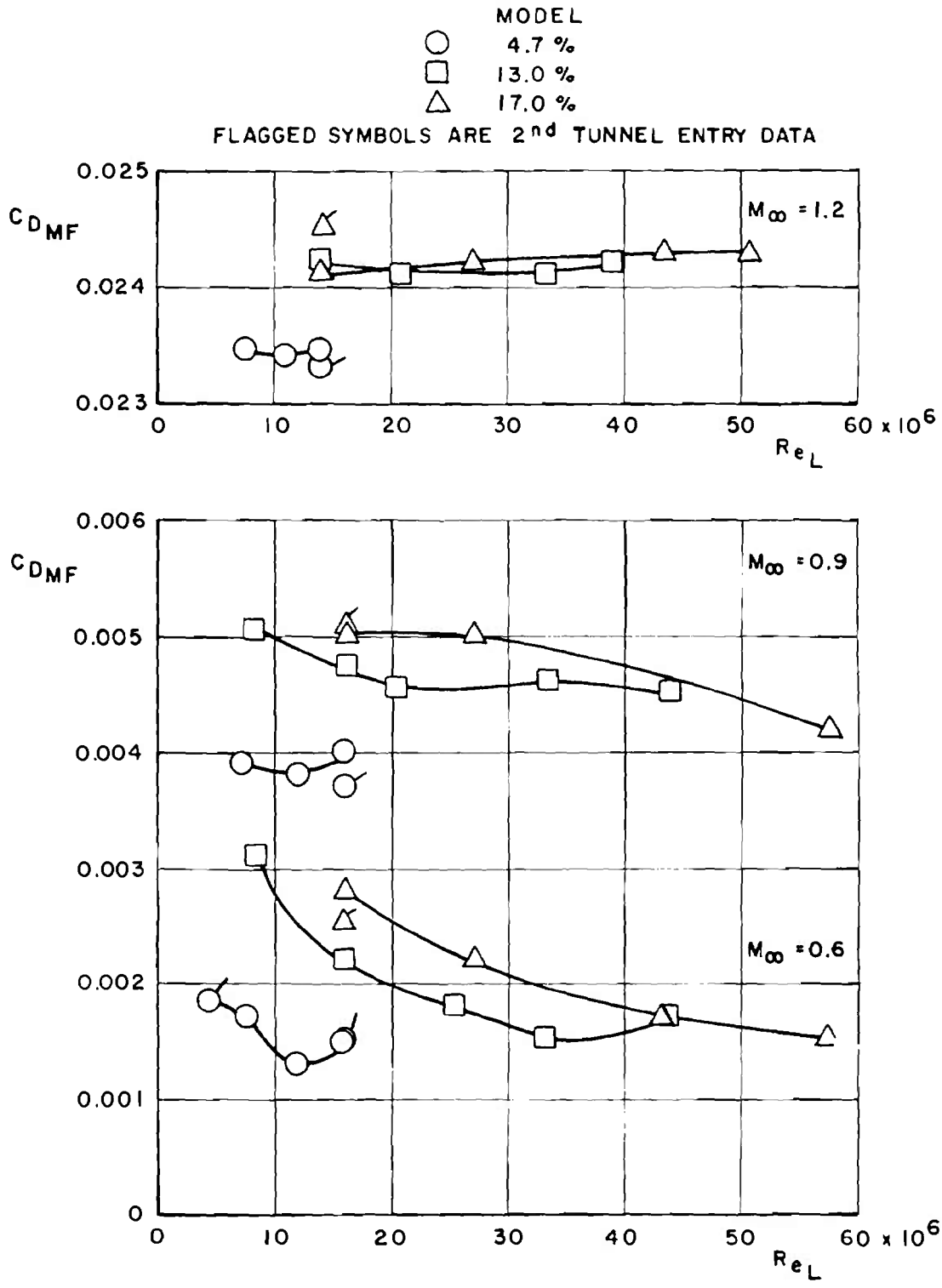

Figure 27. Pressure drag coefficient as a function of characteristic Reynolds number, α = 0.

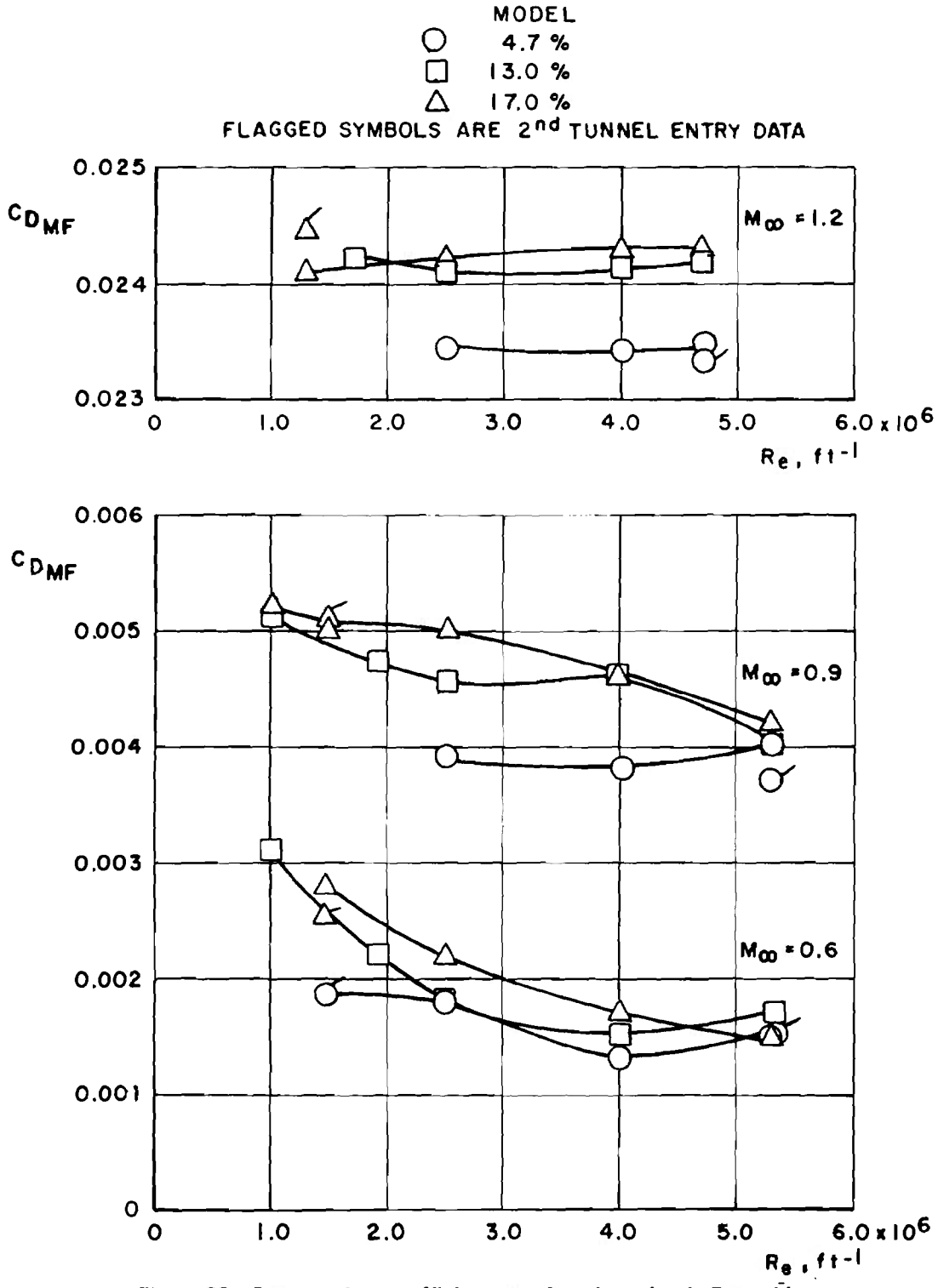

Figure 28. Pressure drag coefficient as a function of unit Reynolds number, α = 0

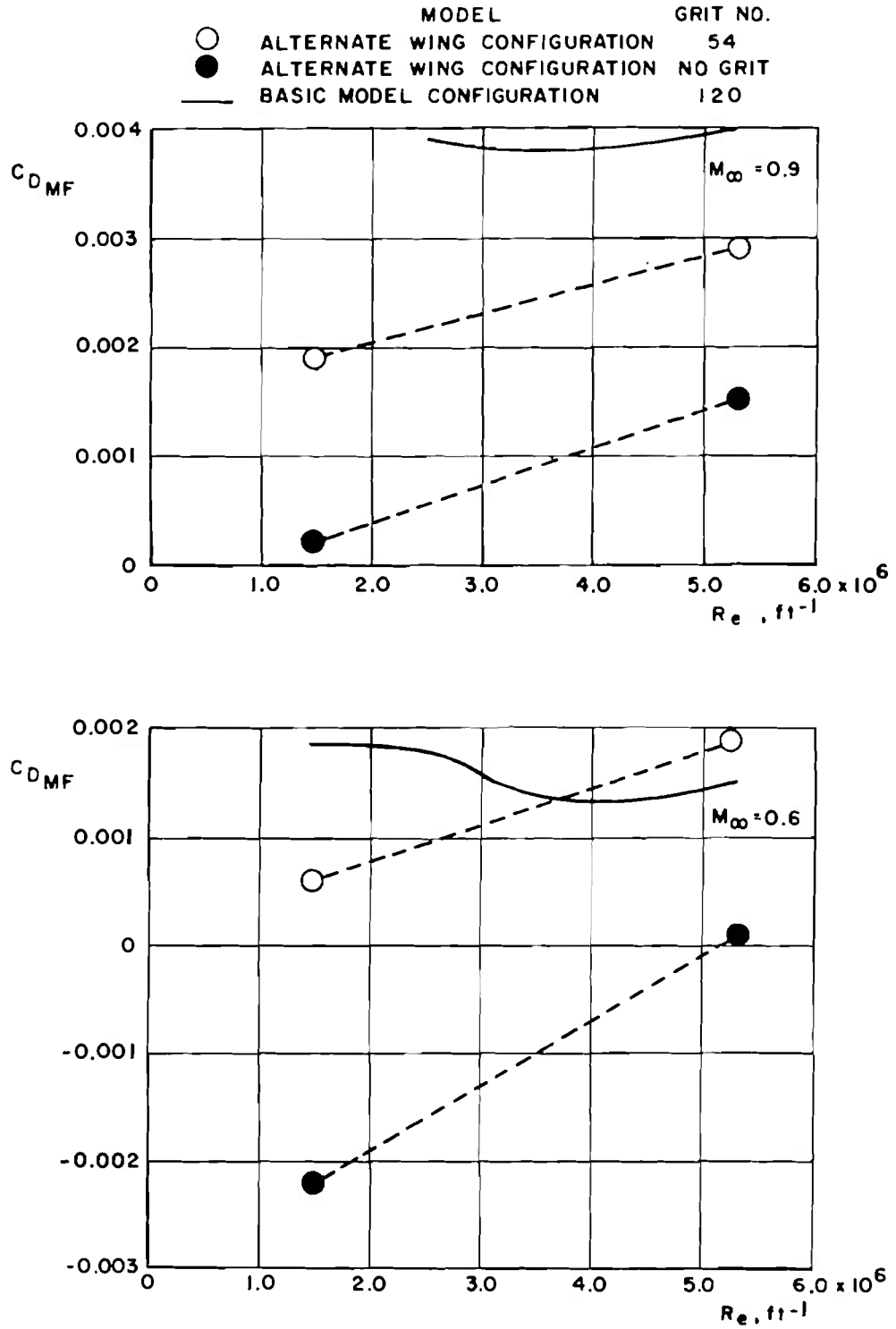

Figure 29. Pressure drag coefficient as a function of unit Reynolds number for 4.7-percent model, α = 0.

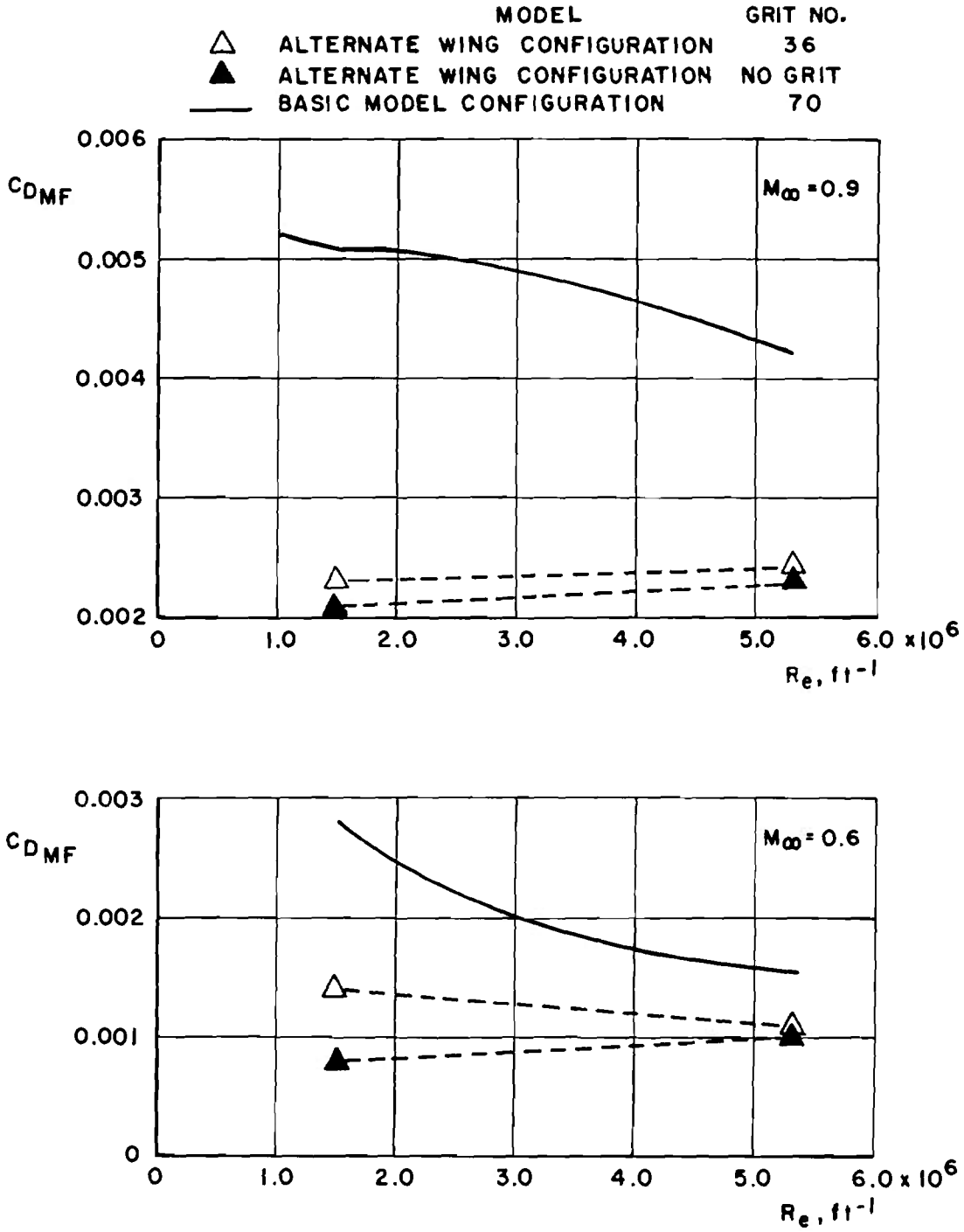

Figure 30. Pressure drag coefficient as a function of unit Reynolds number for 17-percent model, α = 0.

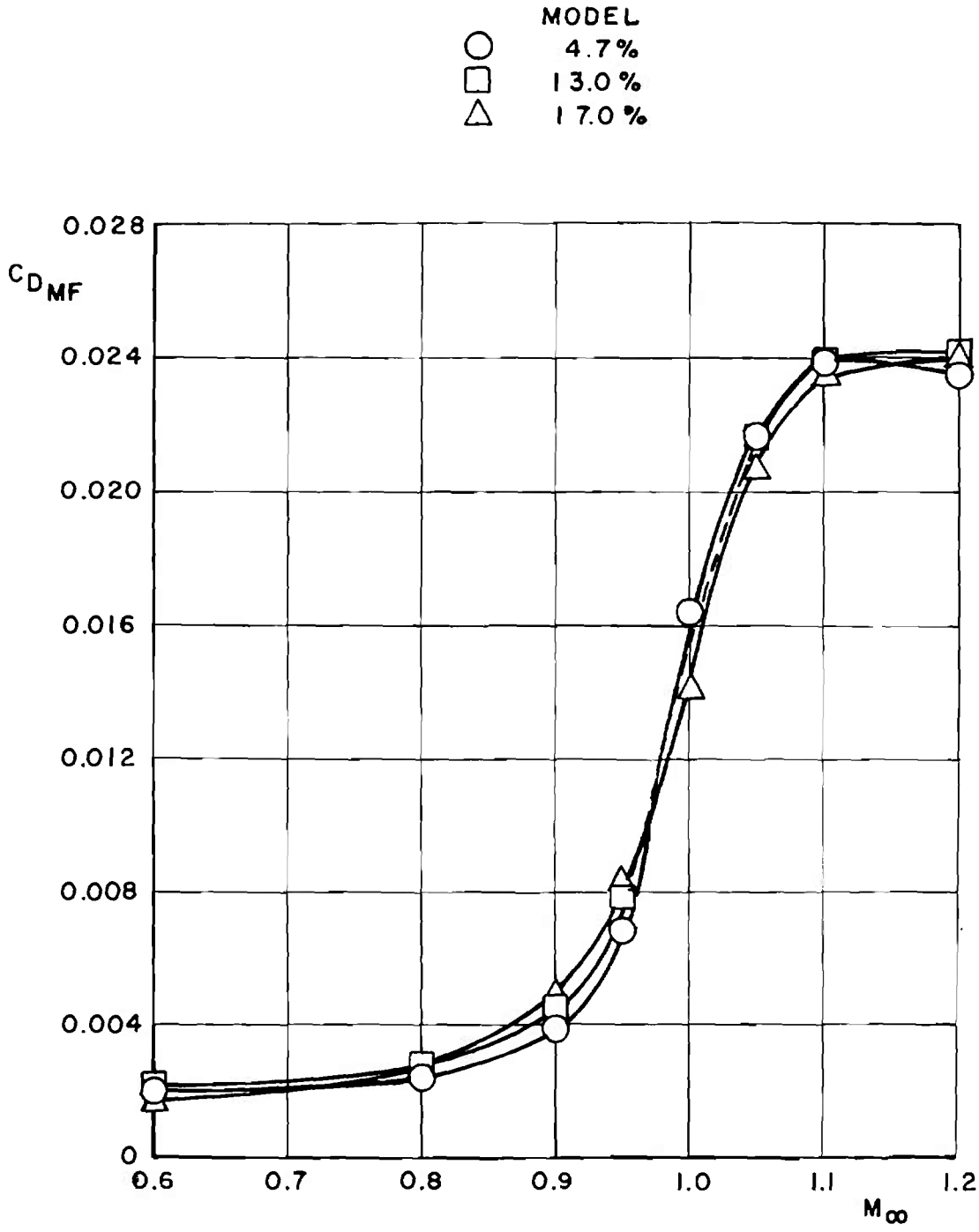

Figure 31. Pressure drag coefficient for basic configuration at constant unit Reynolds number, Re = 2.5 x 10^6 ft^{-1}, α = 0.

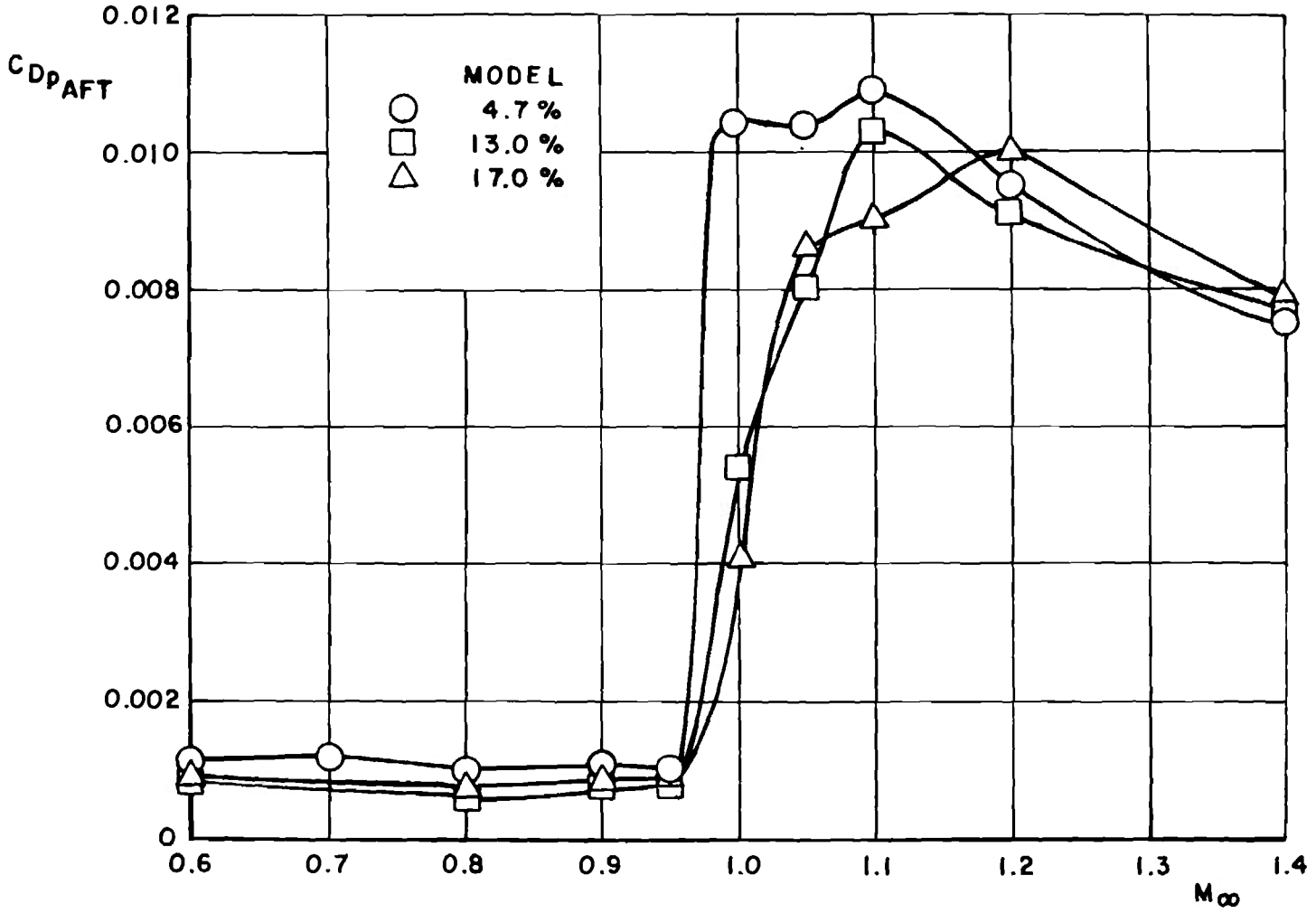

Figure 32. Integrated aft-end drag coefficient for basic configuration, nominal characteristic Reynolds number schedule, α = 0.

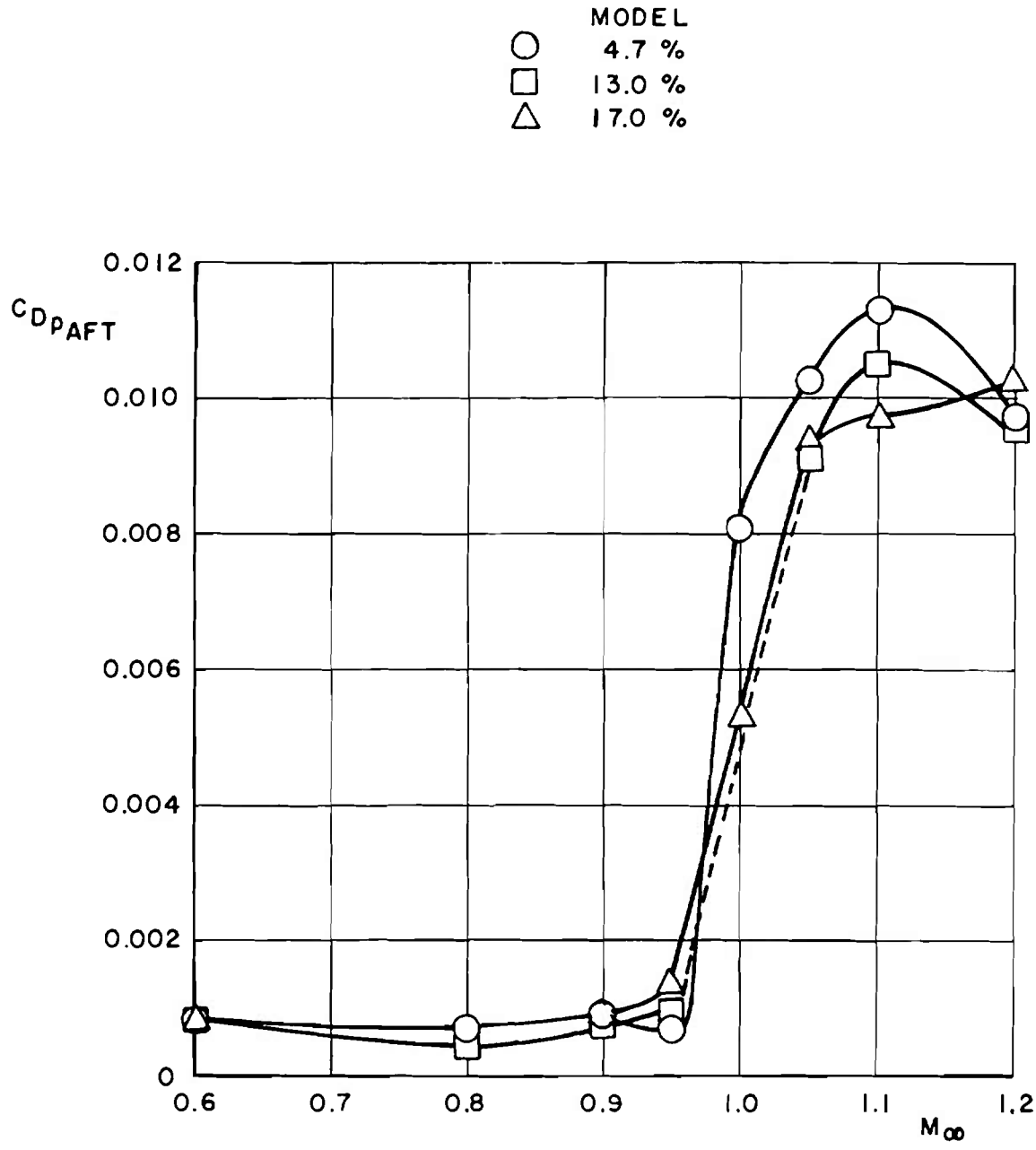

Figure 33. Integrated aft-end drag coefficient for basic configuration, Re = 2.5 x 10^6 ft^{-1}, α = 0.

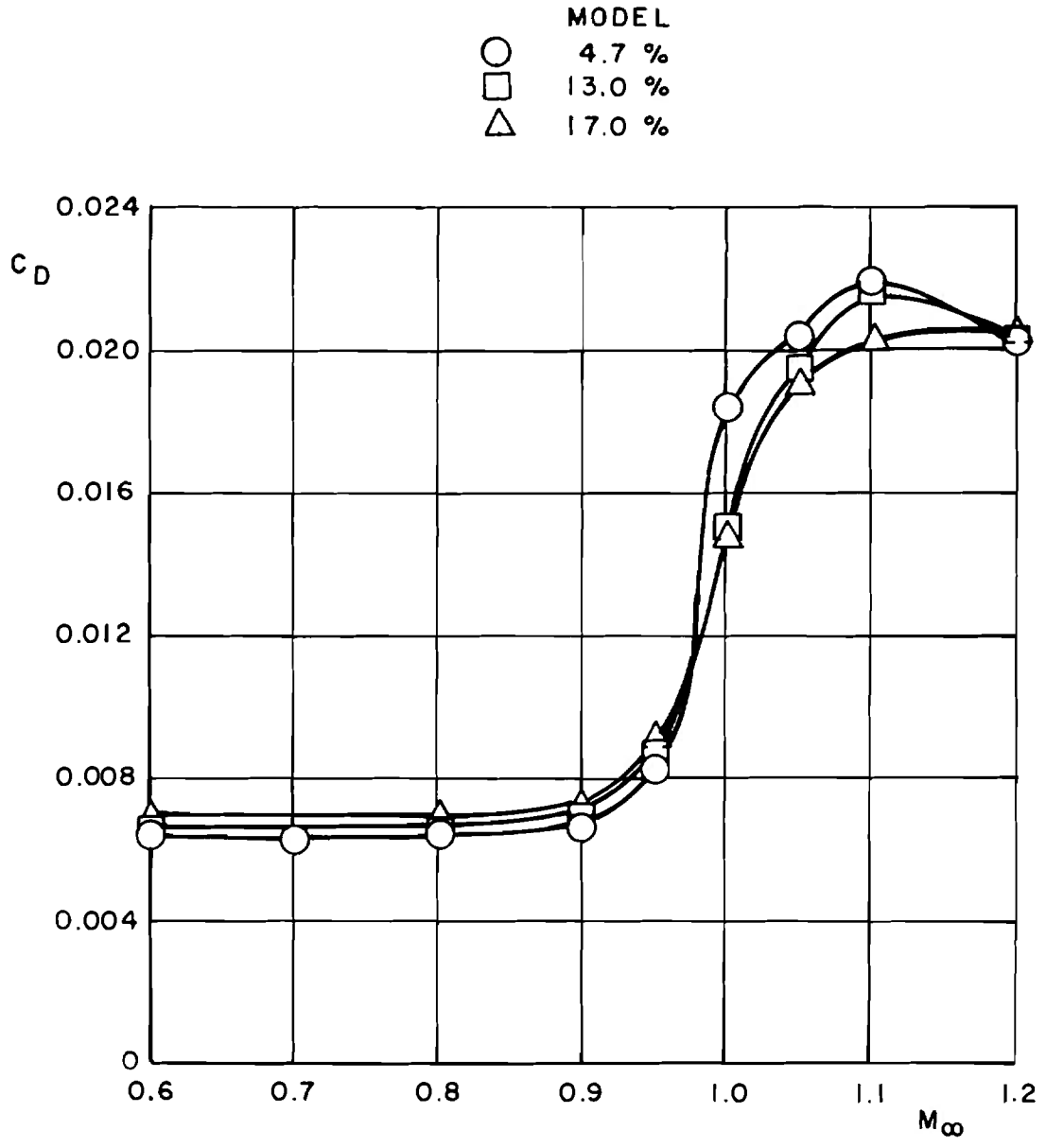

Figure 34. Drag coefficient for wings-off configuration, nominal characteristic Reynolds number schedule, α = 0.

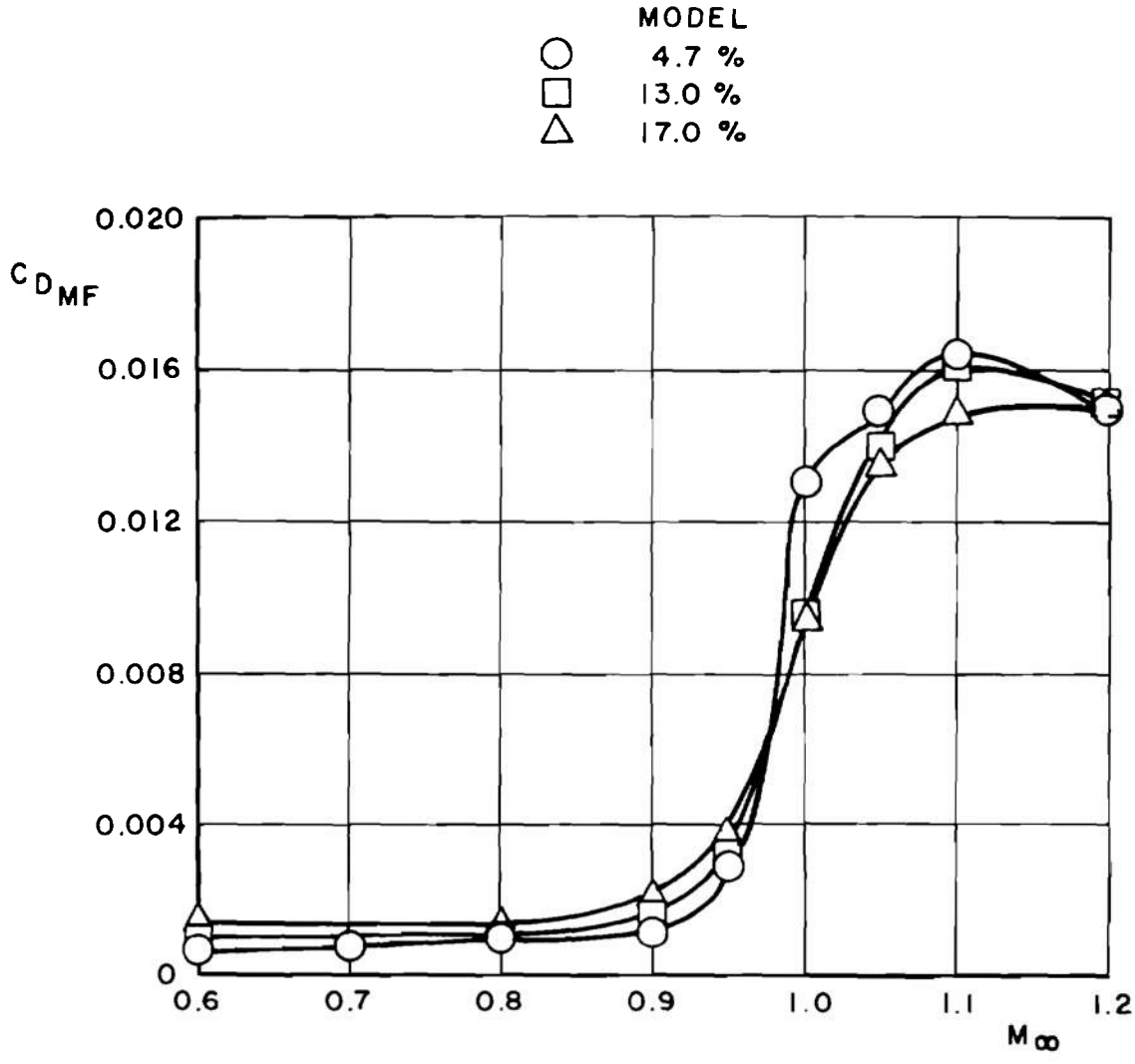

Figure 35. Pressure drag coefficient for wings-off configuration, nominal characteristic Reynolds number schedule, α = 0.

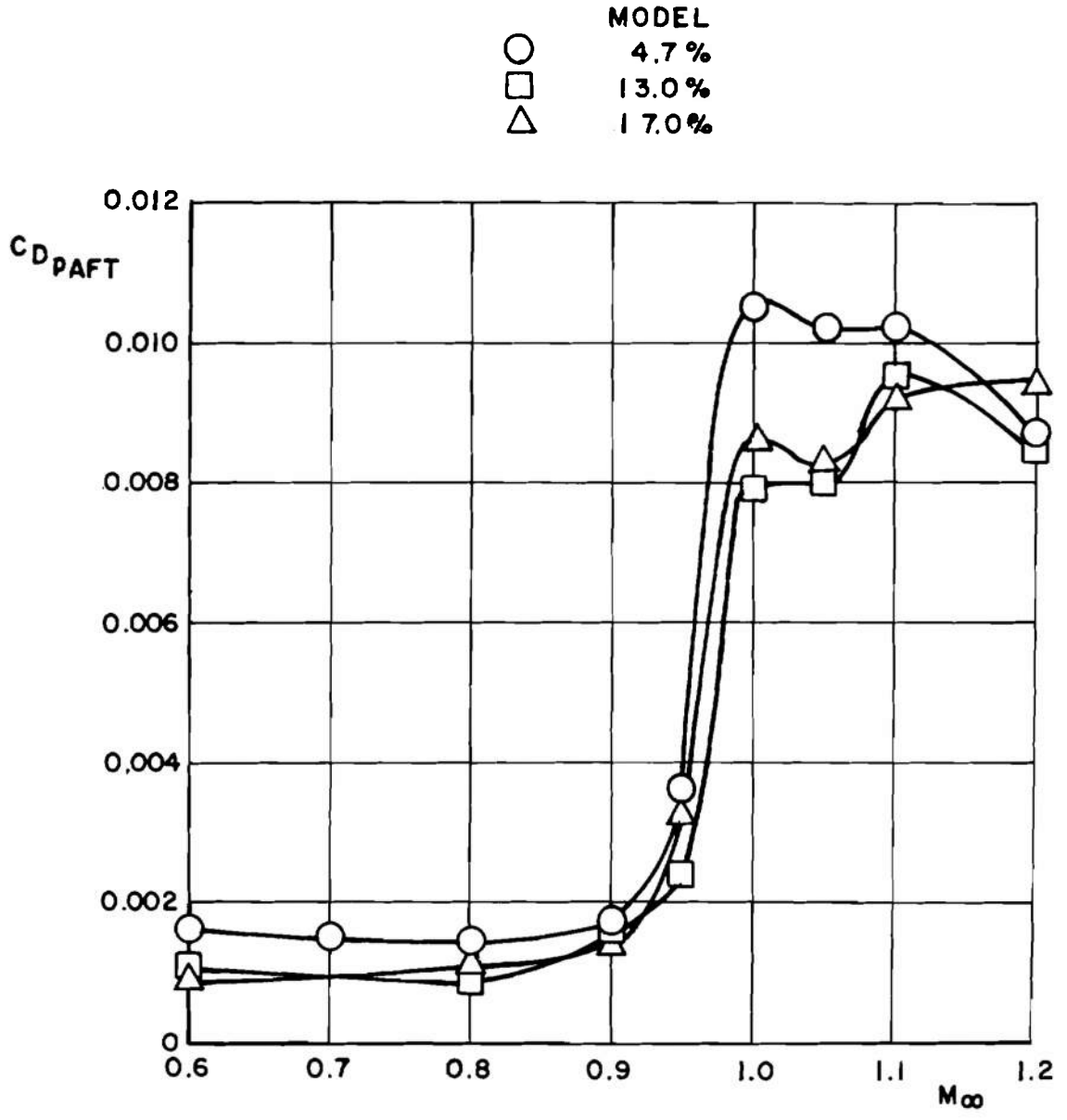

Figure 36. Integrated aft-end drag coefficient for wings-off configuration, nominal characteristic Reynolds number schedule, α = 0.

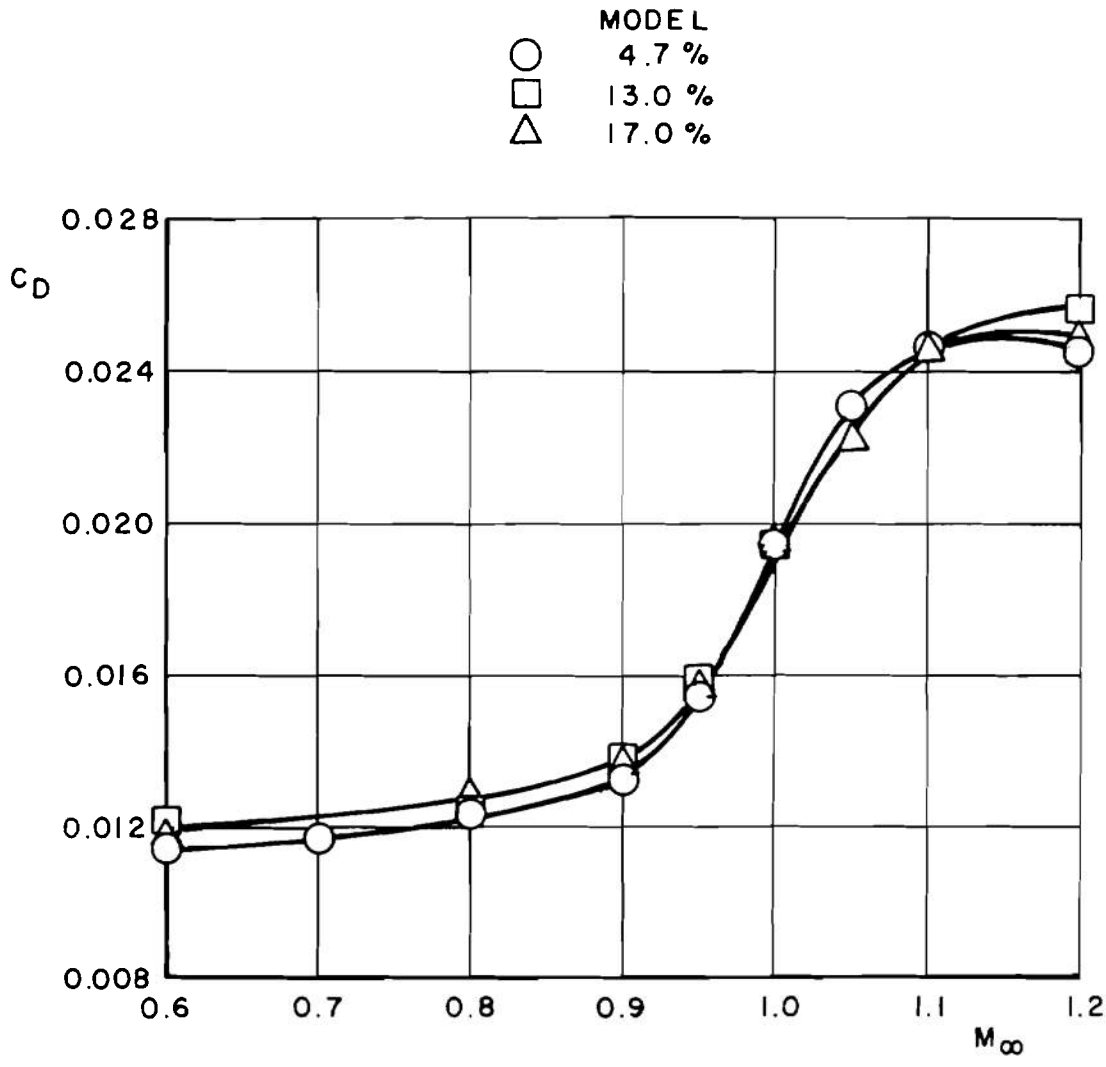

Figure 37. Drag coefficient for cylindrical afterbody configuration, wings on, nominal characteristic Reynolds number schedule, $\alpha = 0$.

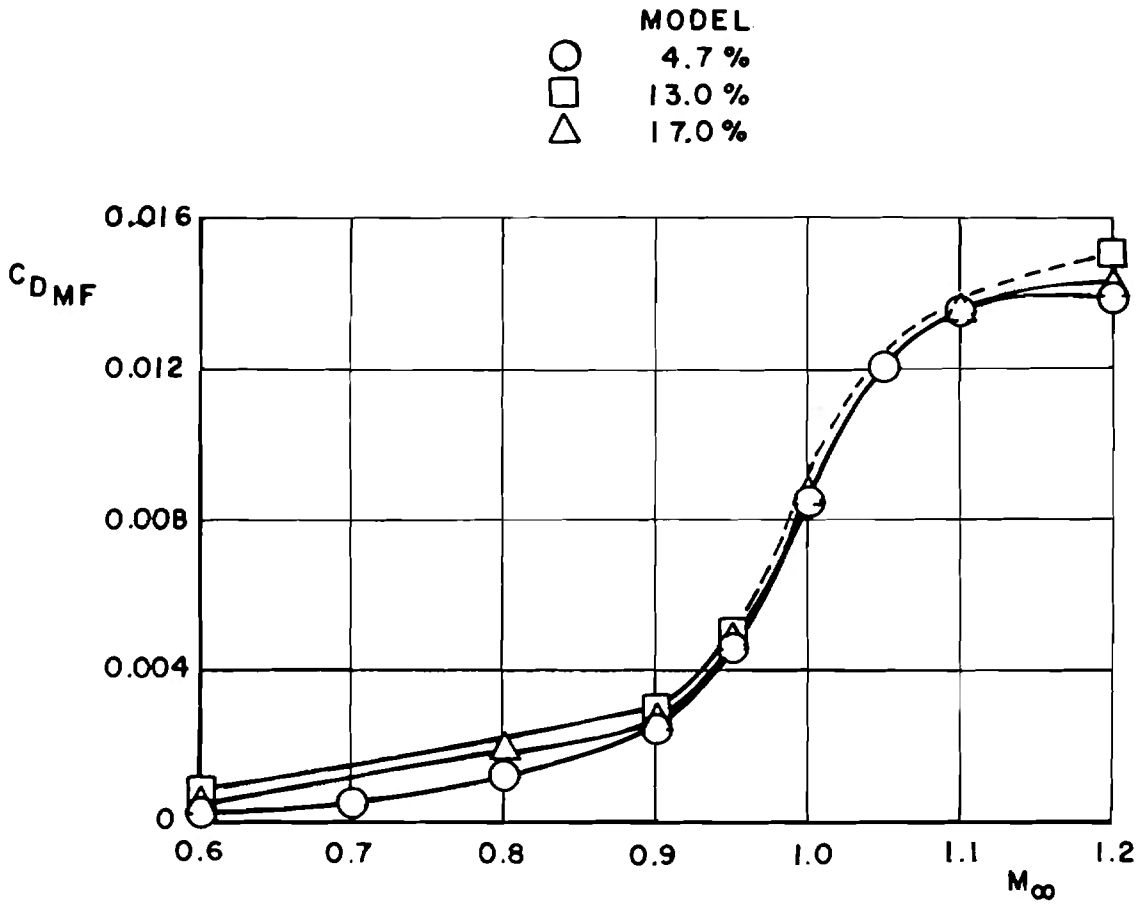

Figure 38. Pressure drag coefficient for cylindrical afterbody configuration, wings on, nominal characteristic Reynolds number schedule, $\alpha = 0$.

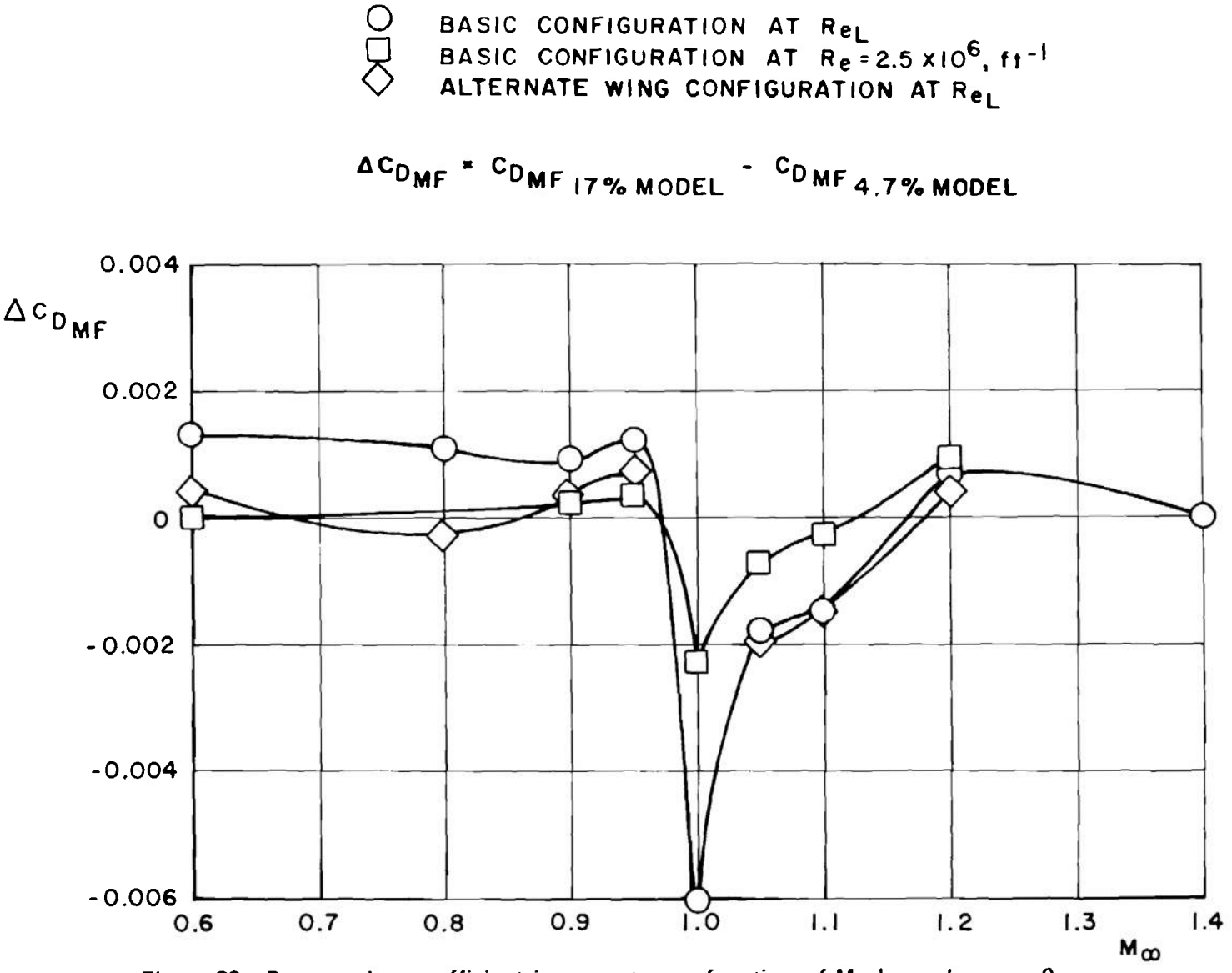

Figure 39. Pressure drag coefficient increments as a function of Mach number, α = 0.

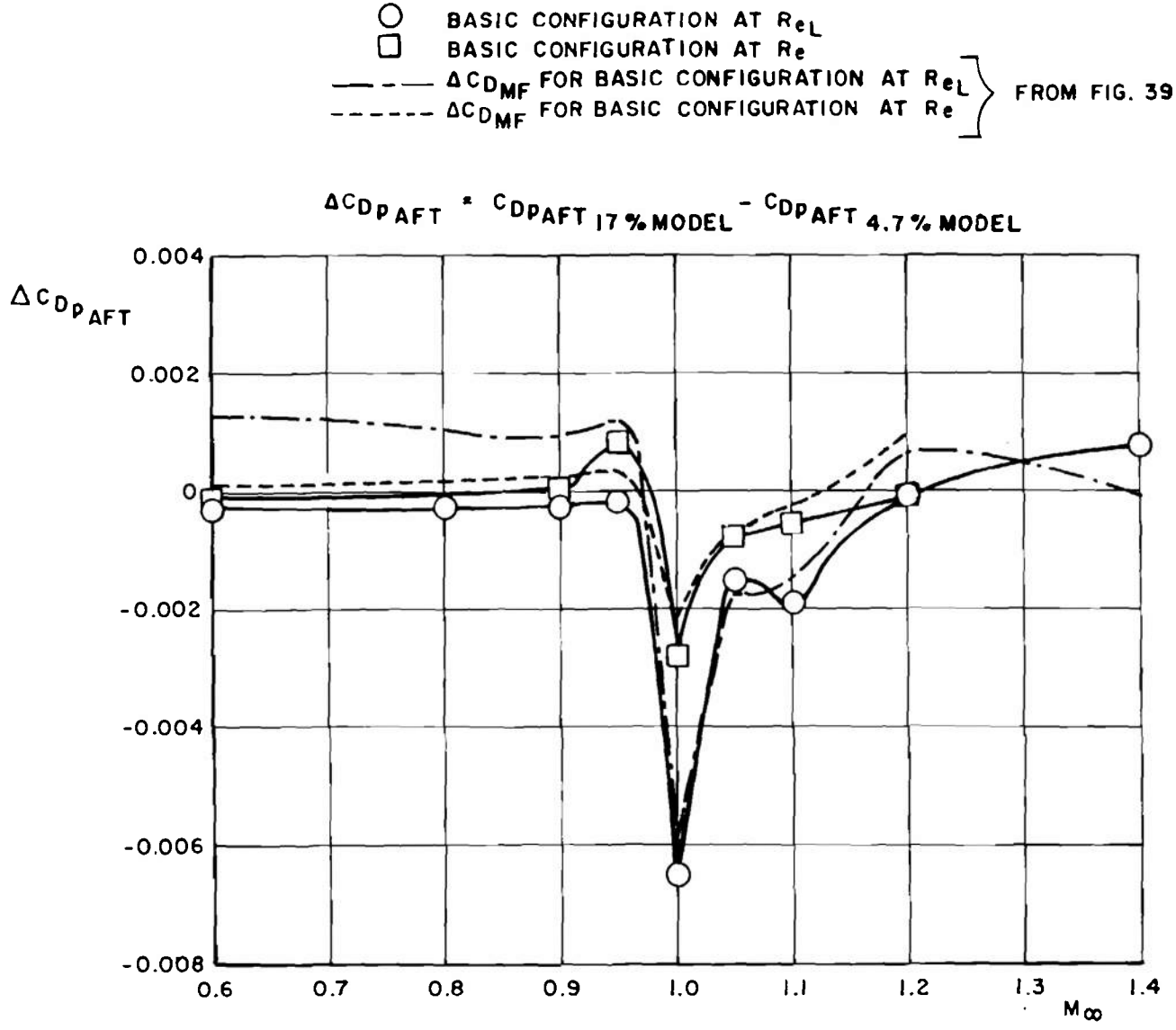

Figure 40. Integrated aft-end drag coefficient increments as a function of Mach number, α = 0.

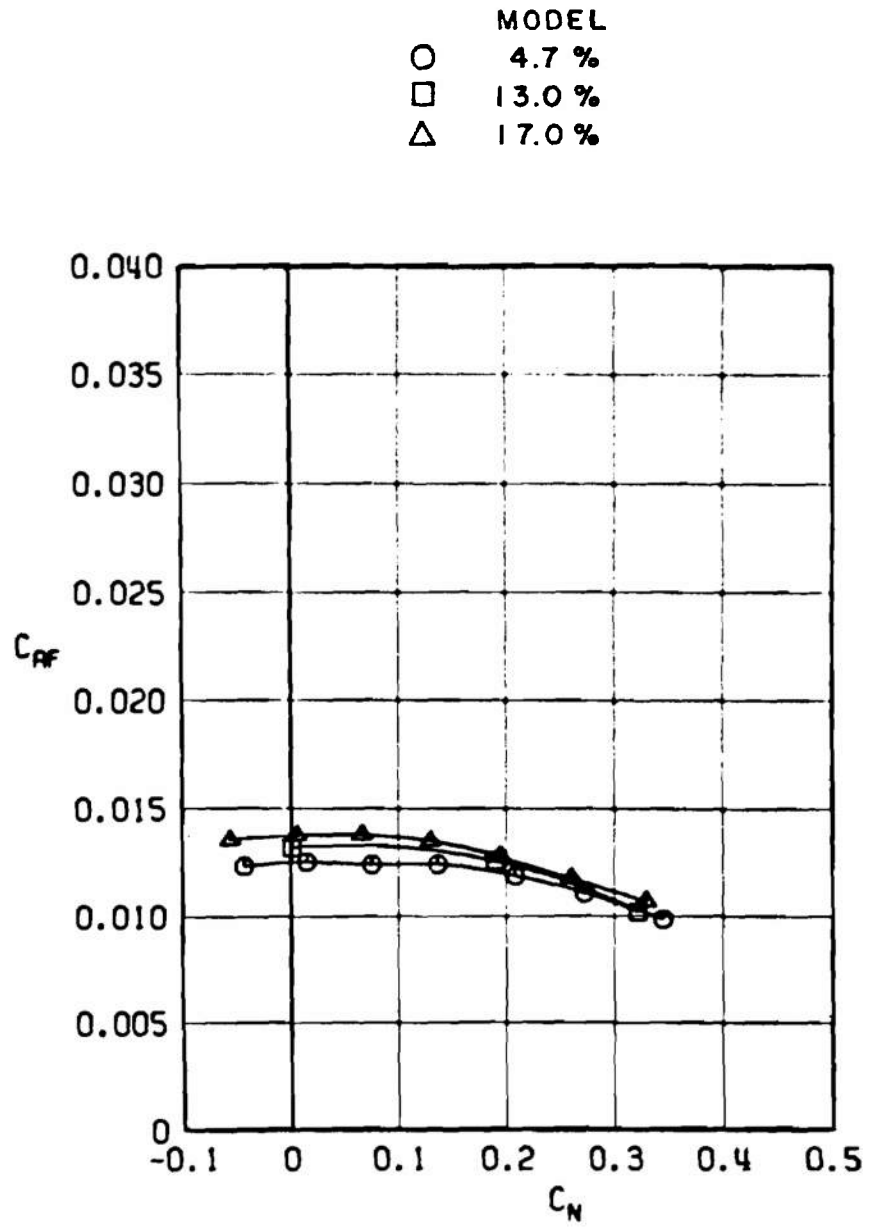

a. $M_\infty = 0.60$

Figure 41. Axial-force coefficient as a function of normal-force coefficient for basic configuration, nominal characteristic Reynolds number schedule.

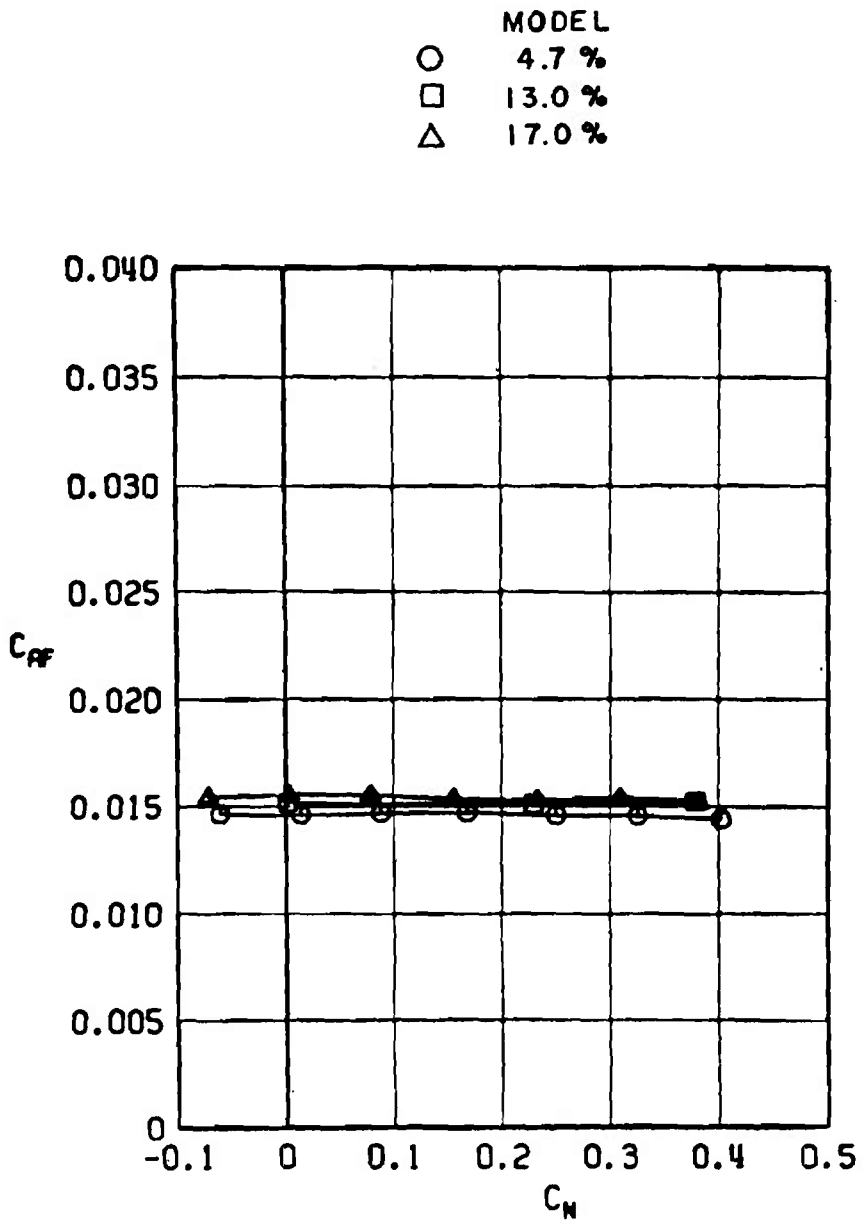

b. $M_\infty = 0.90$
Figure 41. Continued.

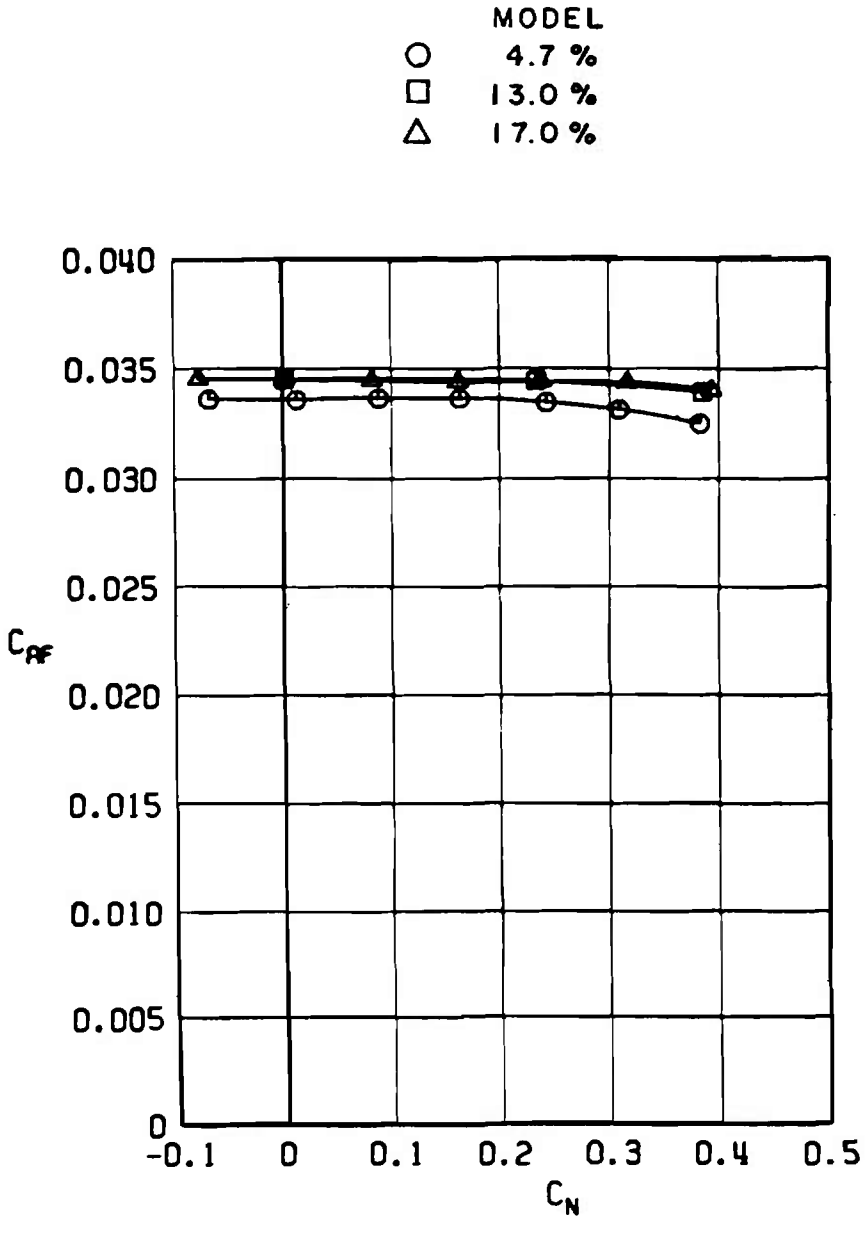

c. $M_\infty = 1.20$

Figure 41. Continued.

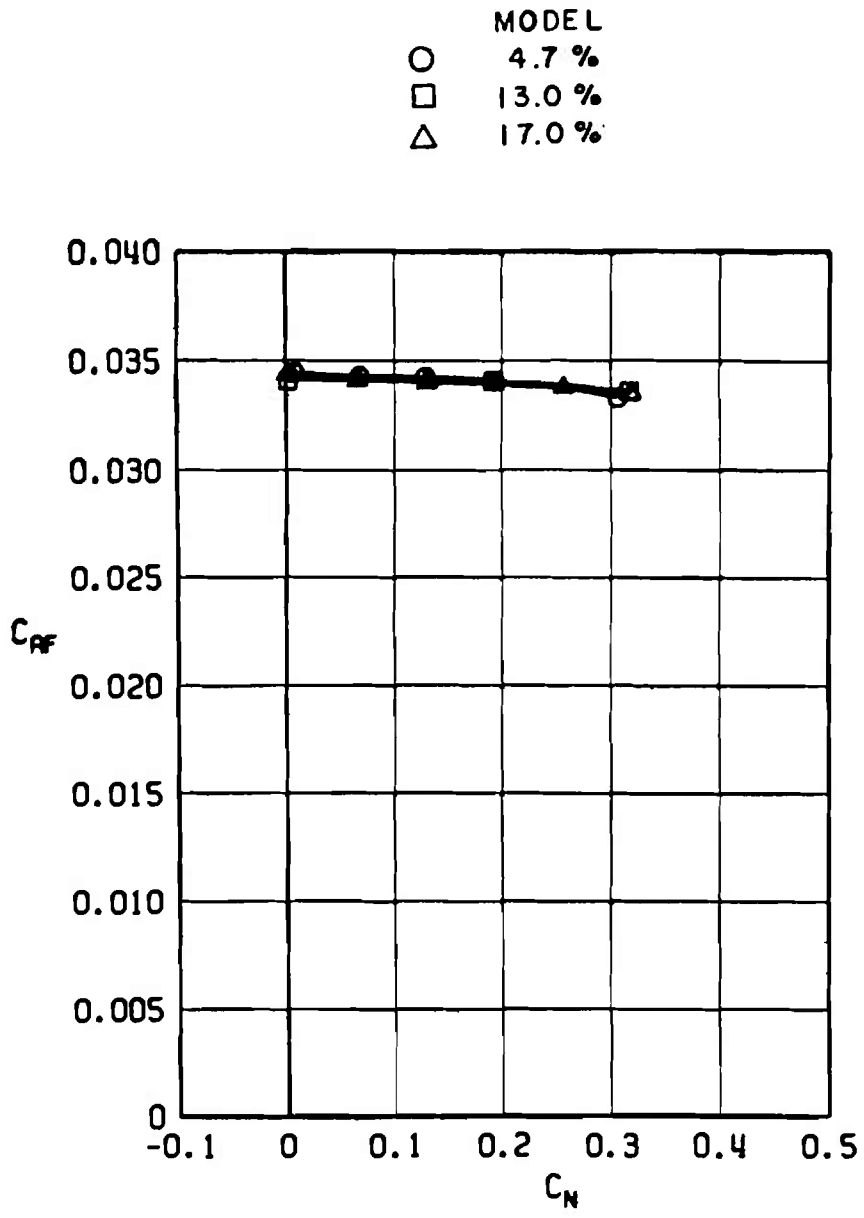

d. M_∞ = 1.40
Figure 41. Concluded.

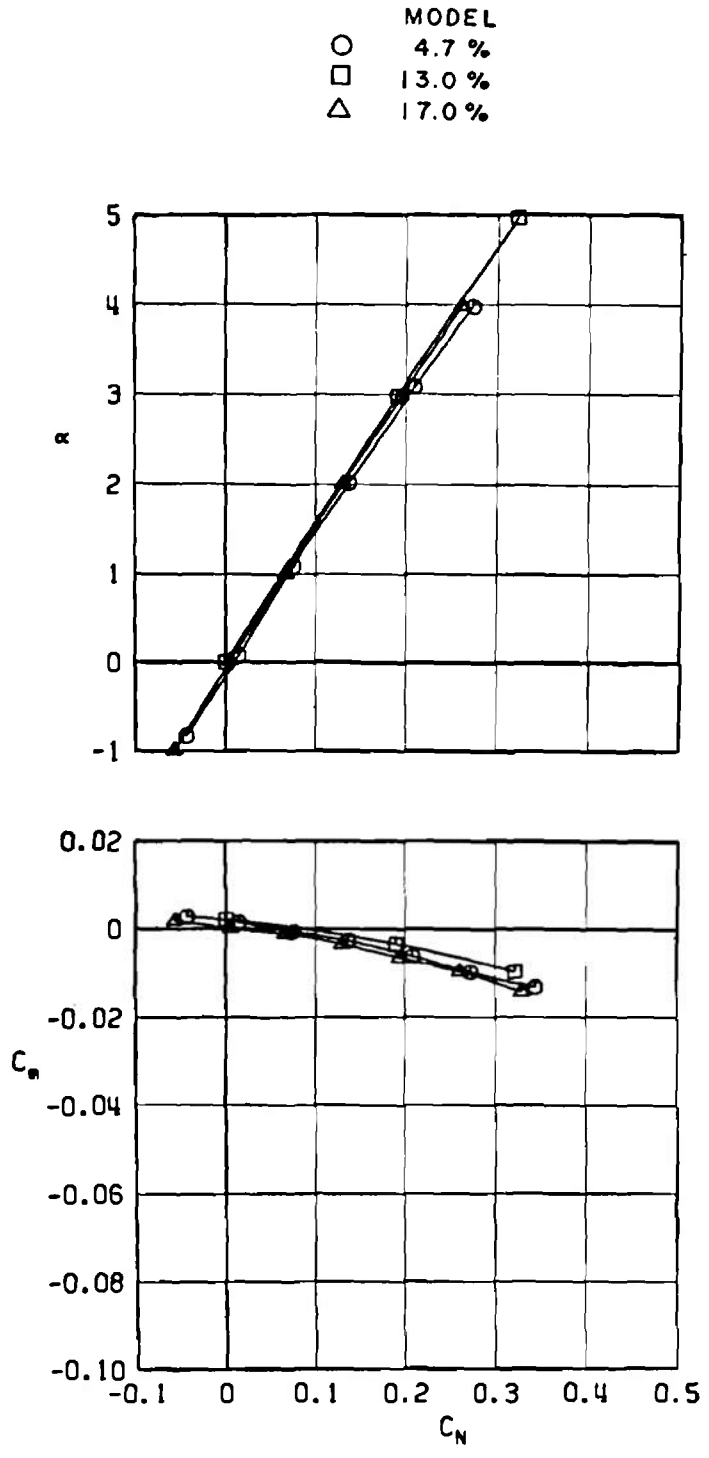

a. $M_\infty = 0.60$

Figure 42. Normal-force and pitching-moment coefficient characteristics of the basic configuration, nominal characteristic Reynolds number schedule.

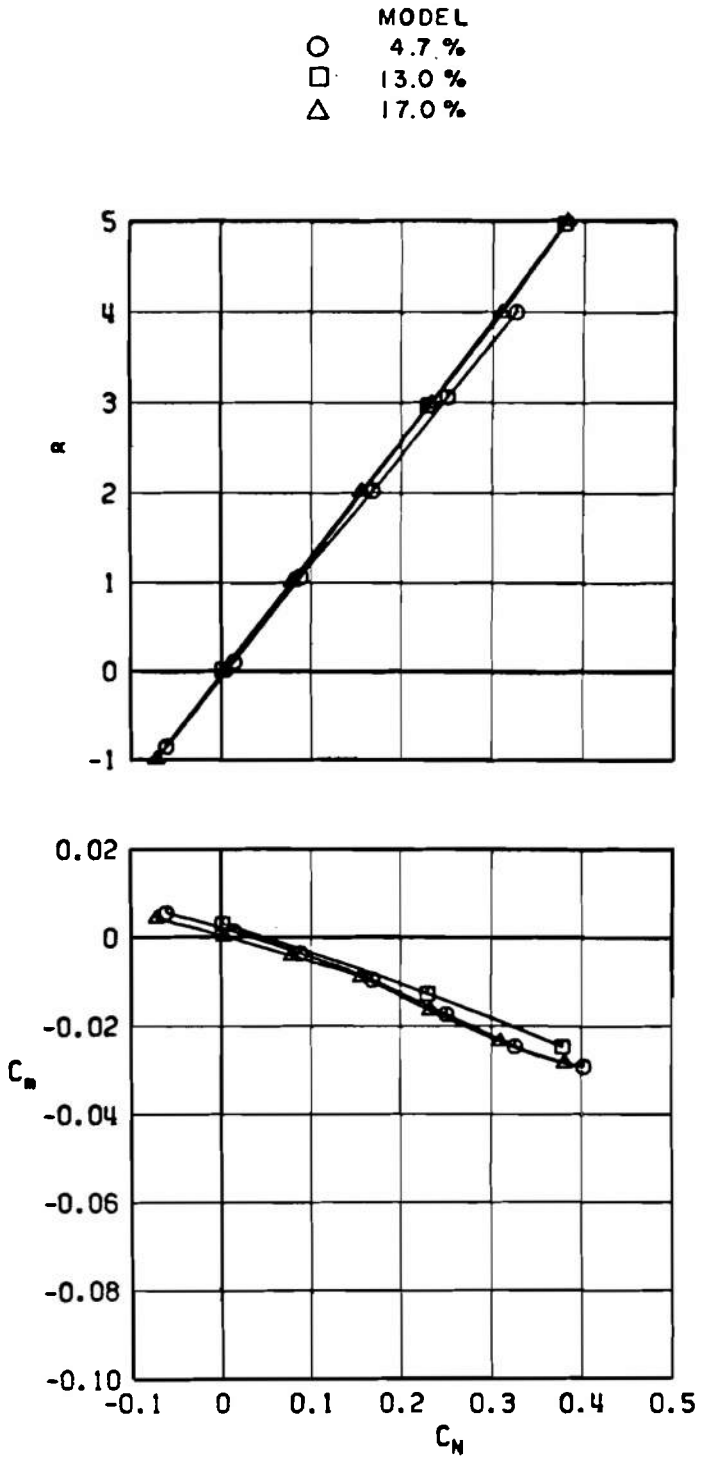

b. $M_\infty = 0.90$

Figure 42. Continued.

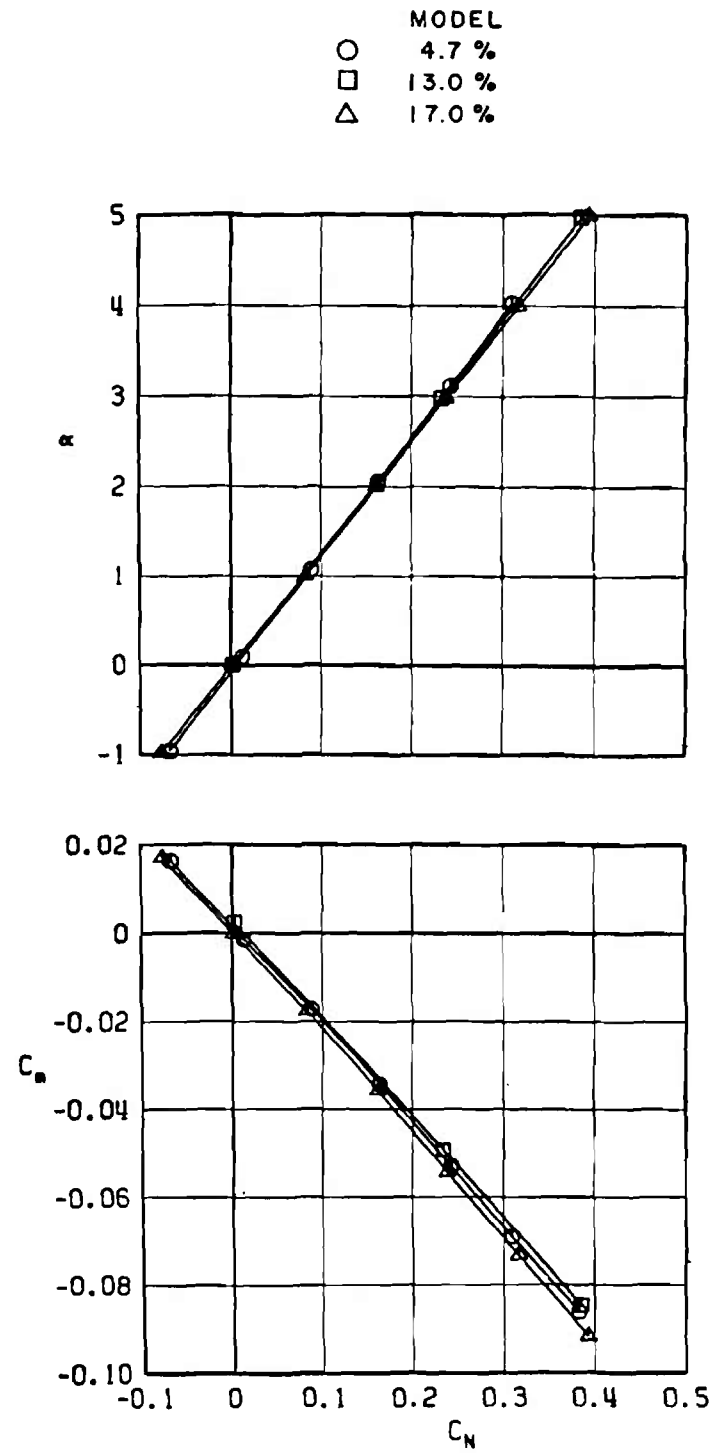

c. $M_\infty = 1.20$

Figure 42. Continued.

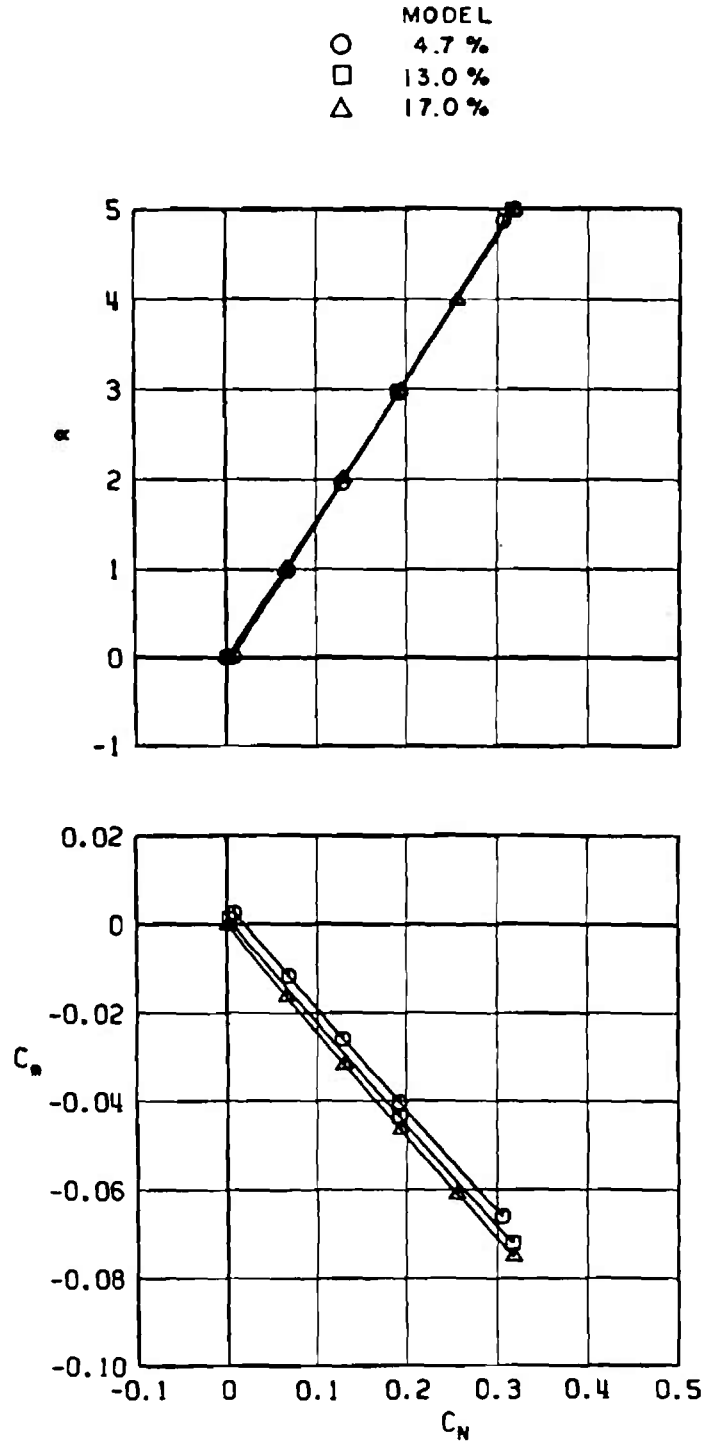

d. M_∞ = 1.40

Figure 42. Concluded.

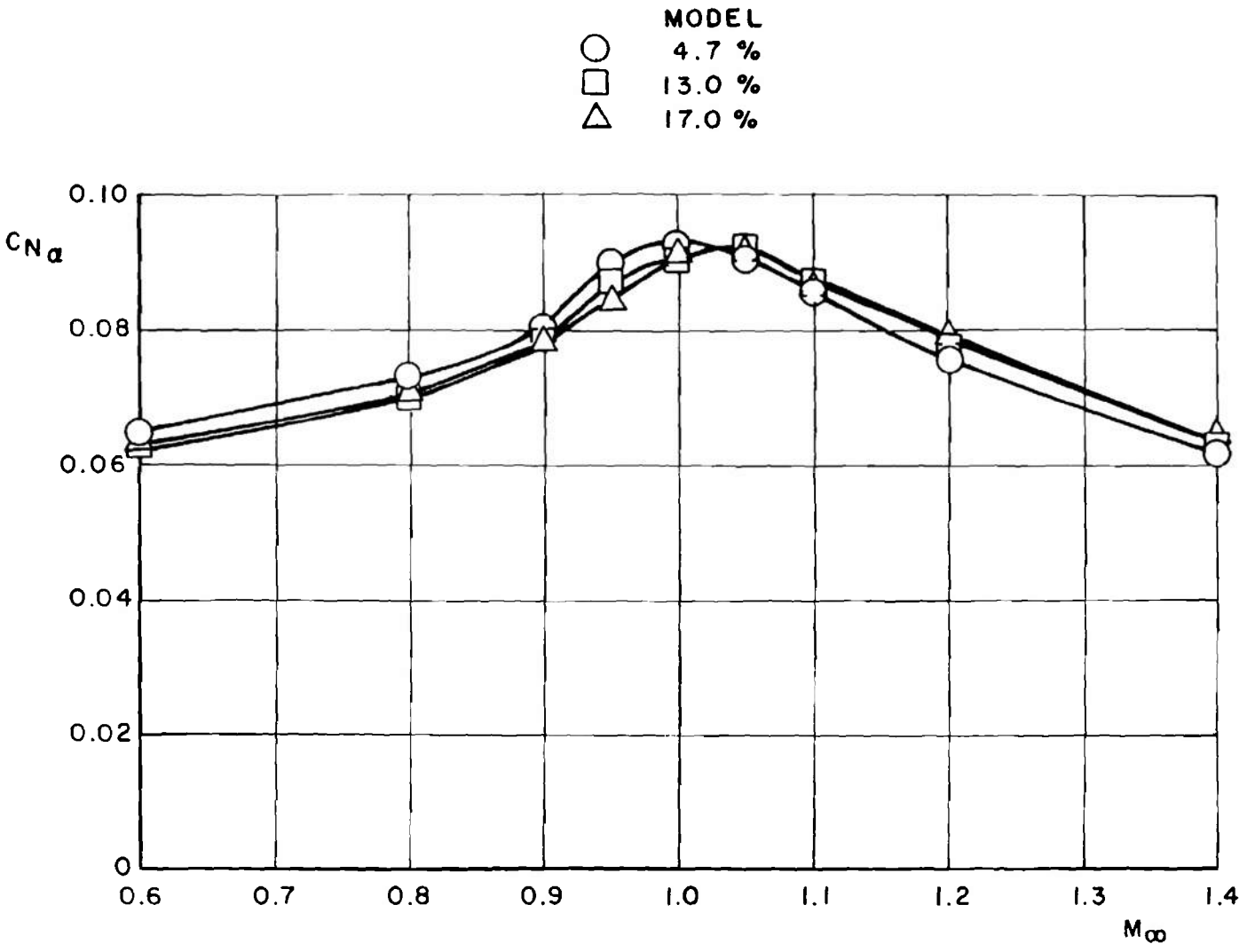

Figure 43. Normal-force coefficient slope for basic configuration.

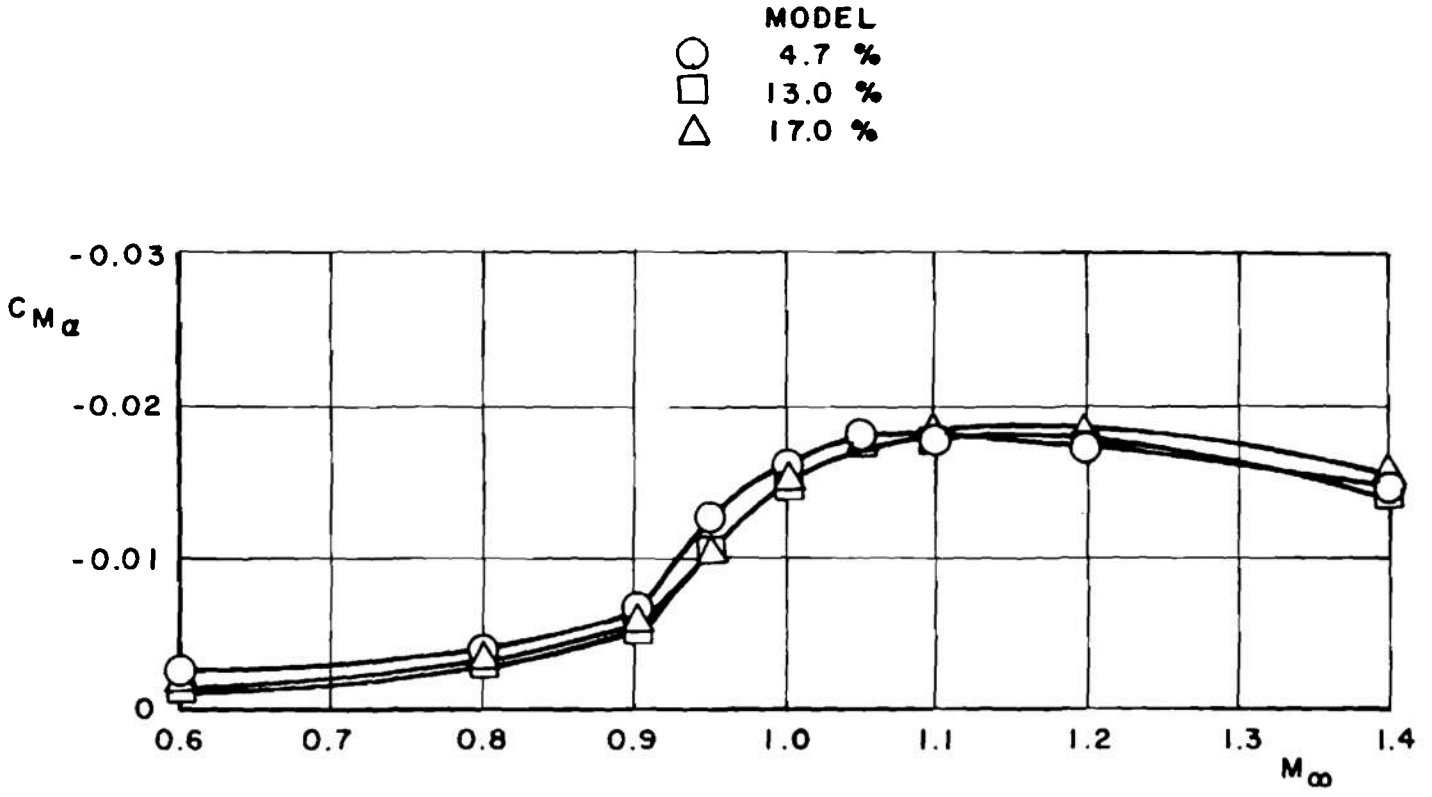

Figure 44. Pitching-moment coefficient slope for basic configuration.

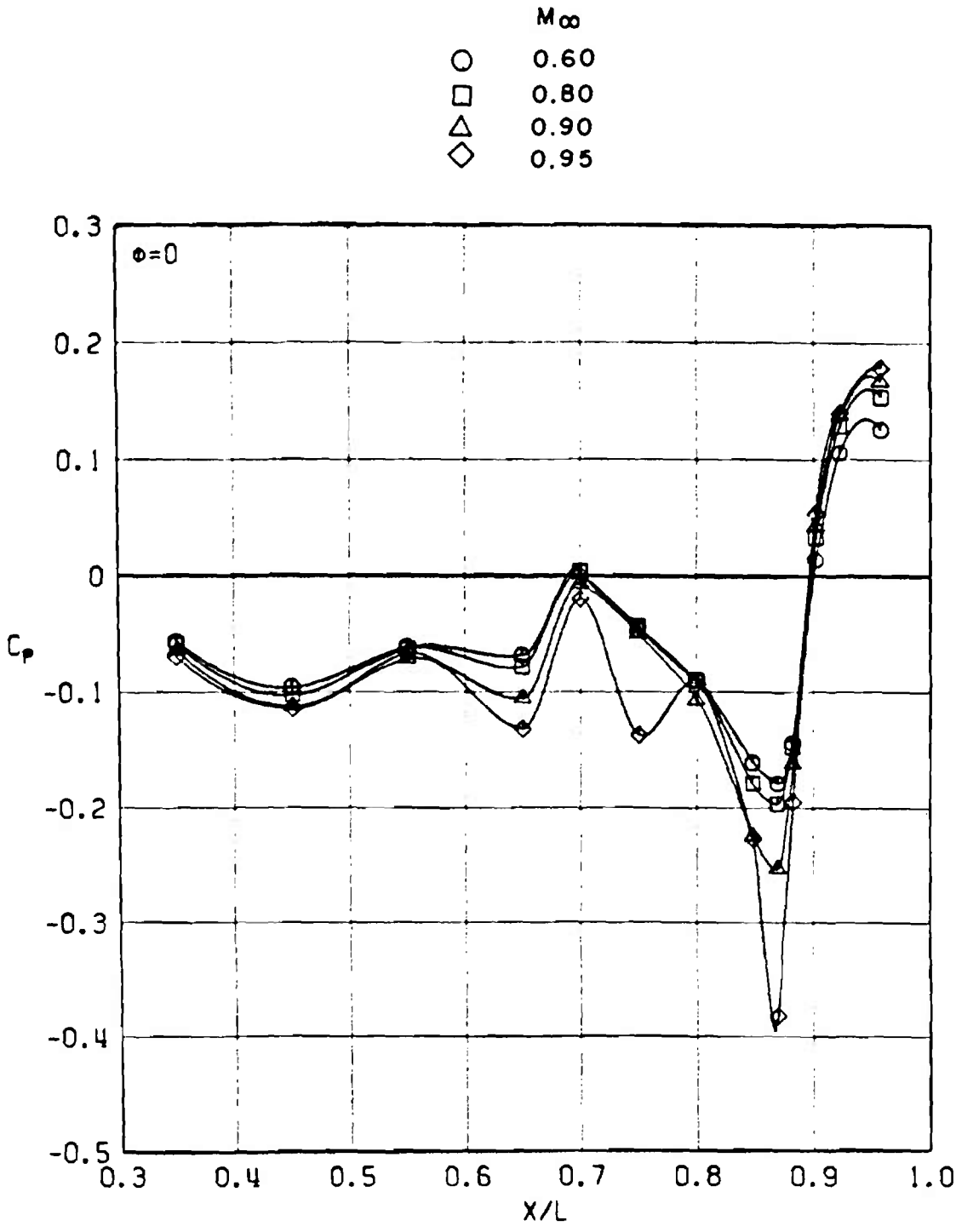

a. M_∞ = 0.60 to 0.95

Figure 45. Effect of Mach number on top centerline pressure distribution, 13-percent scale basic model, nominal characteristic Reynolds number schedule, α = 0.

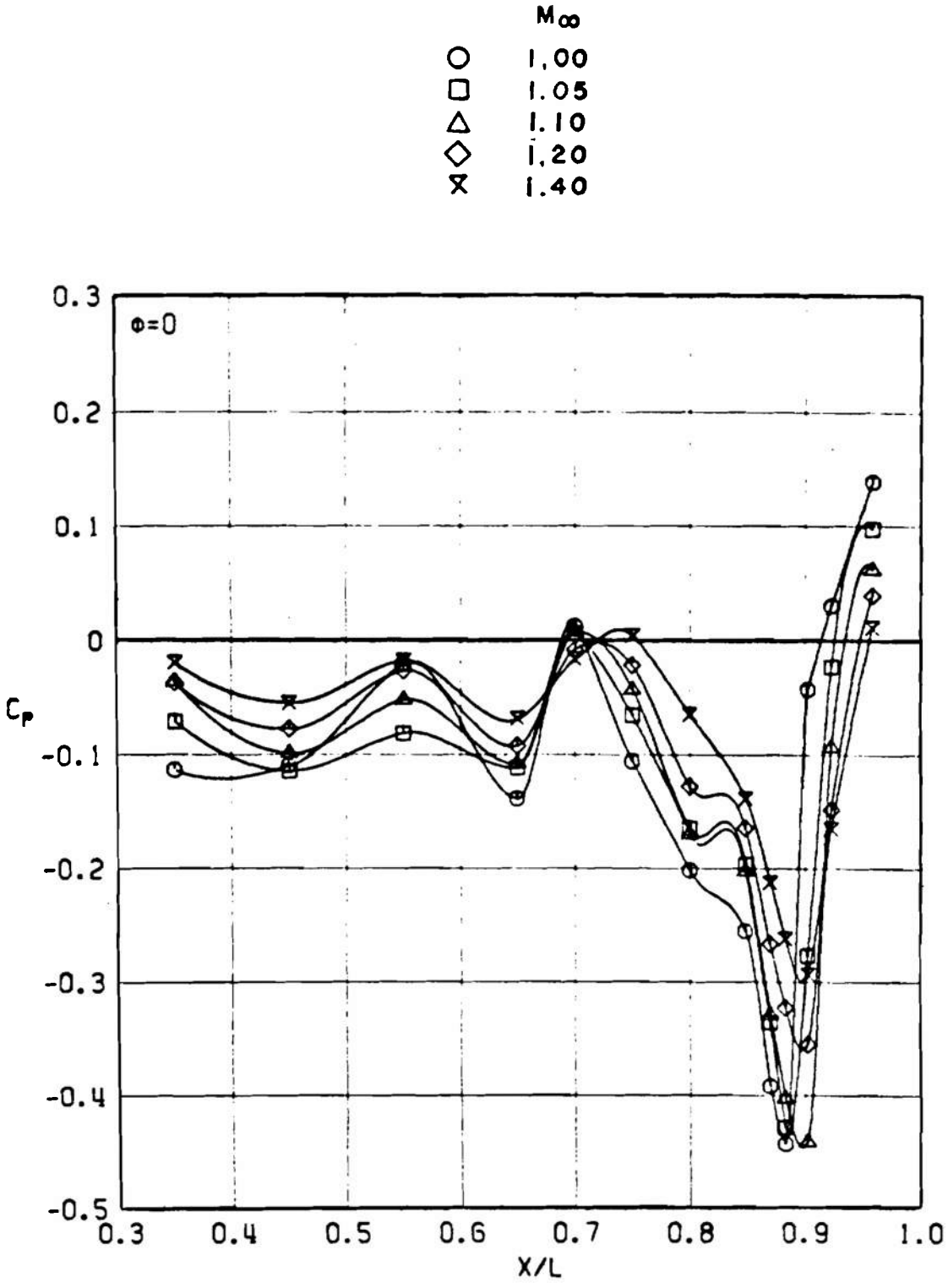

b. M_∞ = 1.00 to 1.40
Figure 45. Concluded.

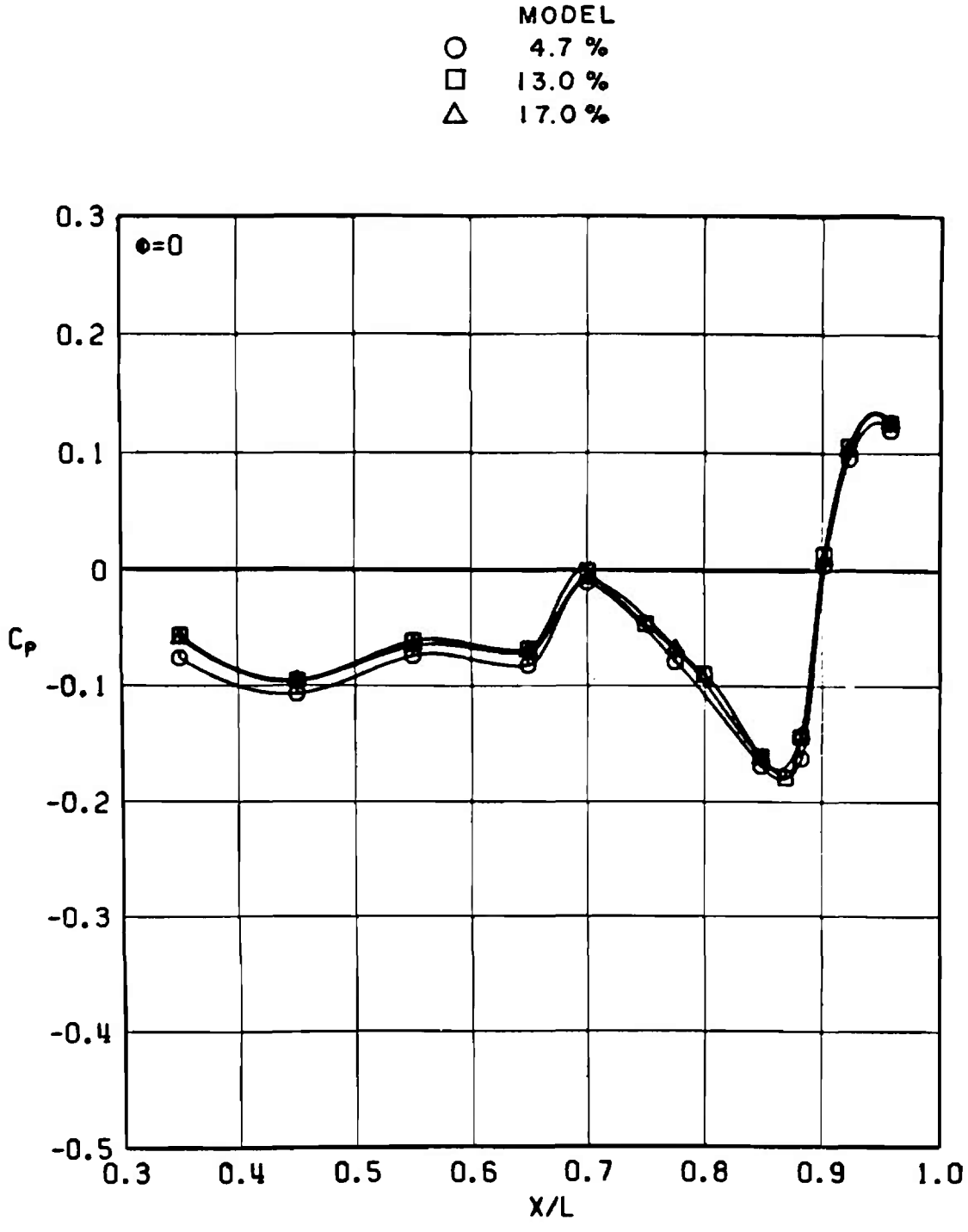

a. $M_\infty = 0.60$

Figure 46. Top centerline pressure distribution for basic configuration, nominal characteristic Reynolds number schedule, $\alpha = 0$.

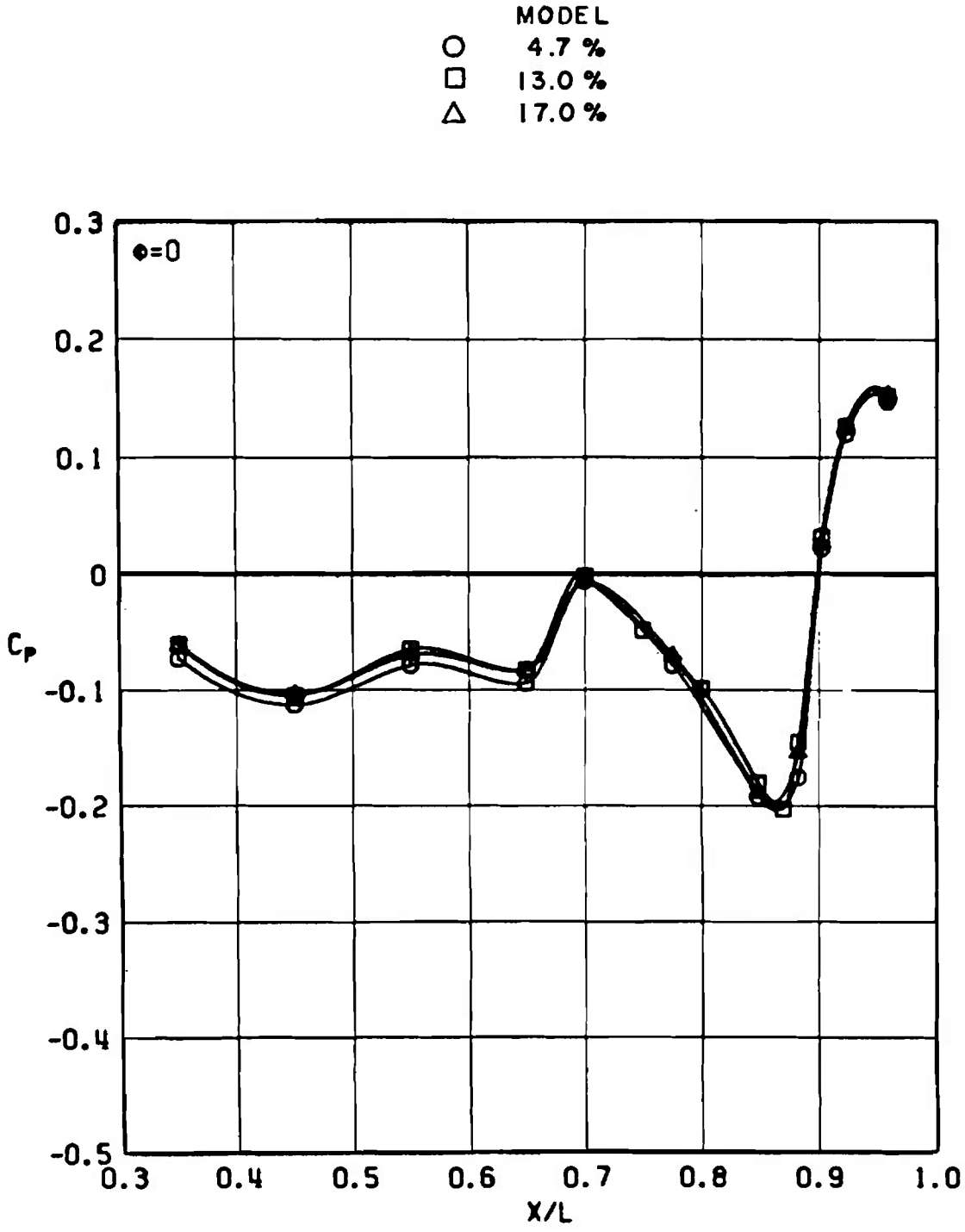

b. $M_\infty = 0.80$

Figure 46. Continued.

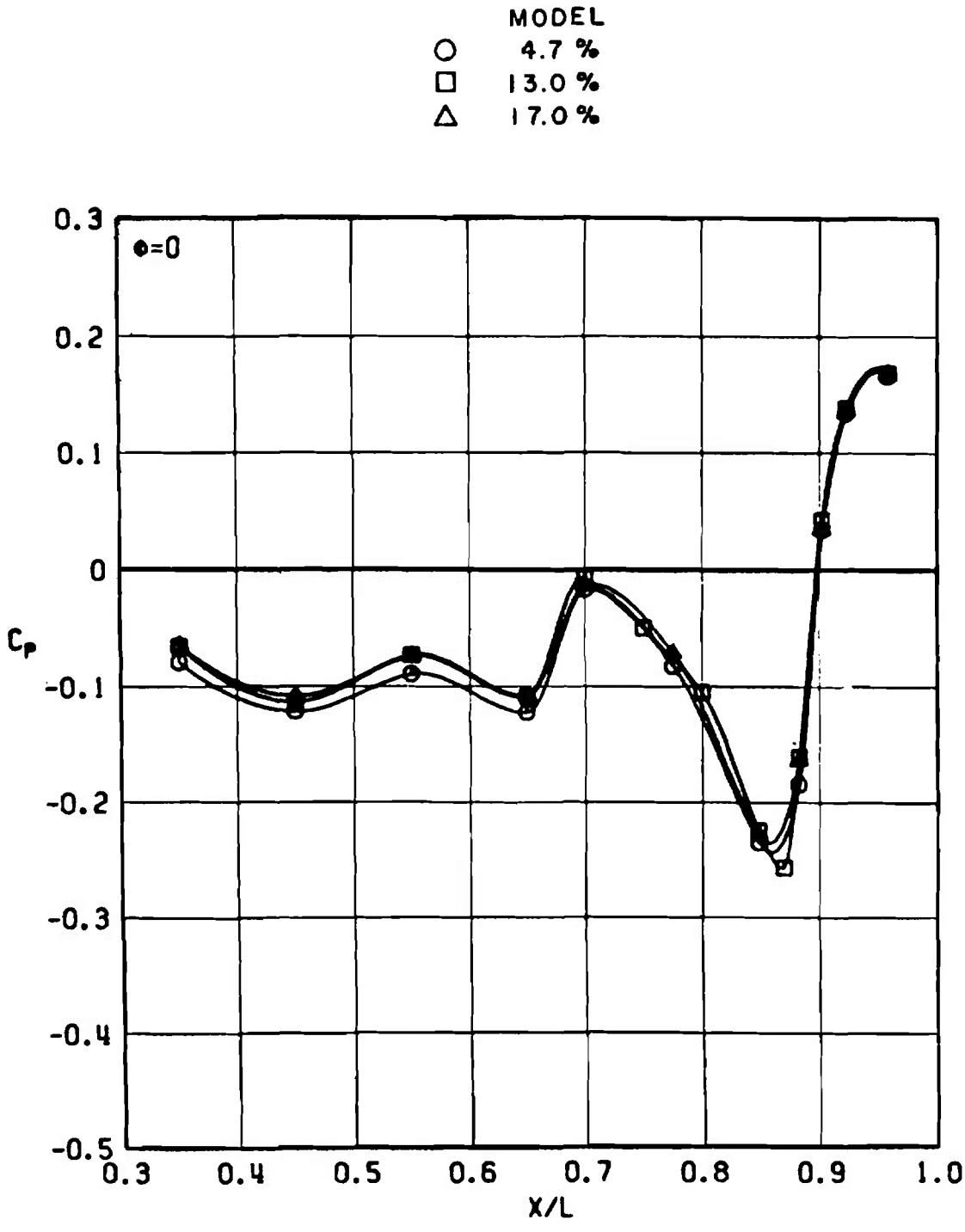

c. $M_\infty = 0.90$
Figure 46. Continued.

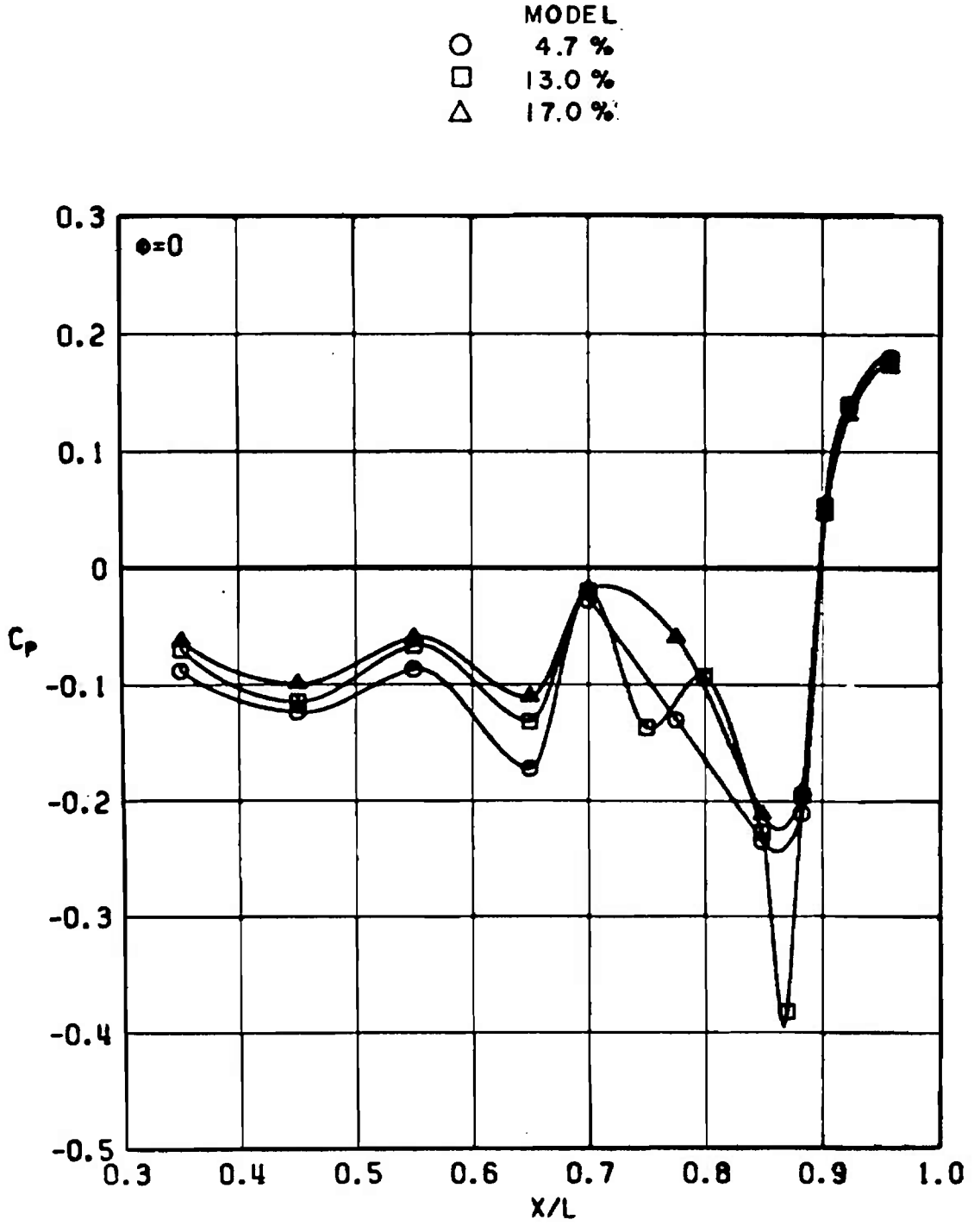

d. $M_\infty = 0.95$

Figure 46. Continued.

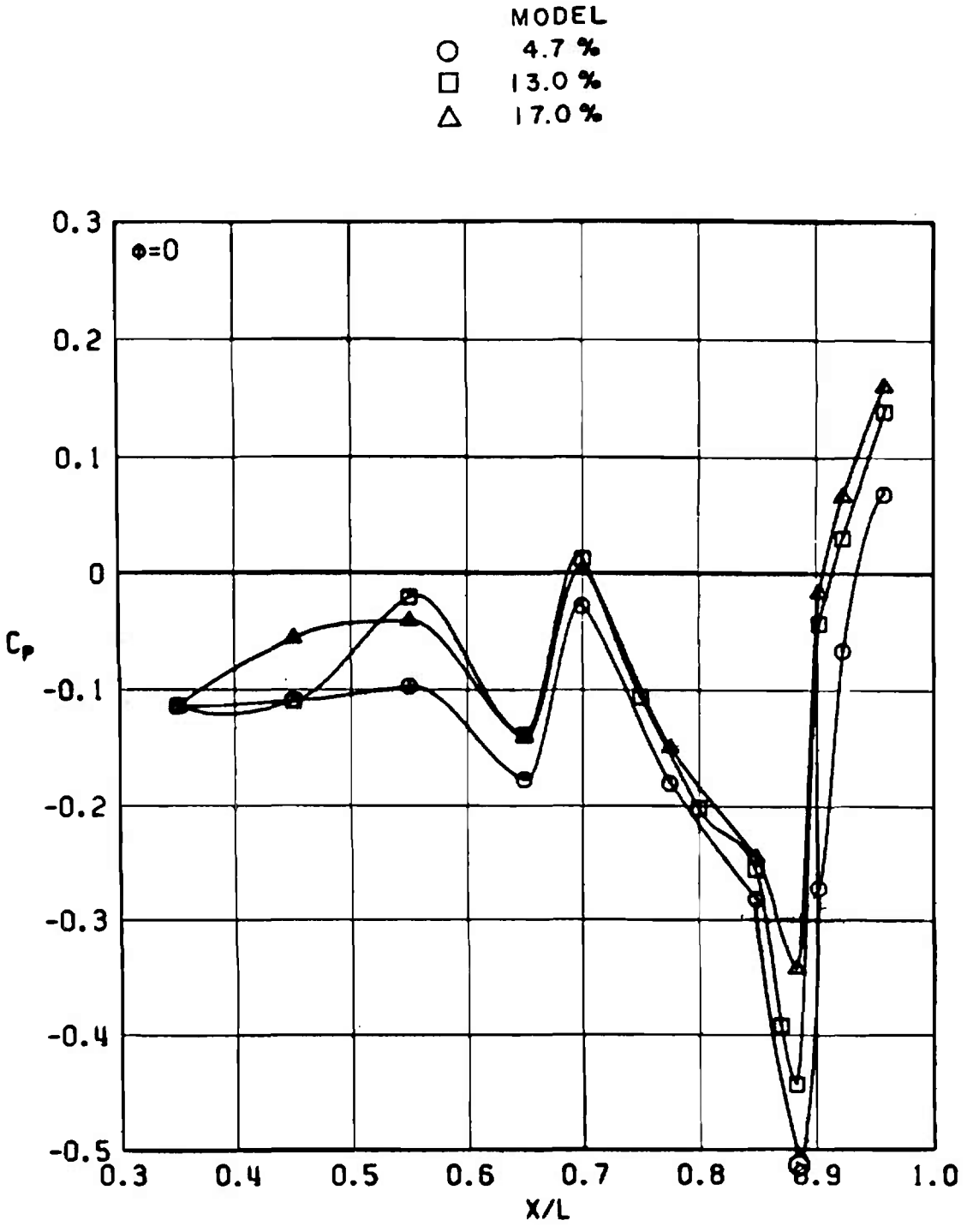

e. $M_\infty = 1.00$

Figure 46. Continued.

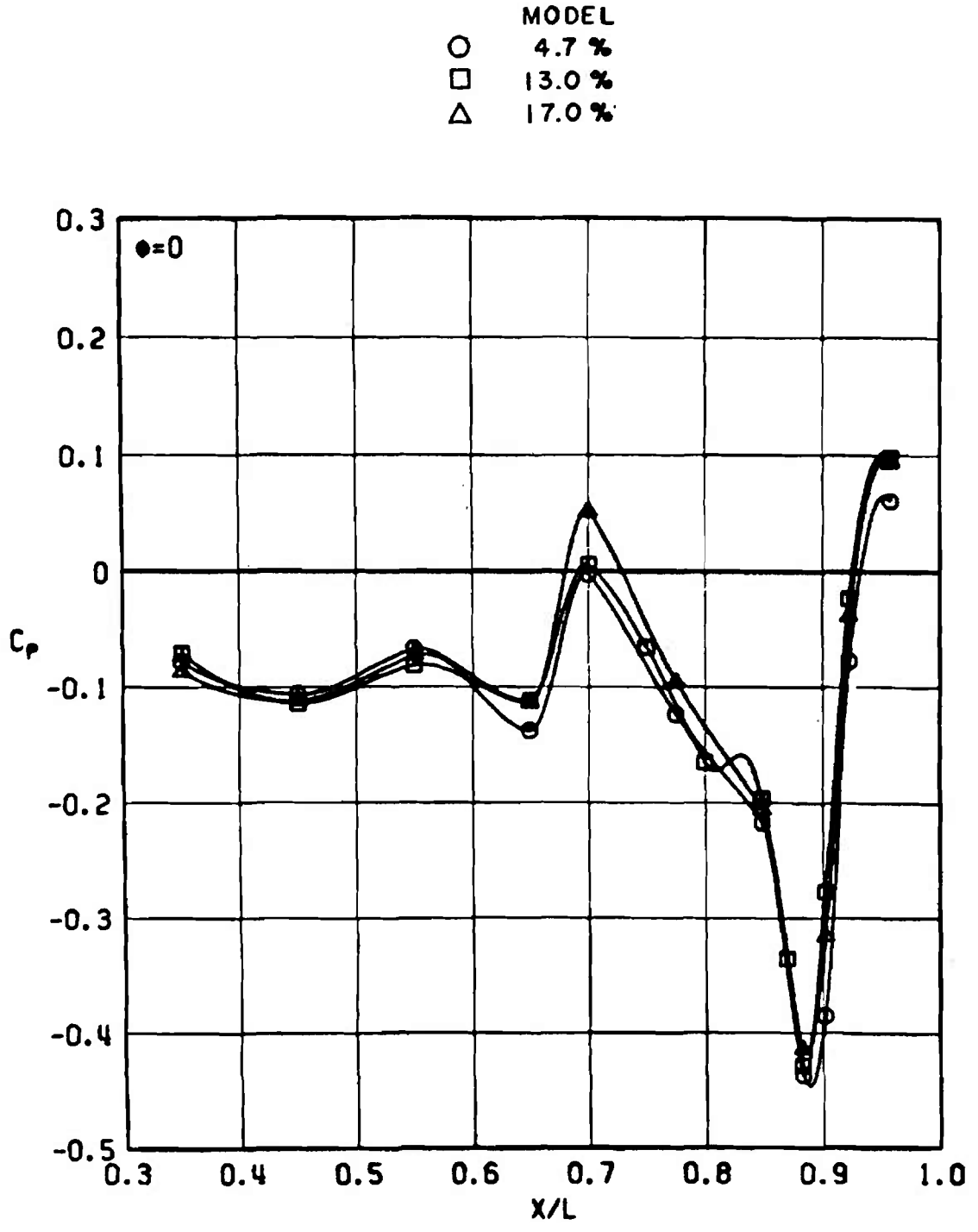

f. $M_\infty = 1.05$

Figure 46. Continued.

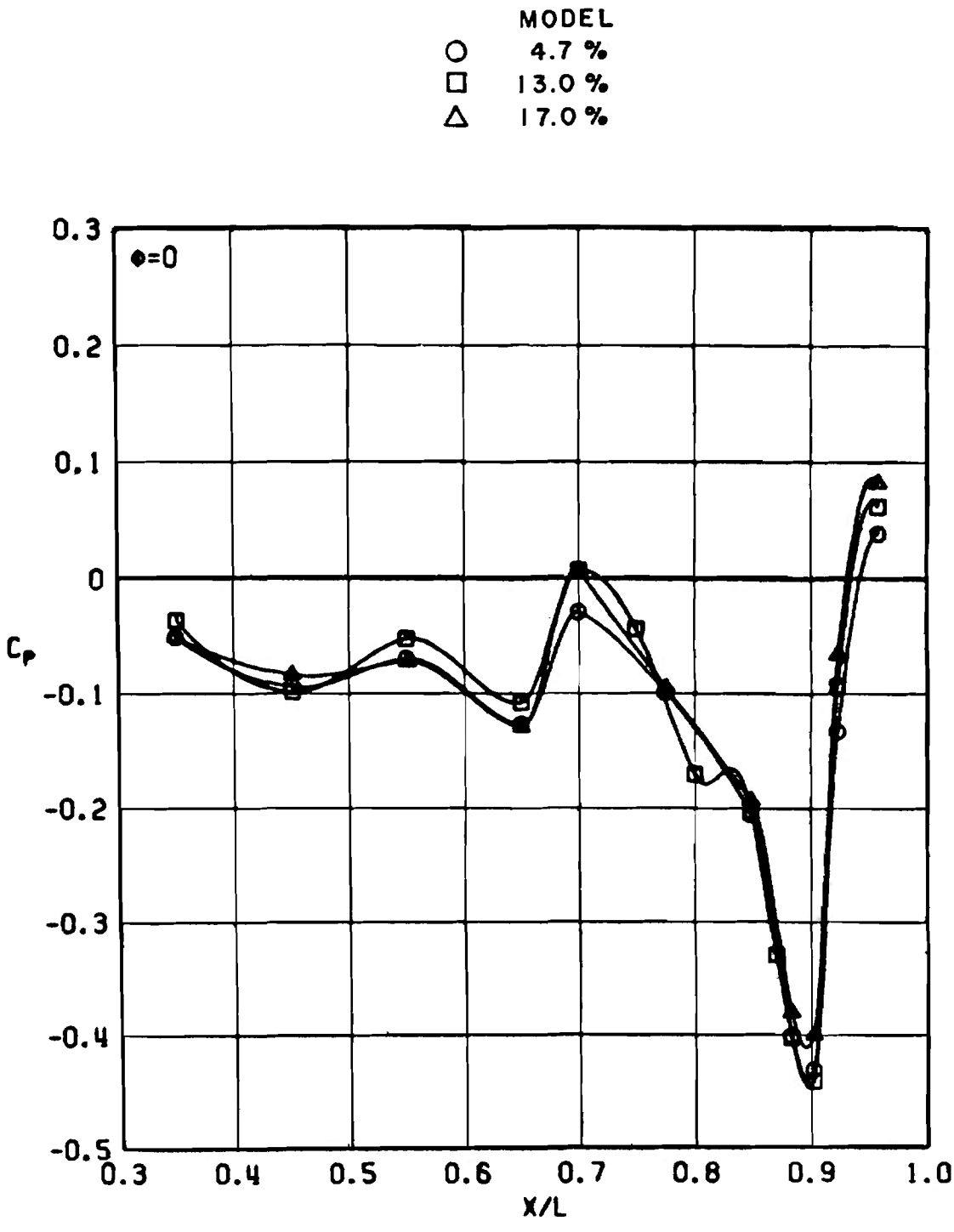

g. $M_\infty = 1.10$

Figure 46. Continued.

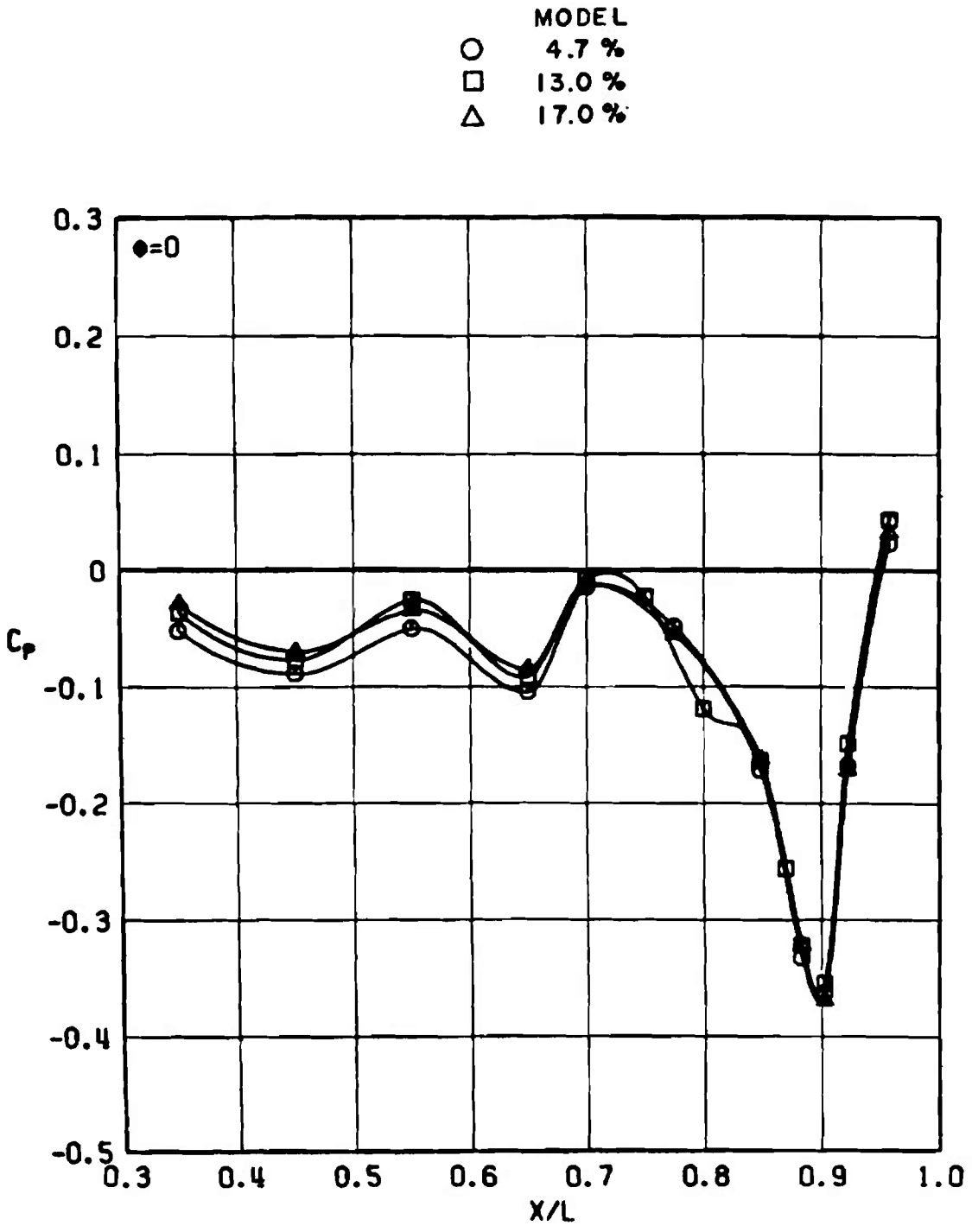

h. $M_\infty = 1.20$

Figure 46. Continued.

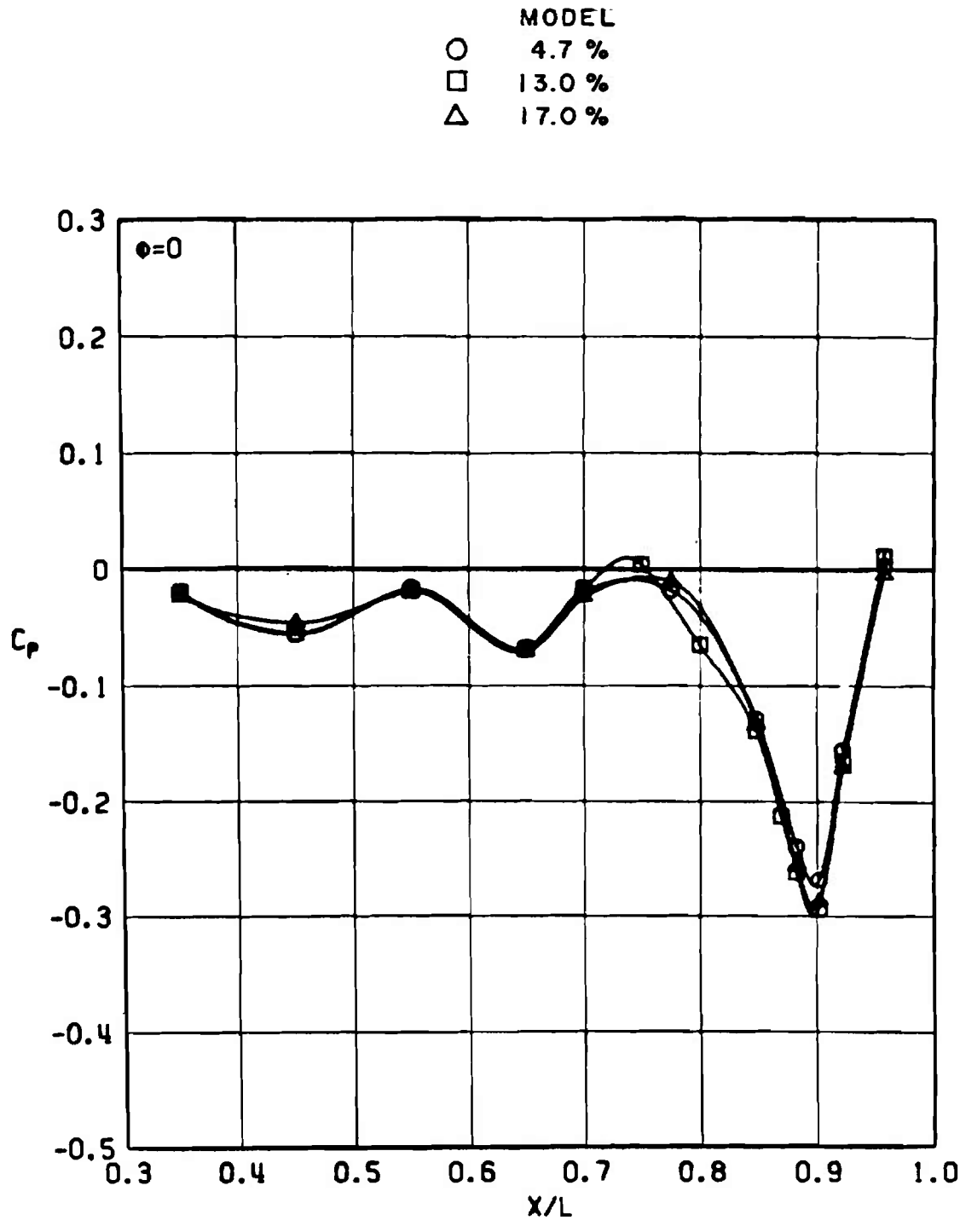

i. $M_\infty = 1.40$

Figure 46. Concluded.

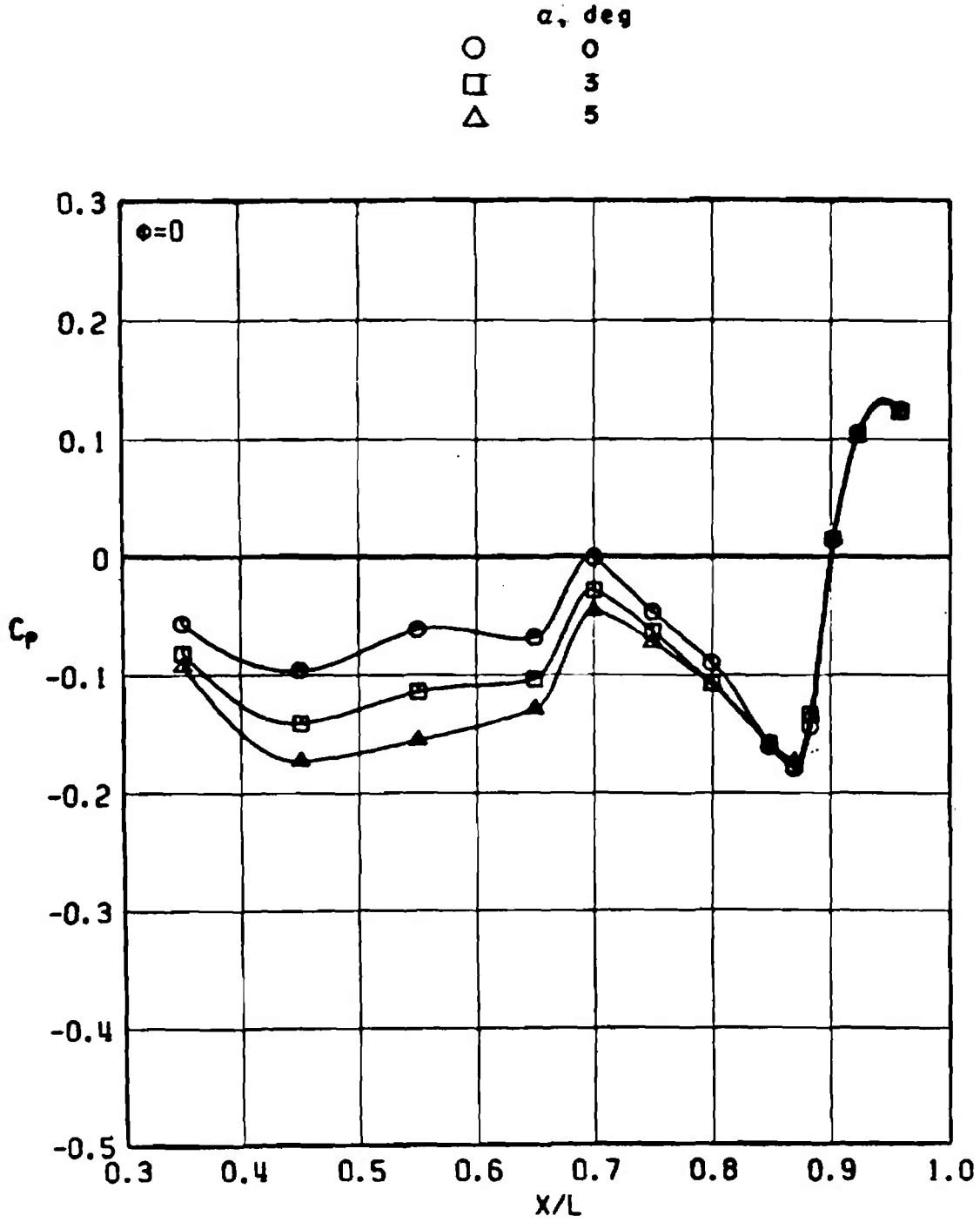

a. $M_\infty = 0.60$

Figure 47. Effect of angle of attack on the top centerline pressure distribution, 13-percent scale model, nominal characteristic Reynolds number schedule.

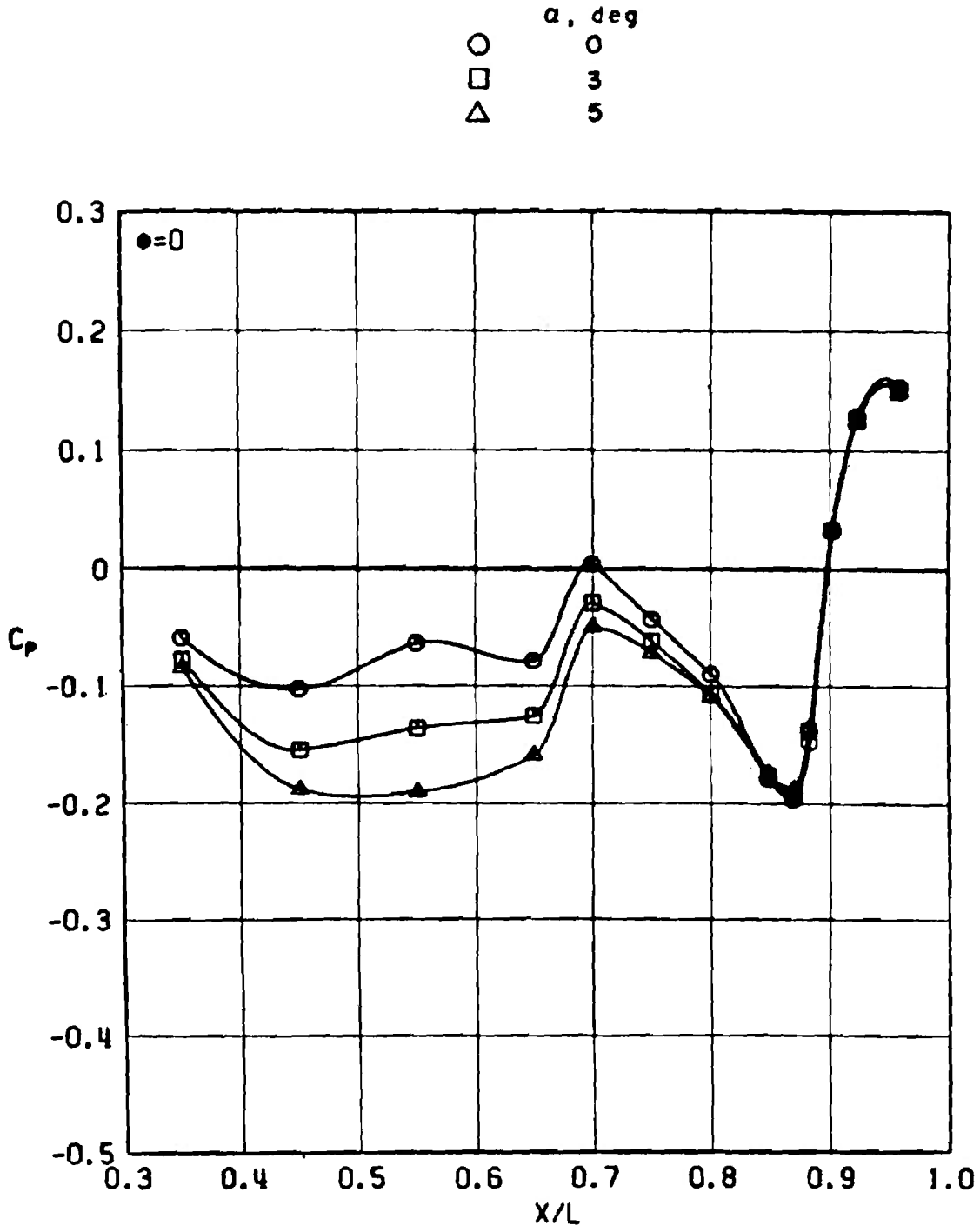

b. $M_\infty = 0.80$

Figure 47. Continued.

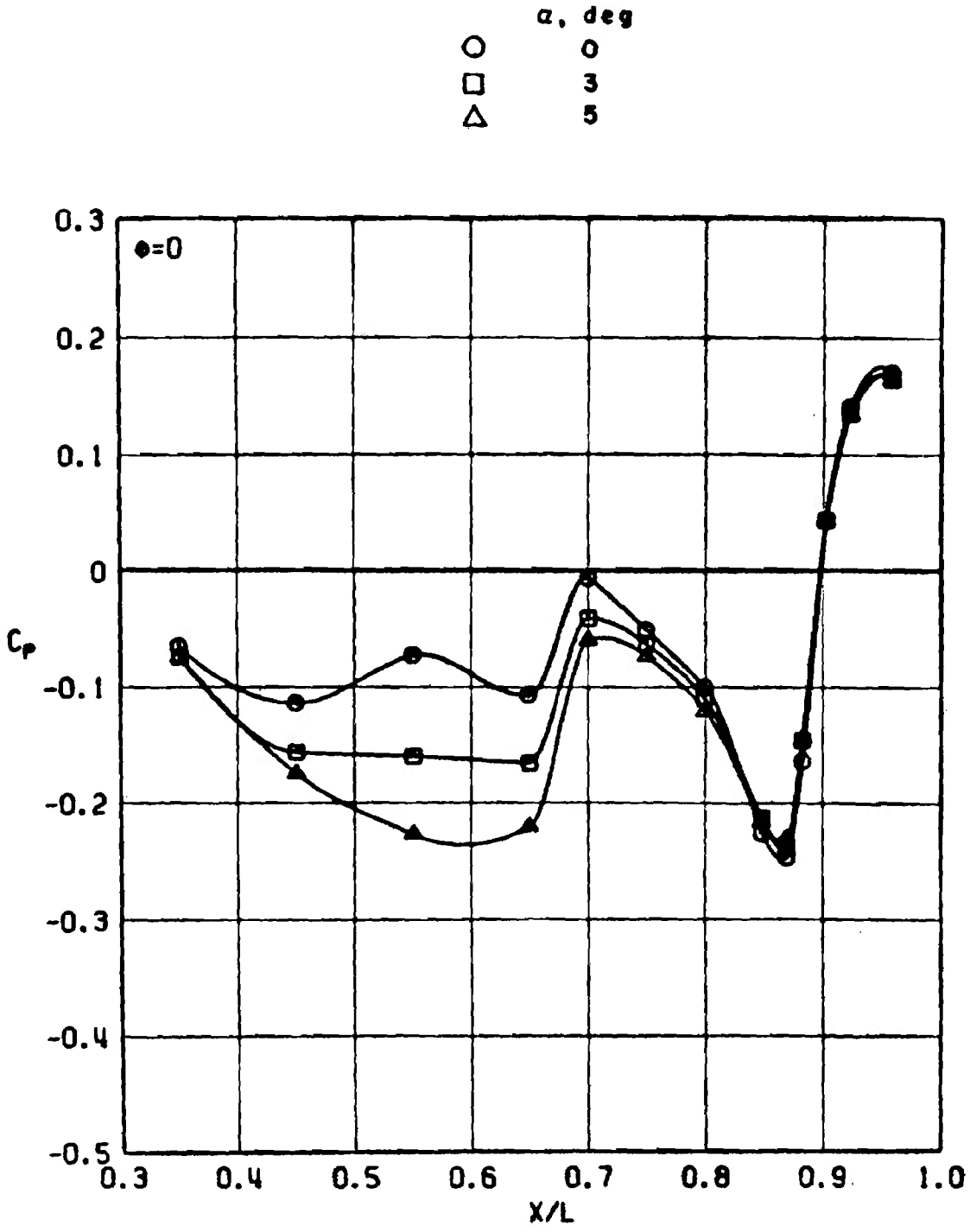

c. $M_\infty = 0.90$

Figure 47. Continued.

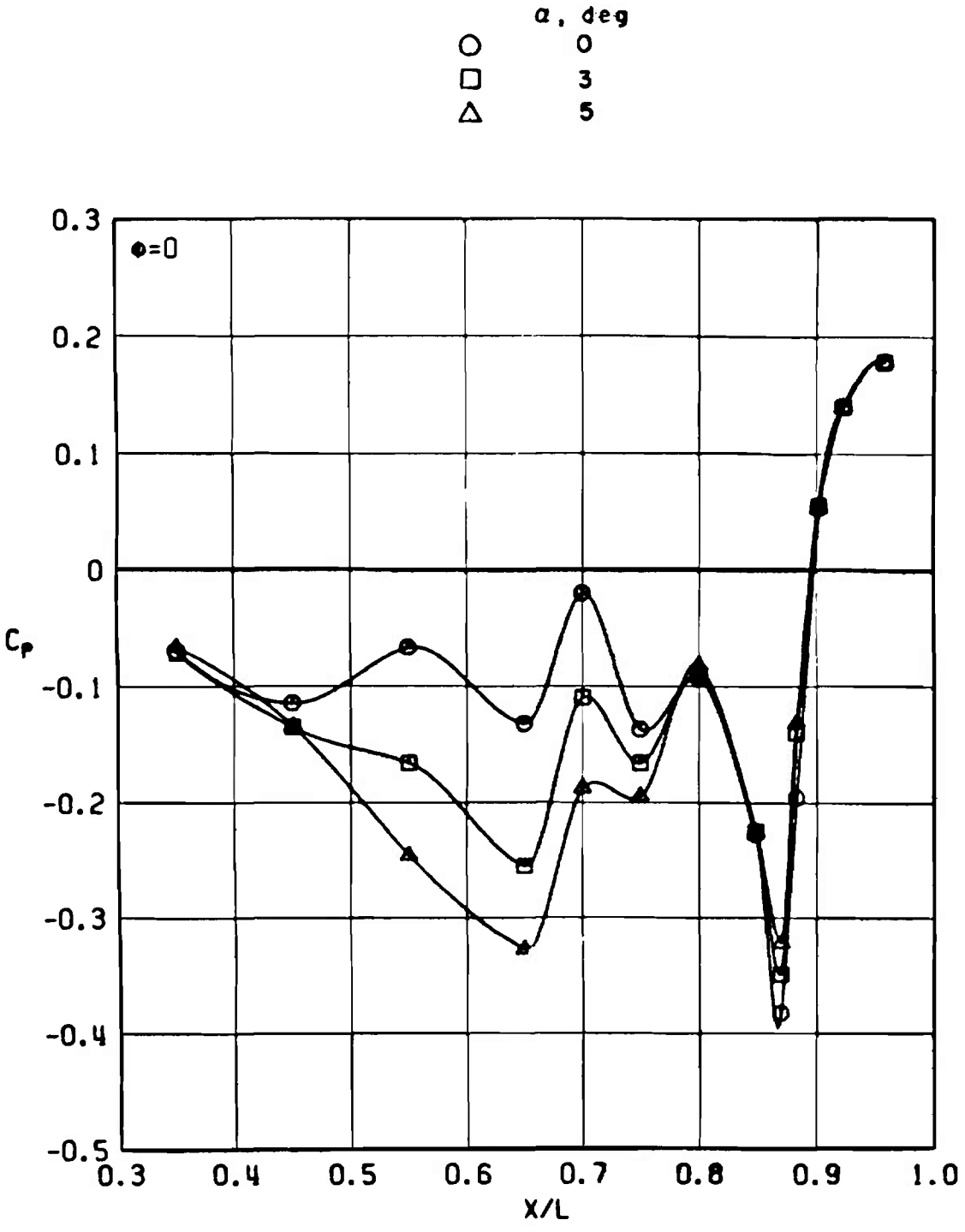

d. $M_\infty = 0.95$

Figure 47. Continued.

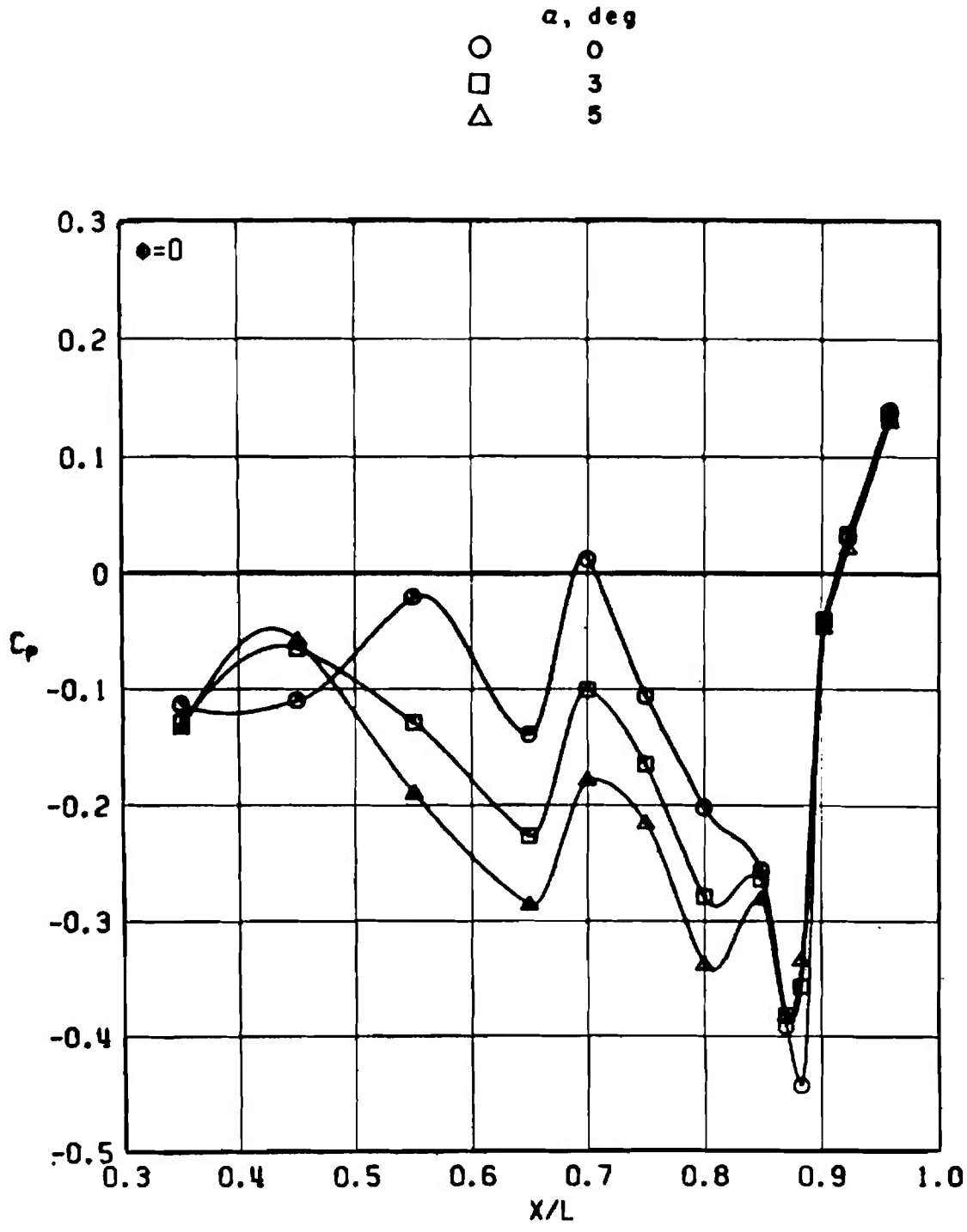

e. $M_\infty = 1.00$

Figure 47. Continued.

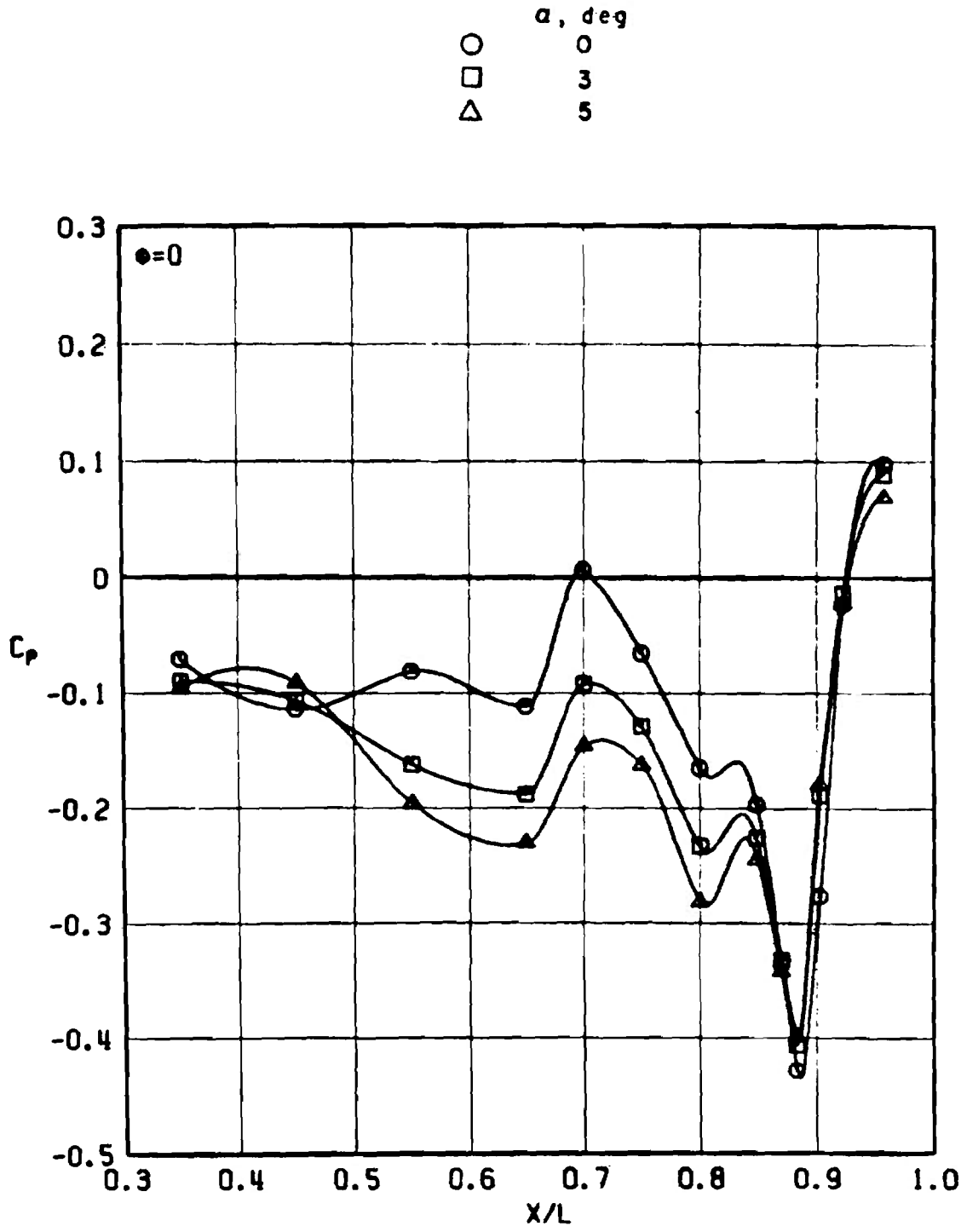

f. $M_\infty = 1.05$

Figure 47. Continued.

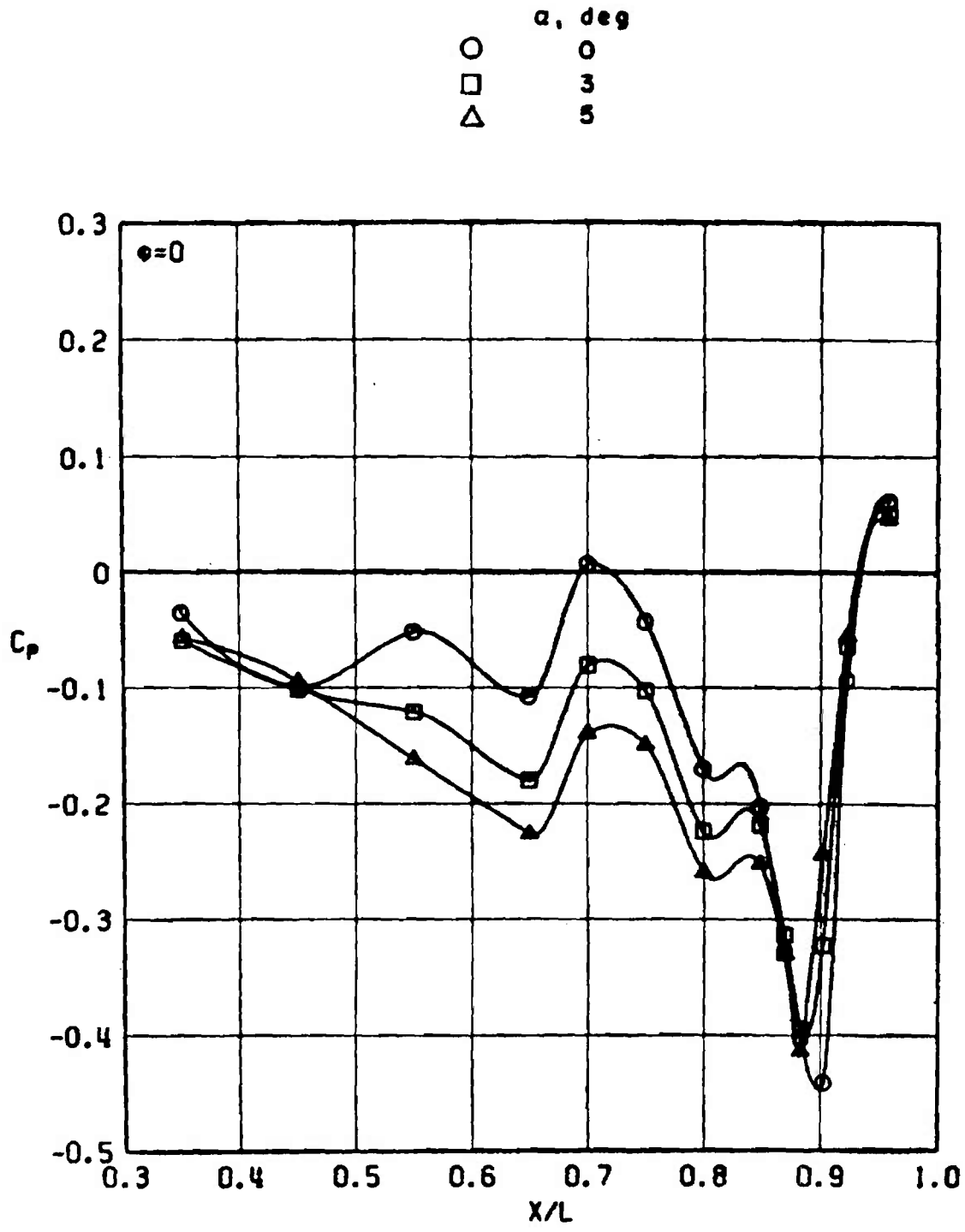

g. $M_\infty = 1.10$
Figure 47. Continued.

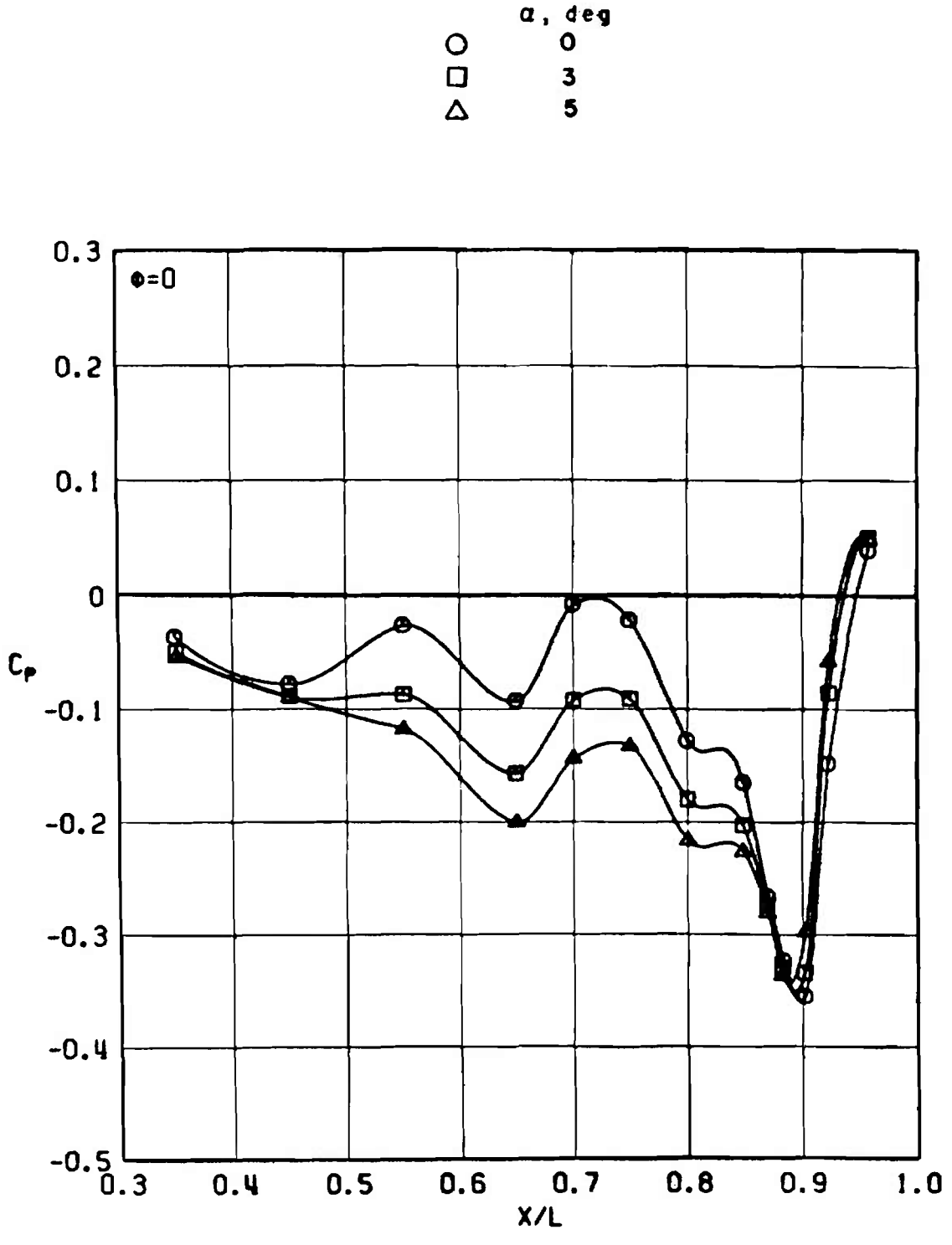

h. $M_\infty = 1.20$

Figure 47. Continued.

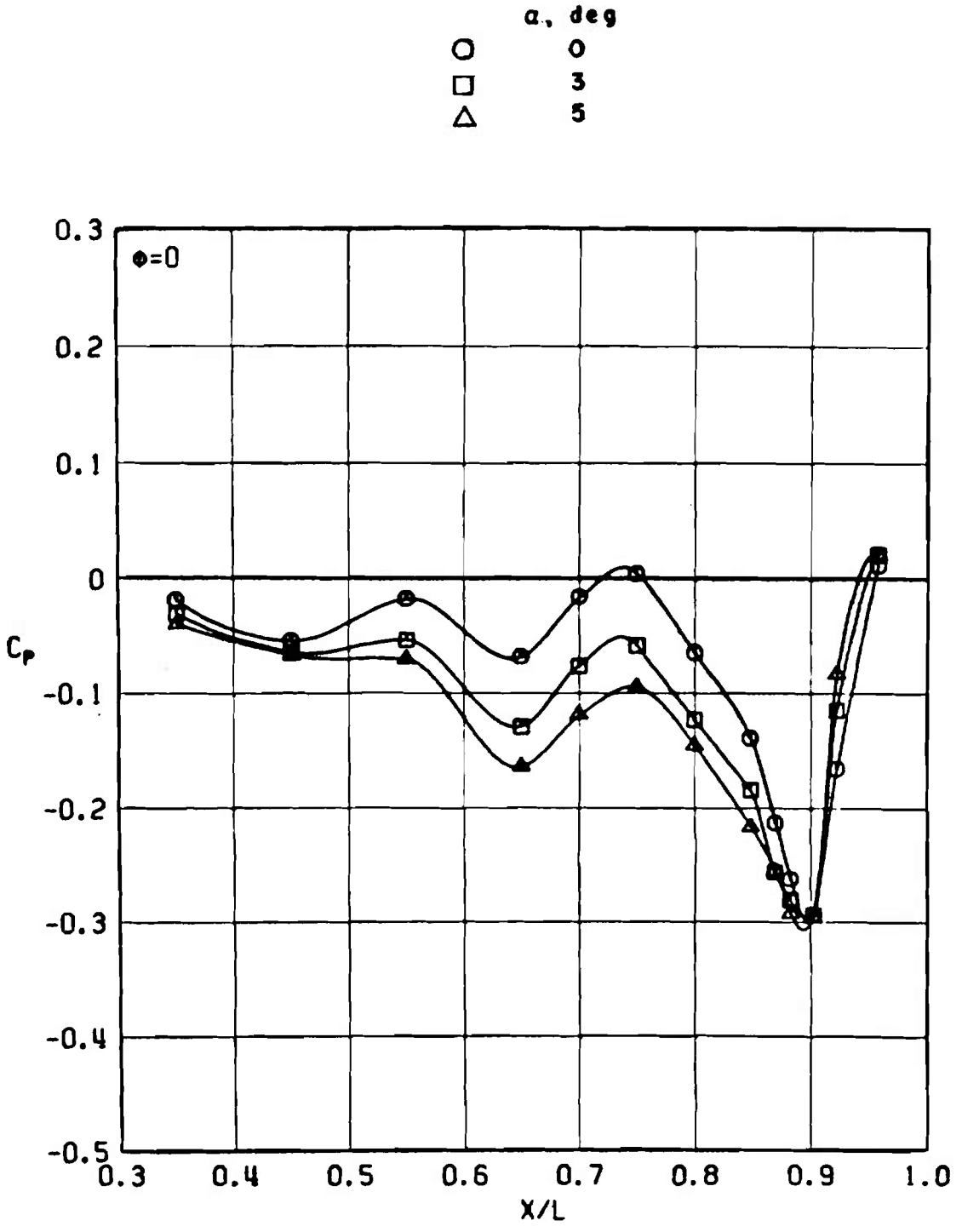

i. M_∞ = 1.40
Figure 47. Concluded.

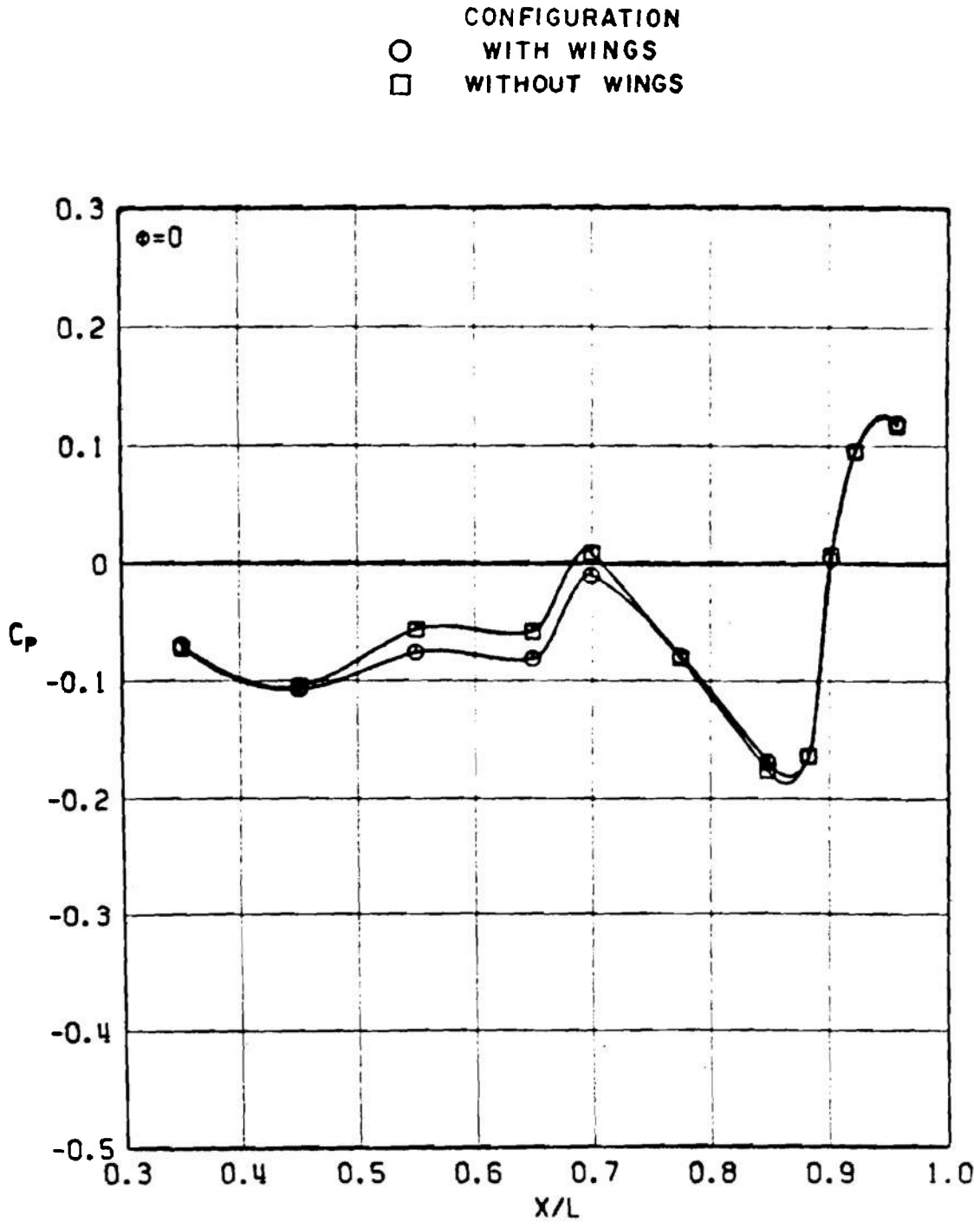

a. $M_\infty = 0.60$

Figure 48. Effect of wings on top centerline pressure distribution, 4.7-percent scale model, nominal characteristic Reynolds number schedule, $\alpha = 0$.

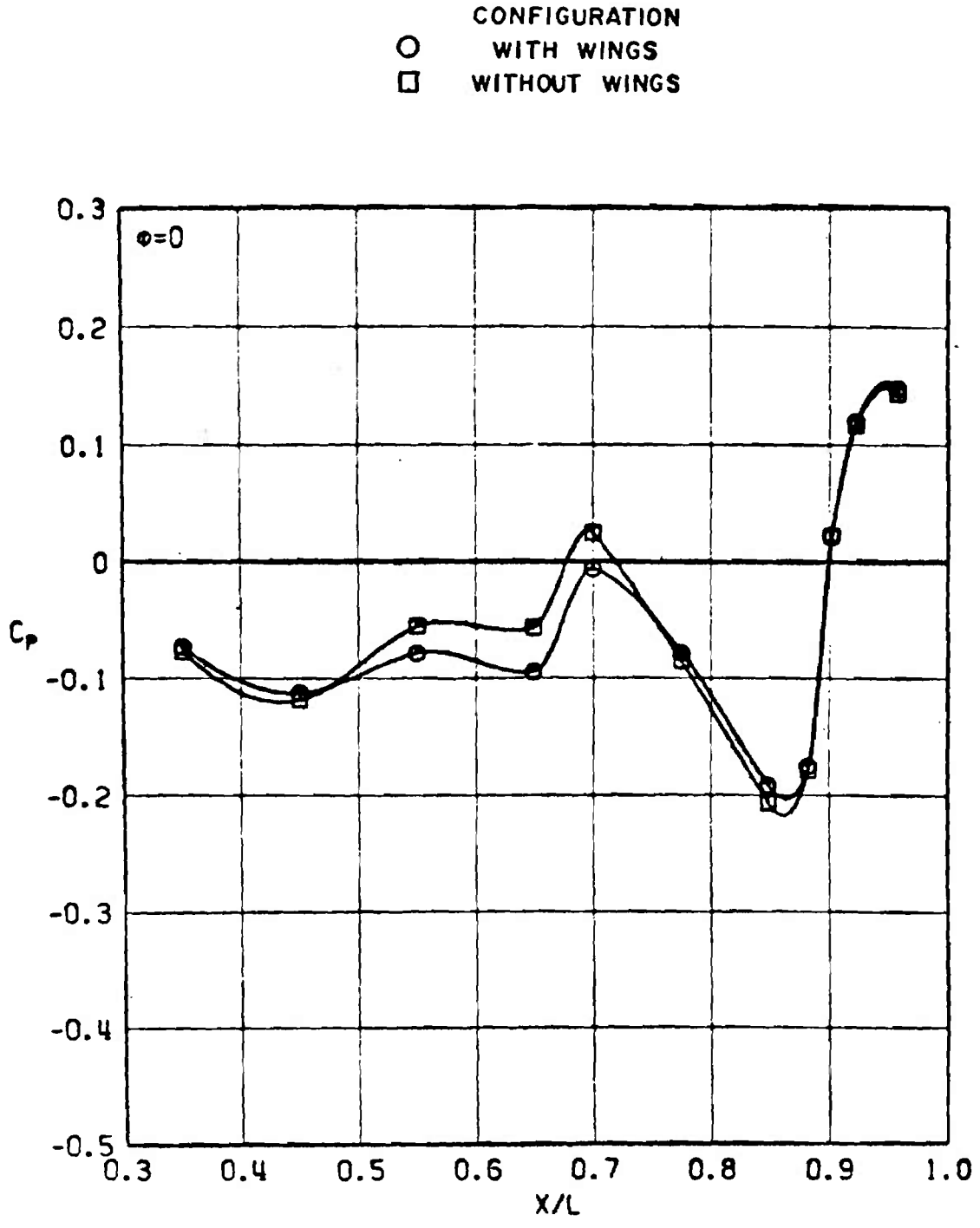

b. $M_\infty = 0.80$

Figure 48. Continued.

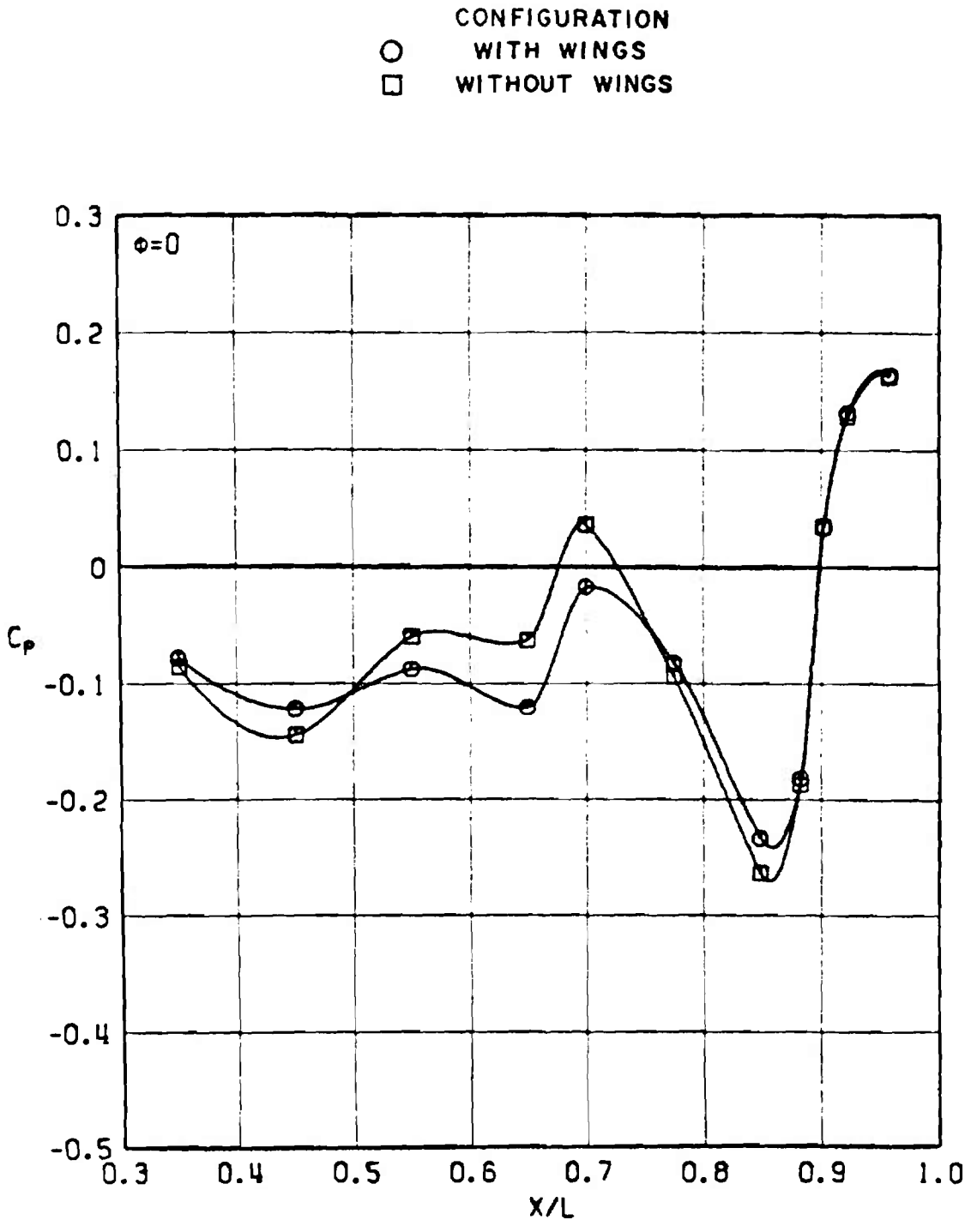

c. $M_\infty = 0.90$

Figure 48. Continued.

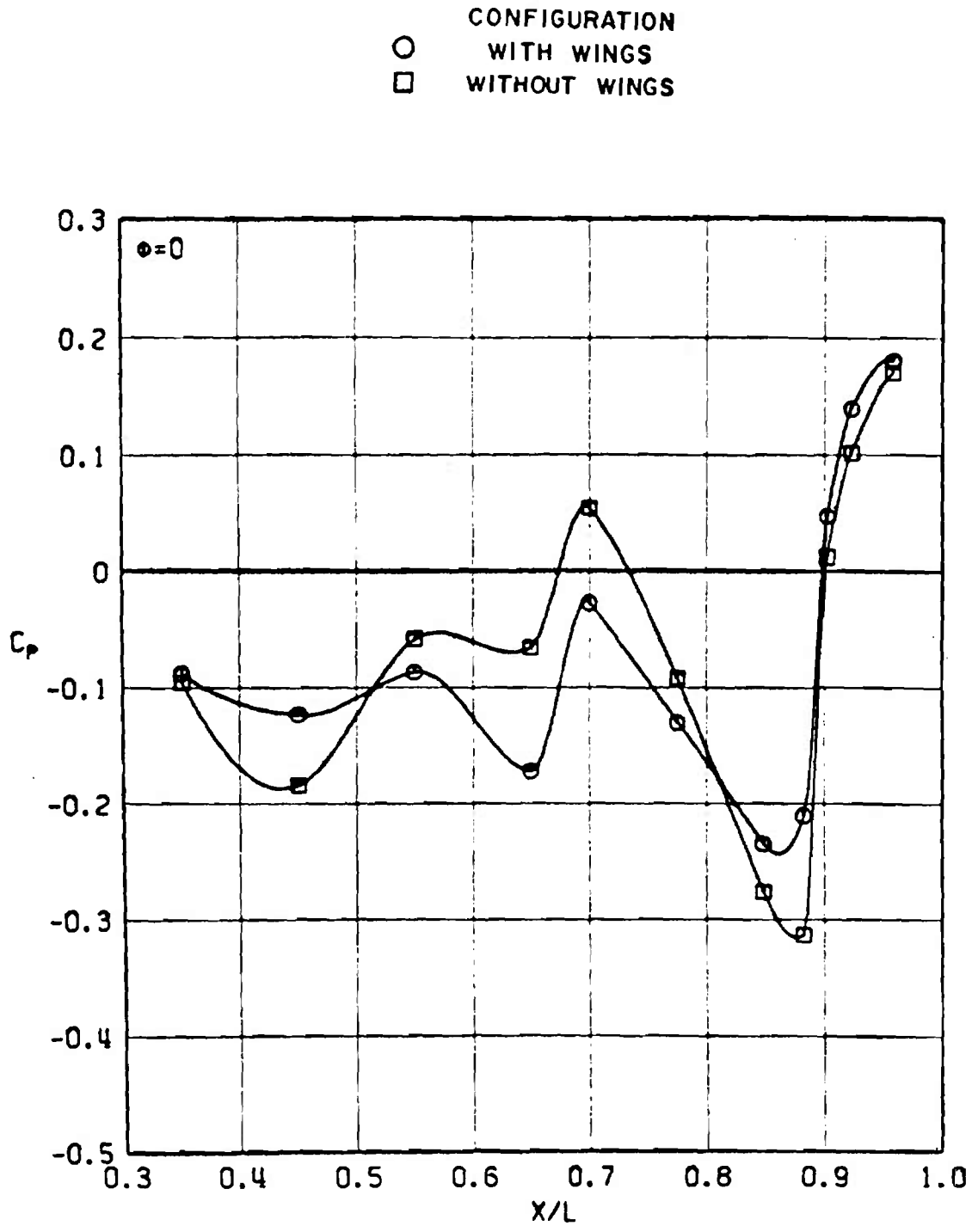

d. $M_\infty = 0.95$

Figure 48. Continued.

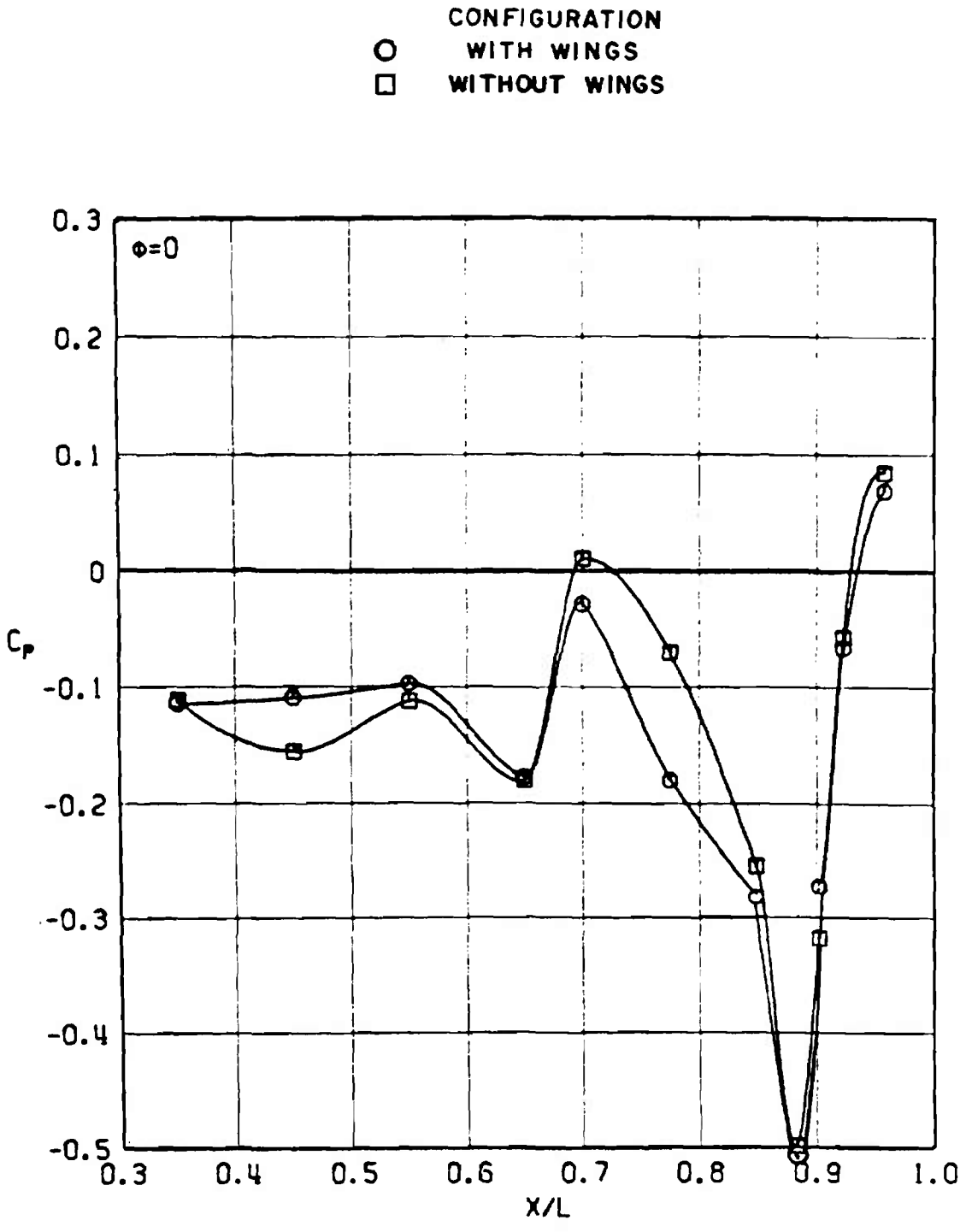

e. $M_\infty = 1.00$

Figure 48. Continued.

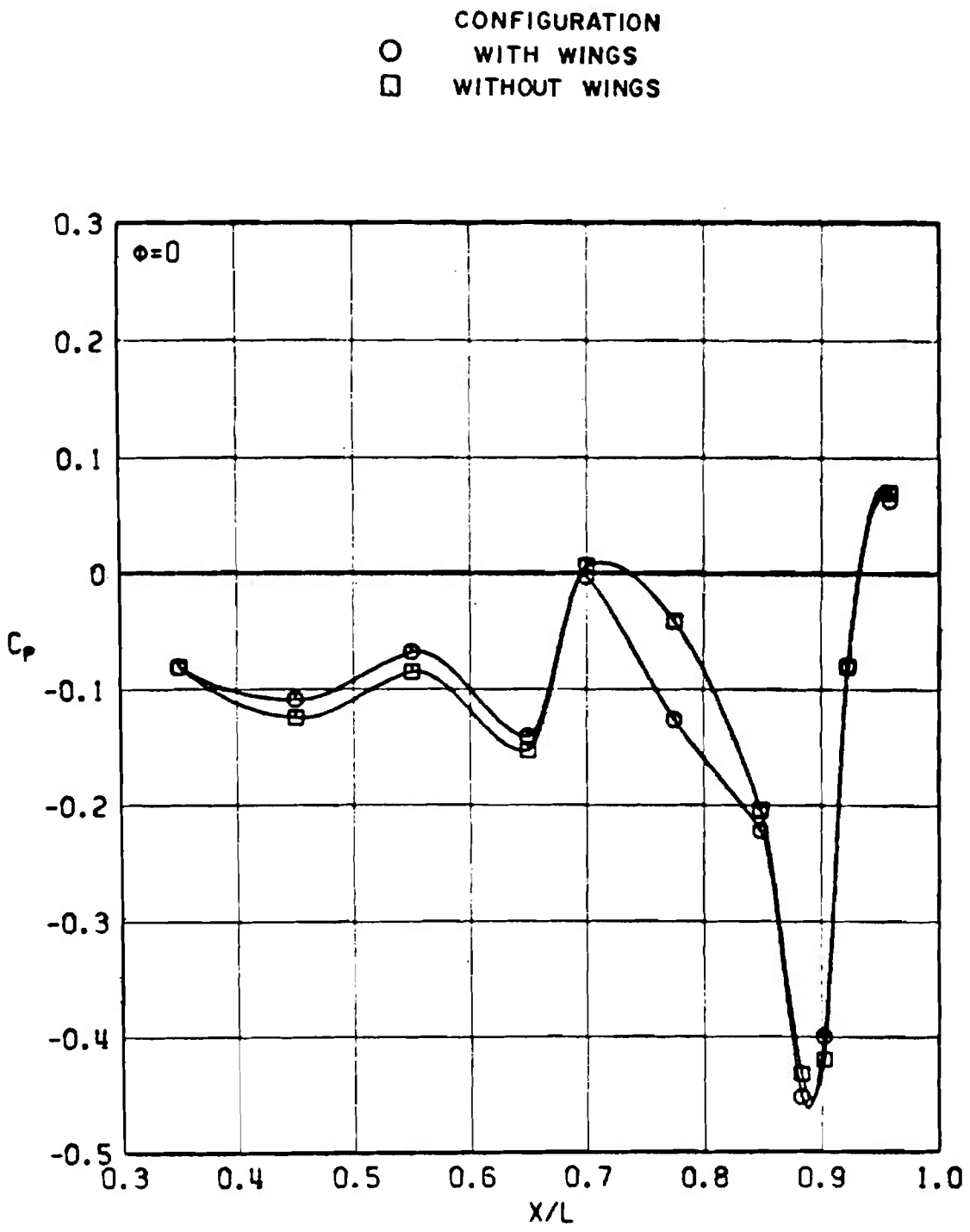

f. $M_\infty = 1.05$

Figure 48. Continued.

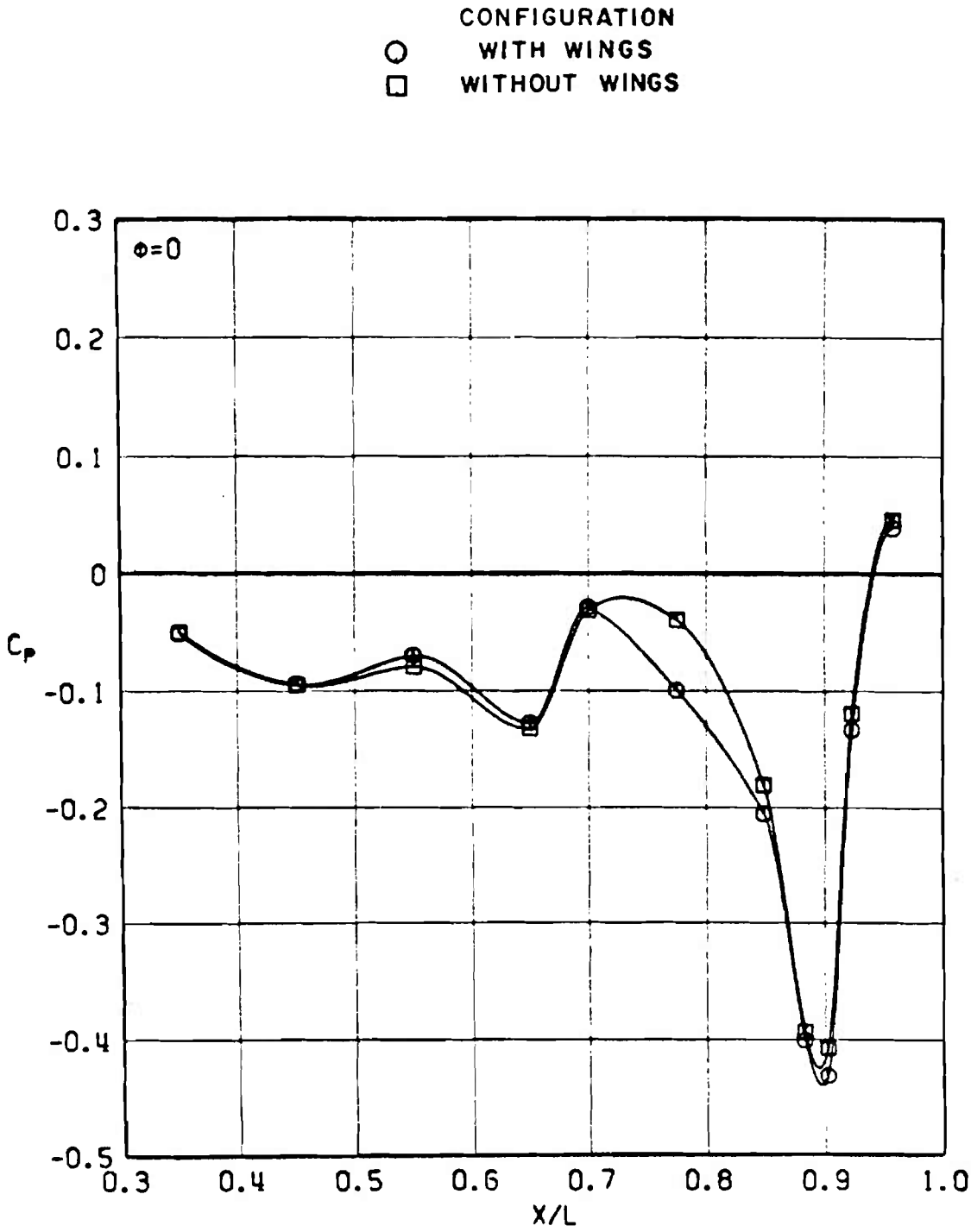

g. $M_\infty = 1.10$

Figure 48. Continued.

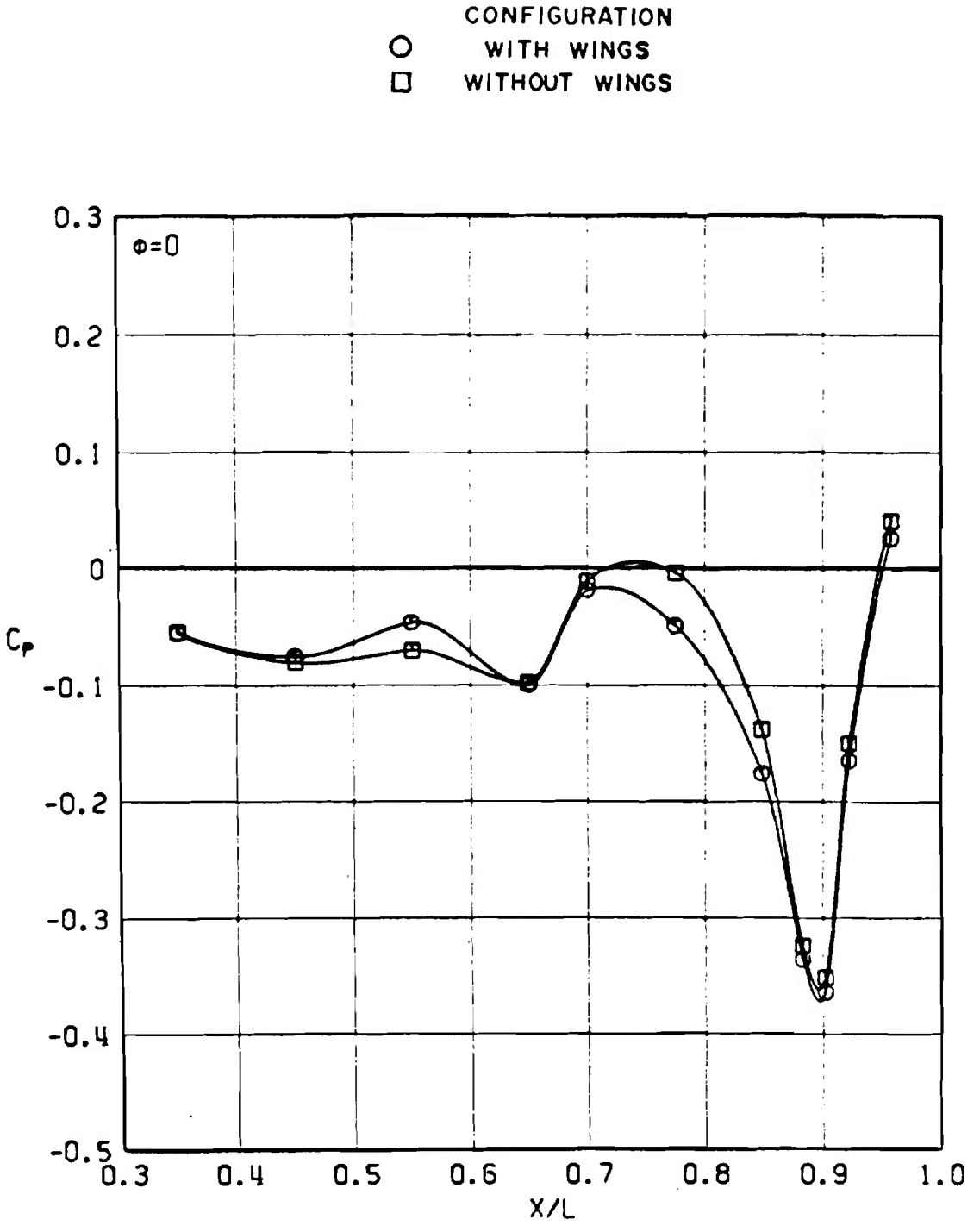

h. M_∞ = 1.20

Figure 48. Concluded.

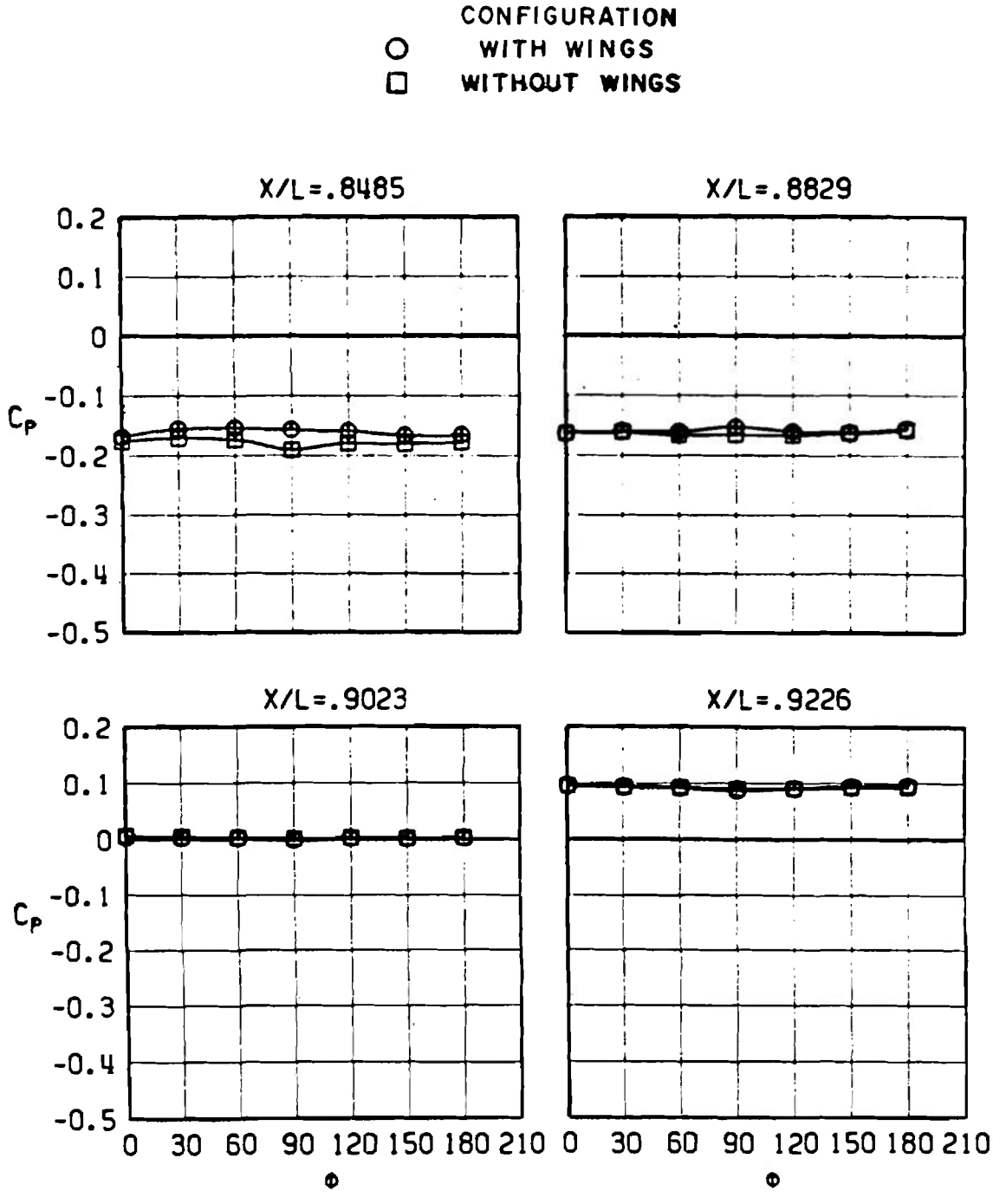

a. $M_\infty = 0.60$

Figure 49. Effect of wings on circumferential pressure distribution, 4.7-percent scale model, nominal characteristic Reynolds number, $\alpha = 0$.

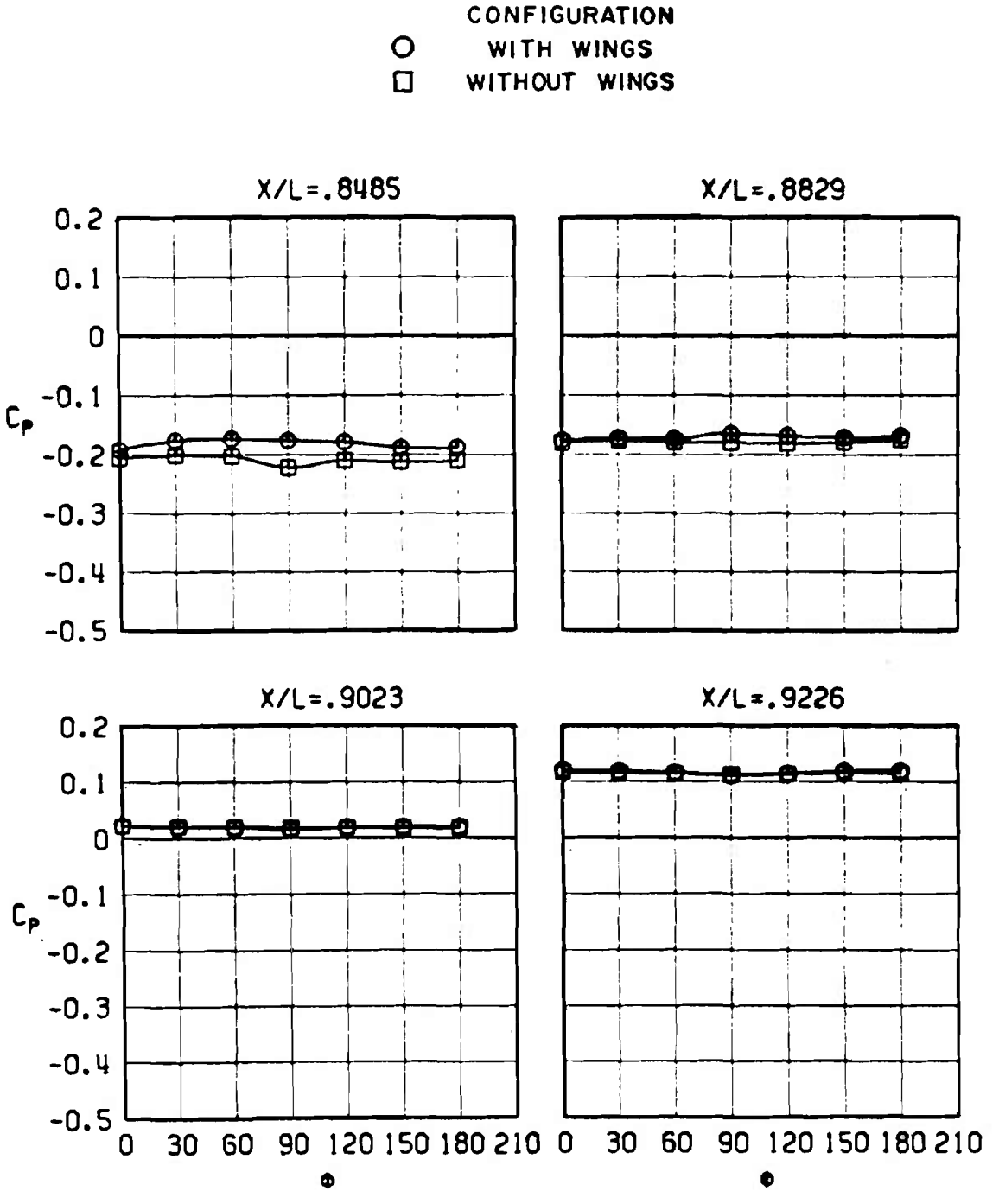

b. $M_\infty = 0.80$

Figure 49. Continued.

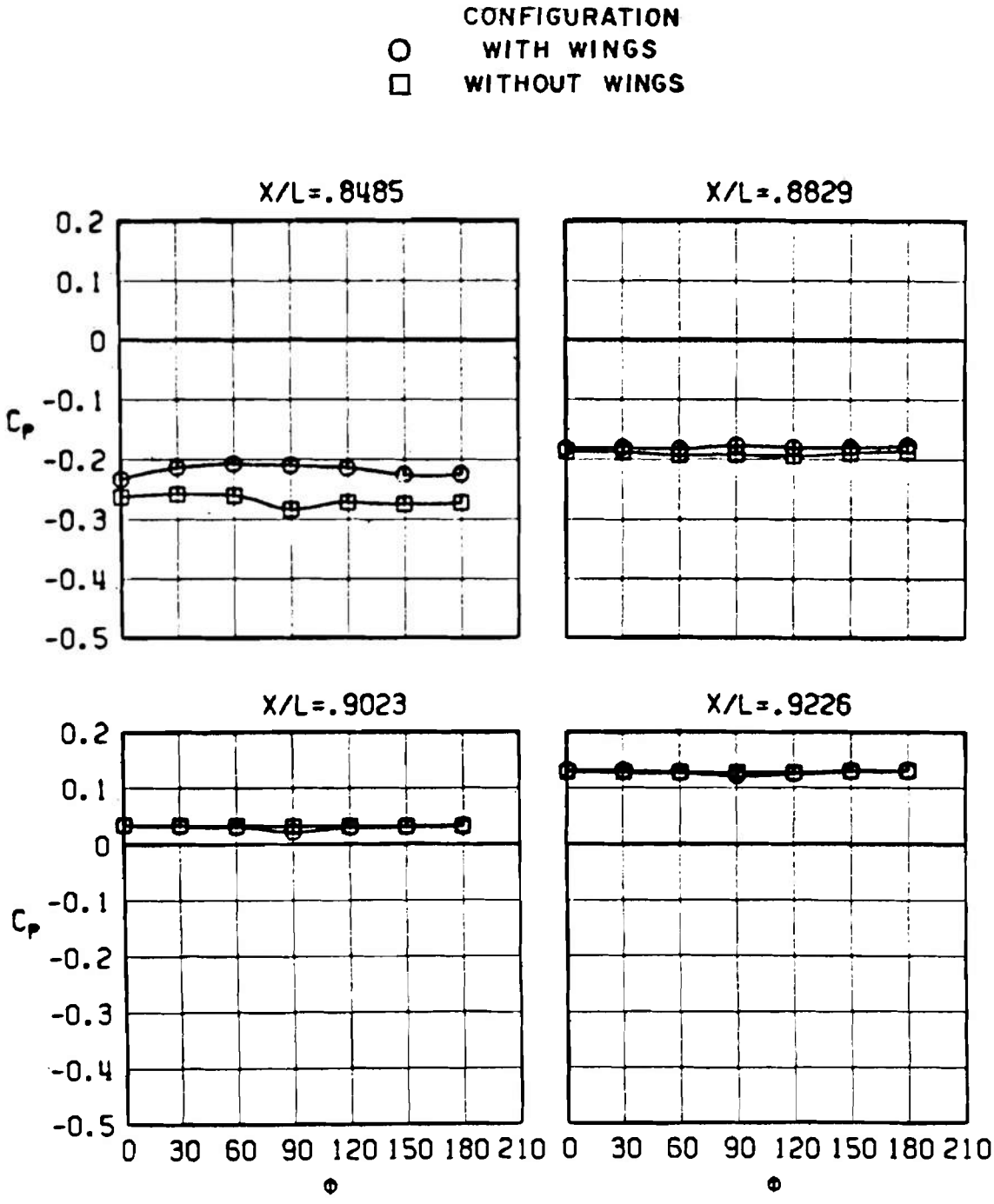

c. $M_\infty = 0.90$

Figure 49. Continued.

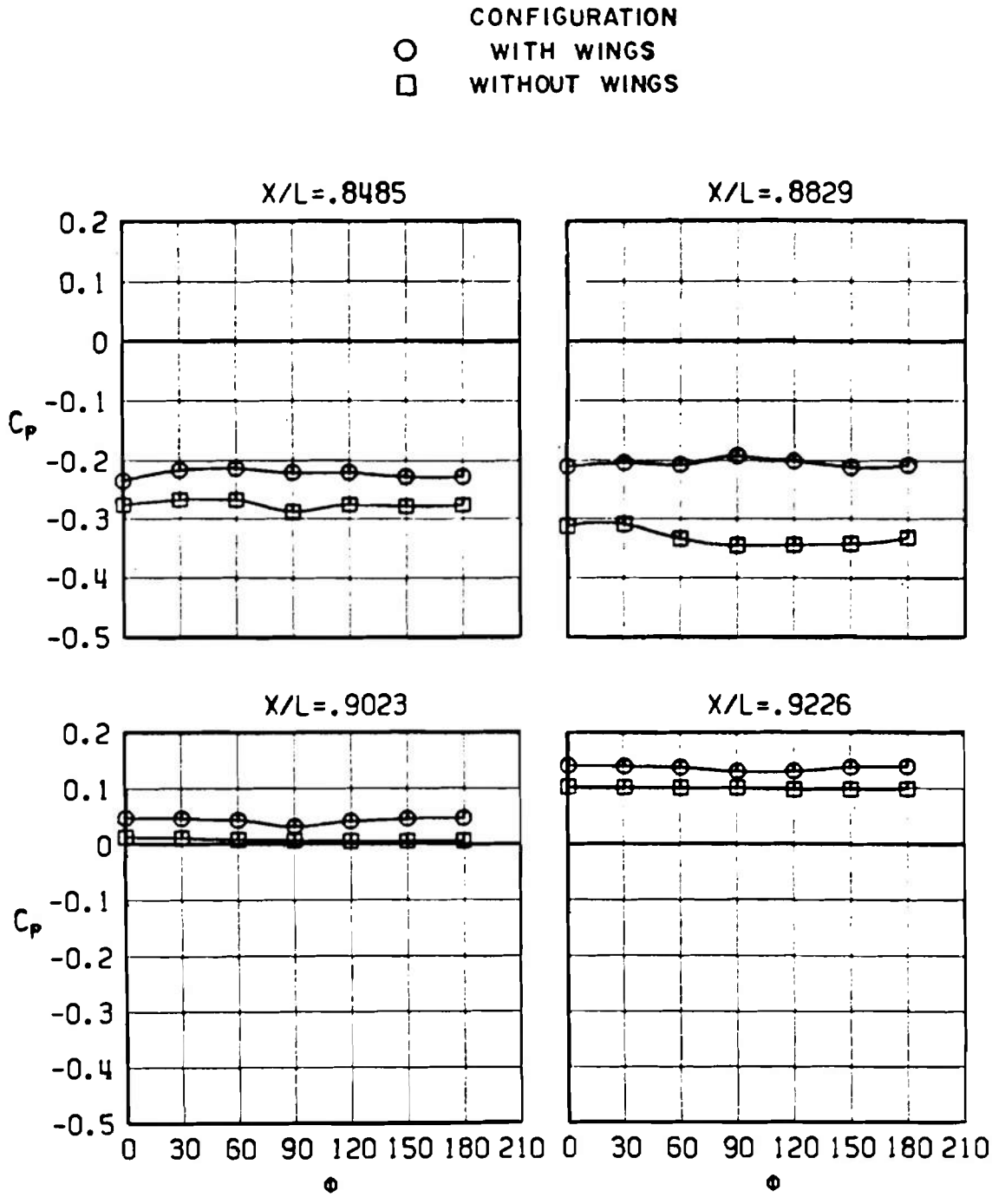

d. $M_\infty = 0.95$

Figure 49. Continued.

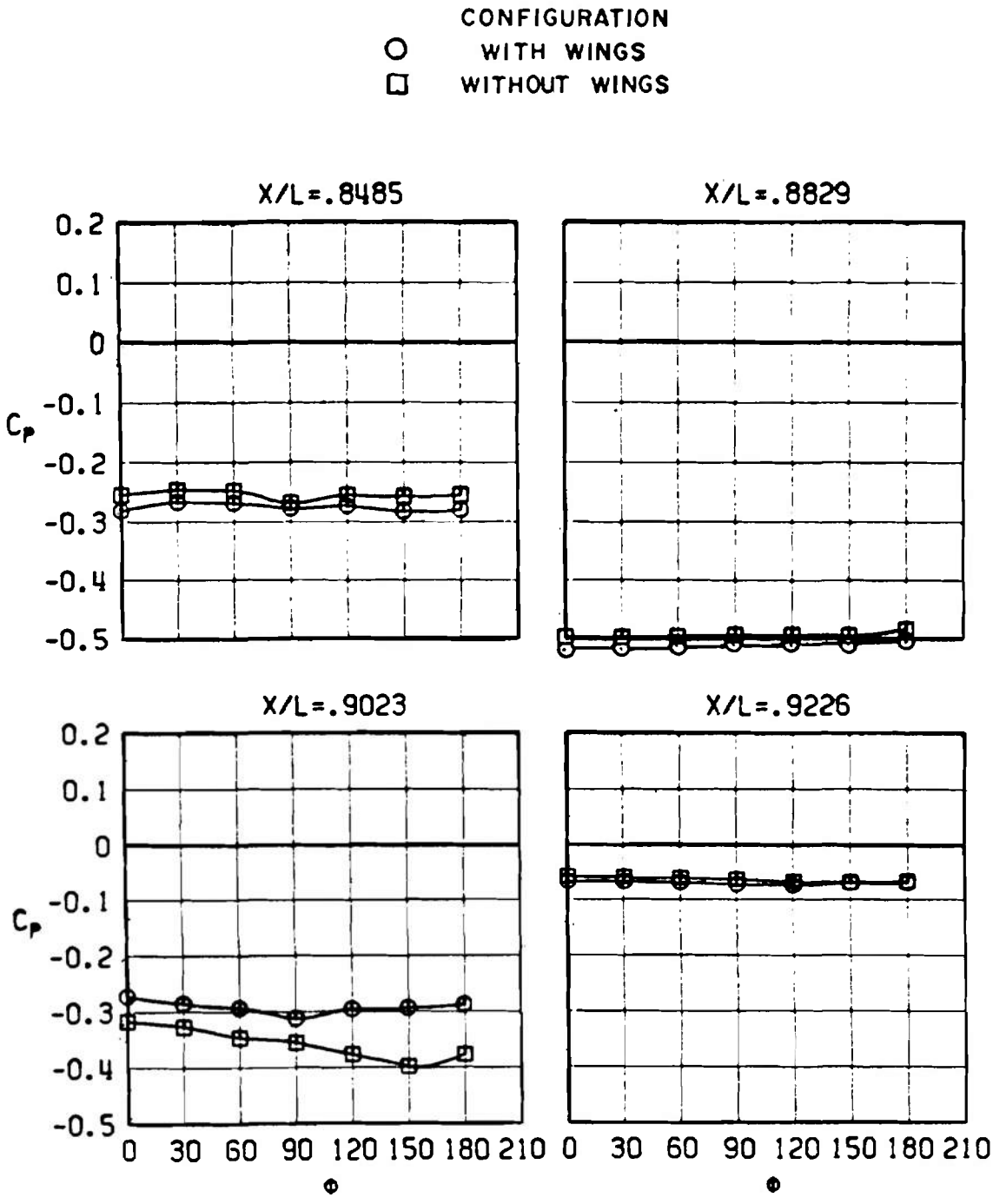

e. $M_\infty = 1.00$

Figure 49. Continued.

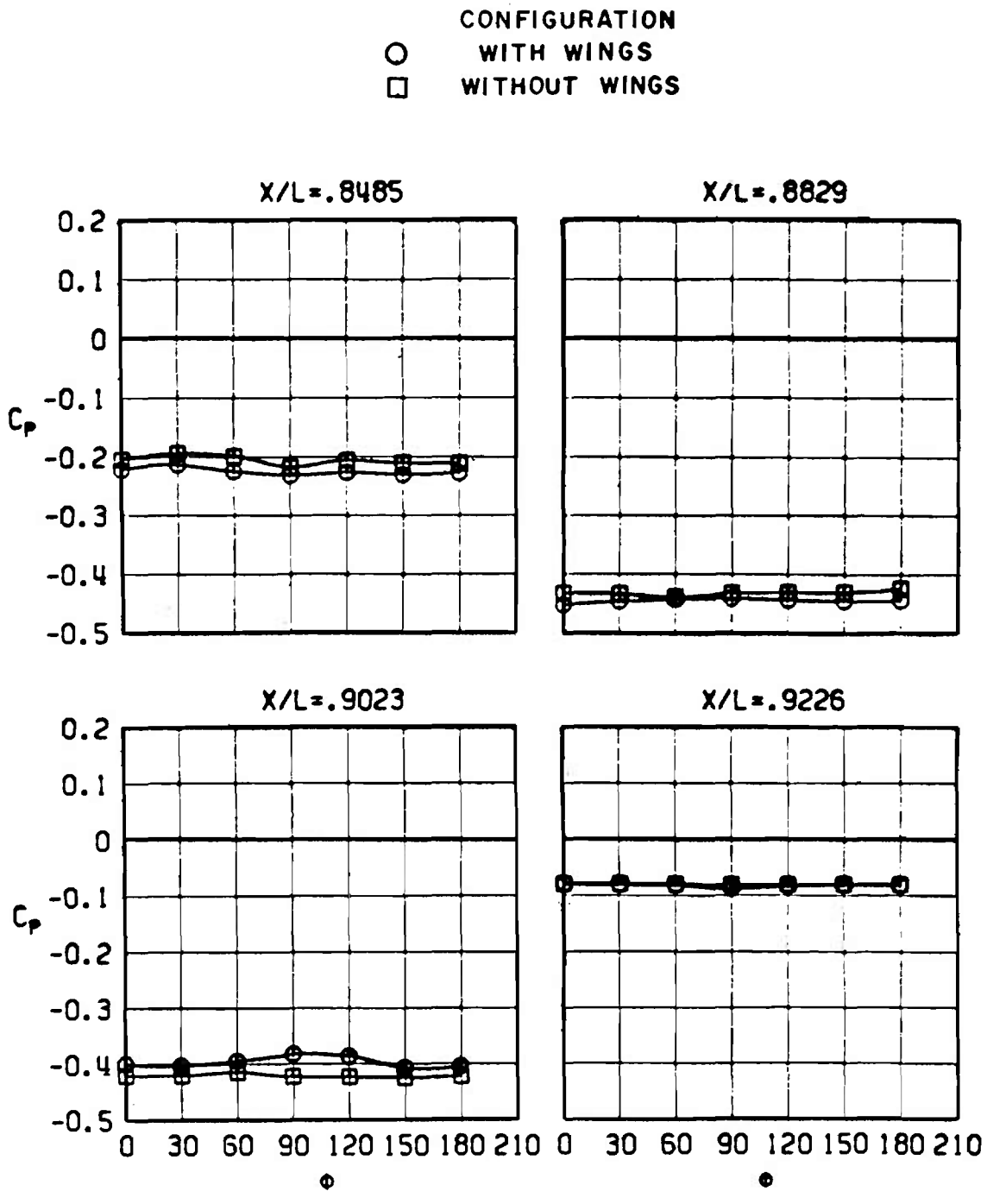

f. M_∞ = 1.05
Figure 49. Continued.

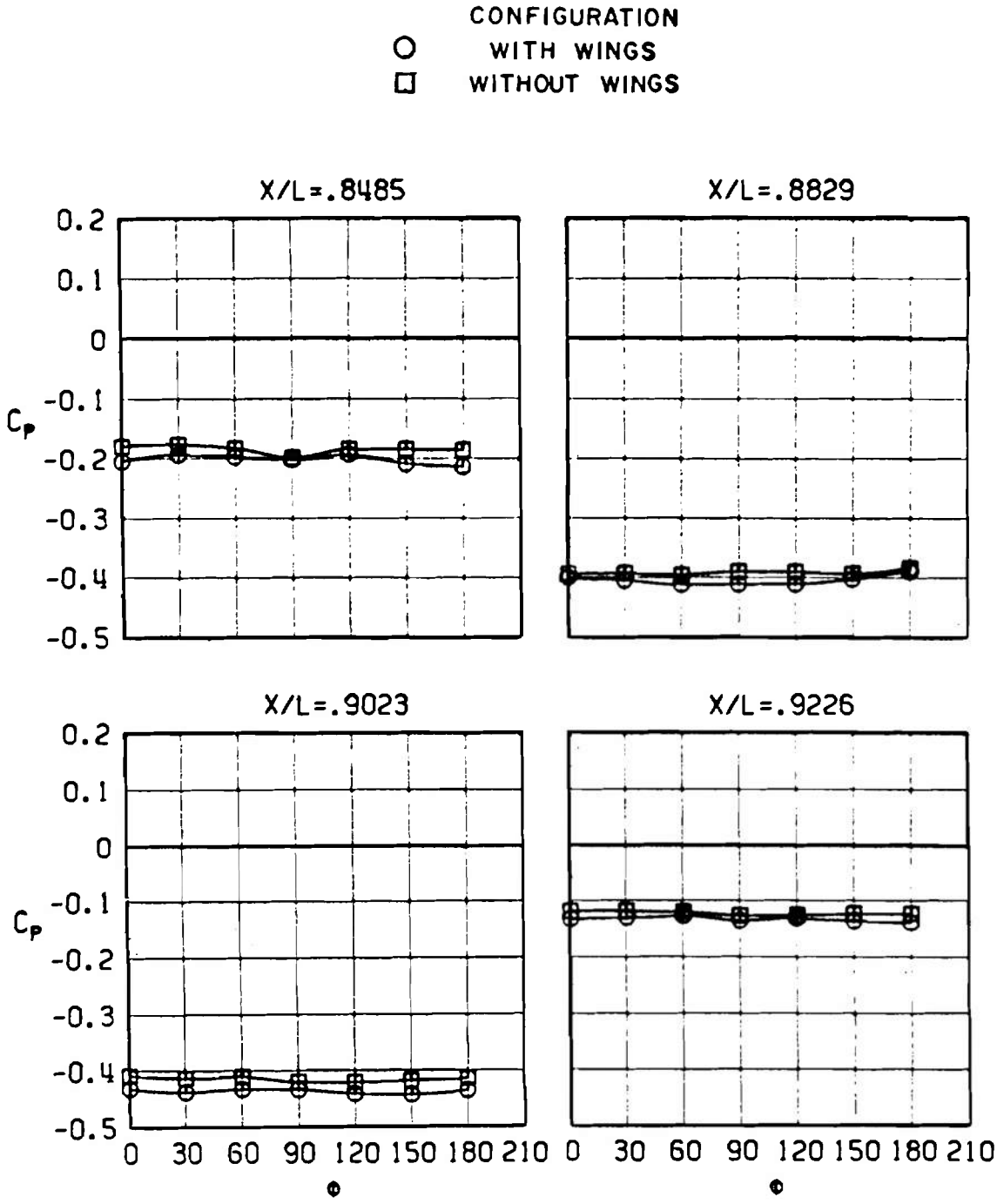

g. $M_\infty = 1.10$
Figure 49. Continued.

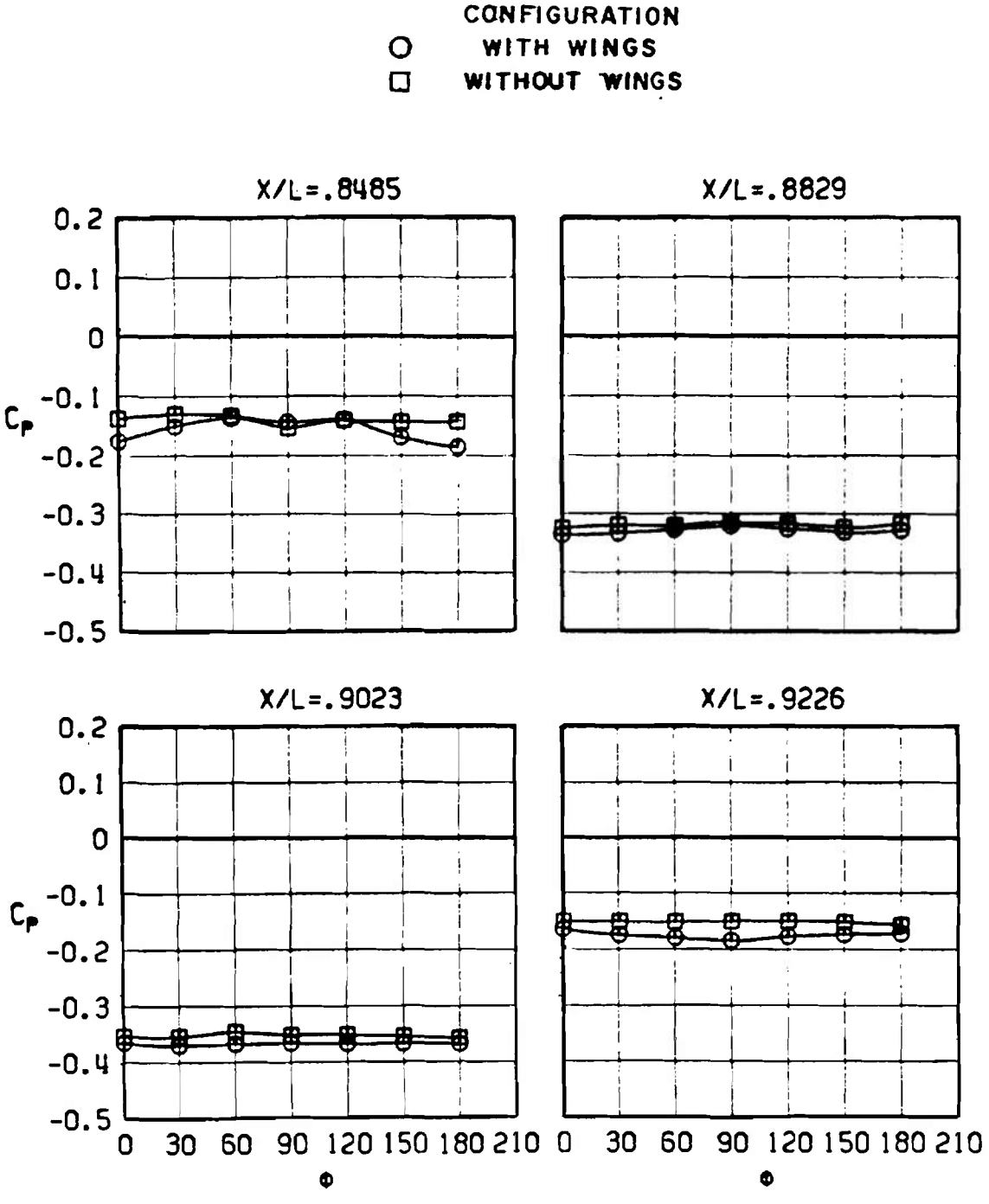

h. $M_\infty = 1.20$

Figure 49. Concluded.

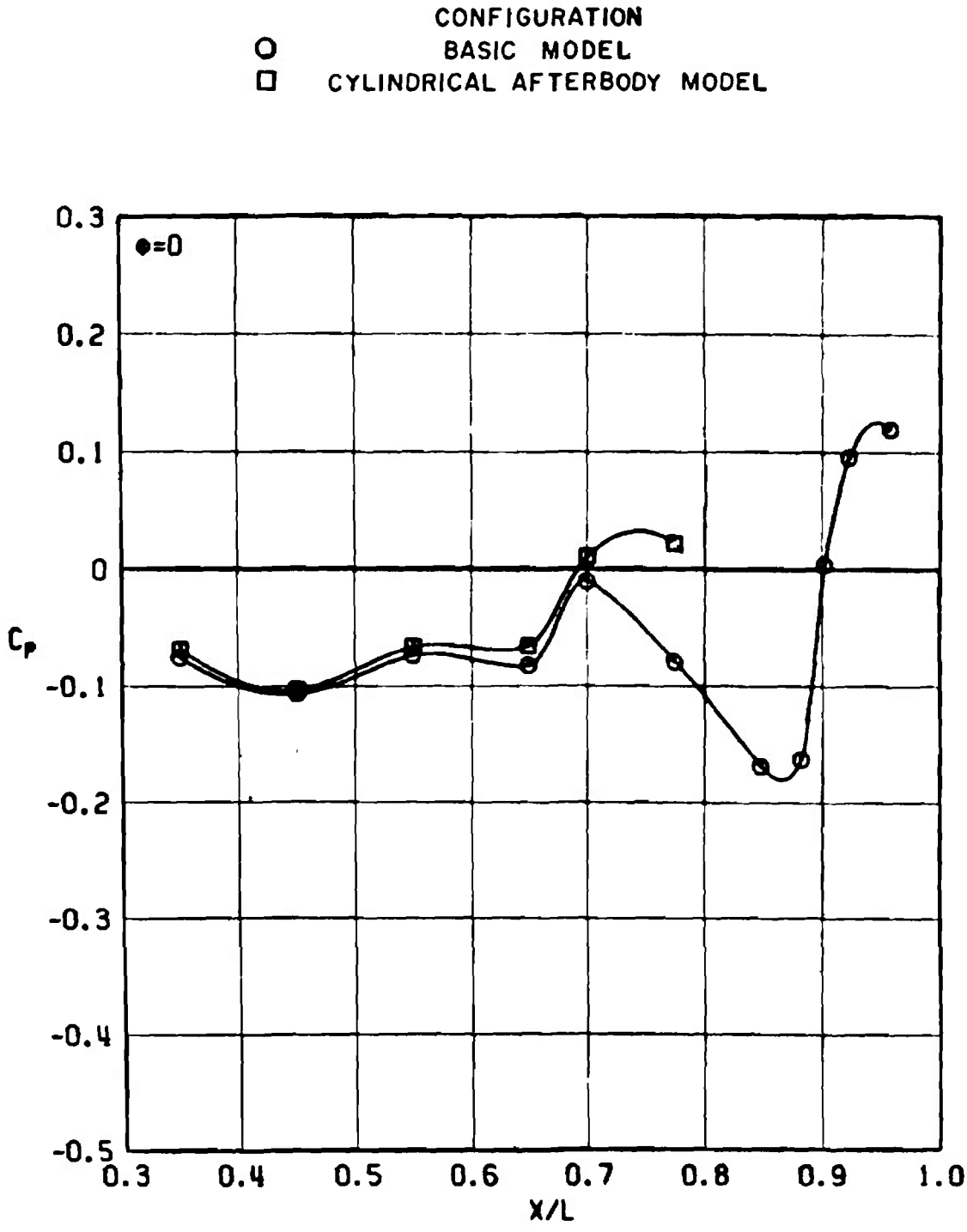

a. $M_\infty = 0.60$

Figure 50. Effect of cylindrical afterbody on top centerline pressure distribution, 4.7-percent scale model, nominal characteristic Reynolds number schedule, $\alpha = 0$.

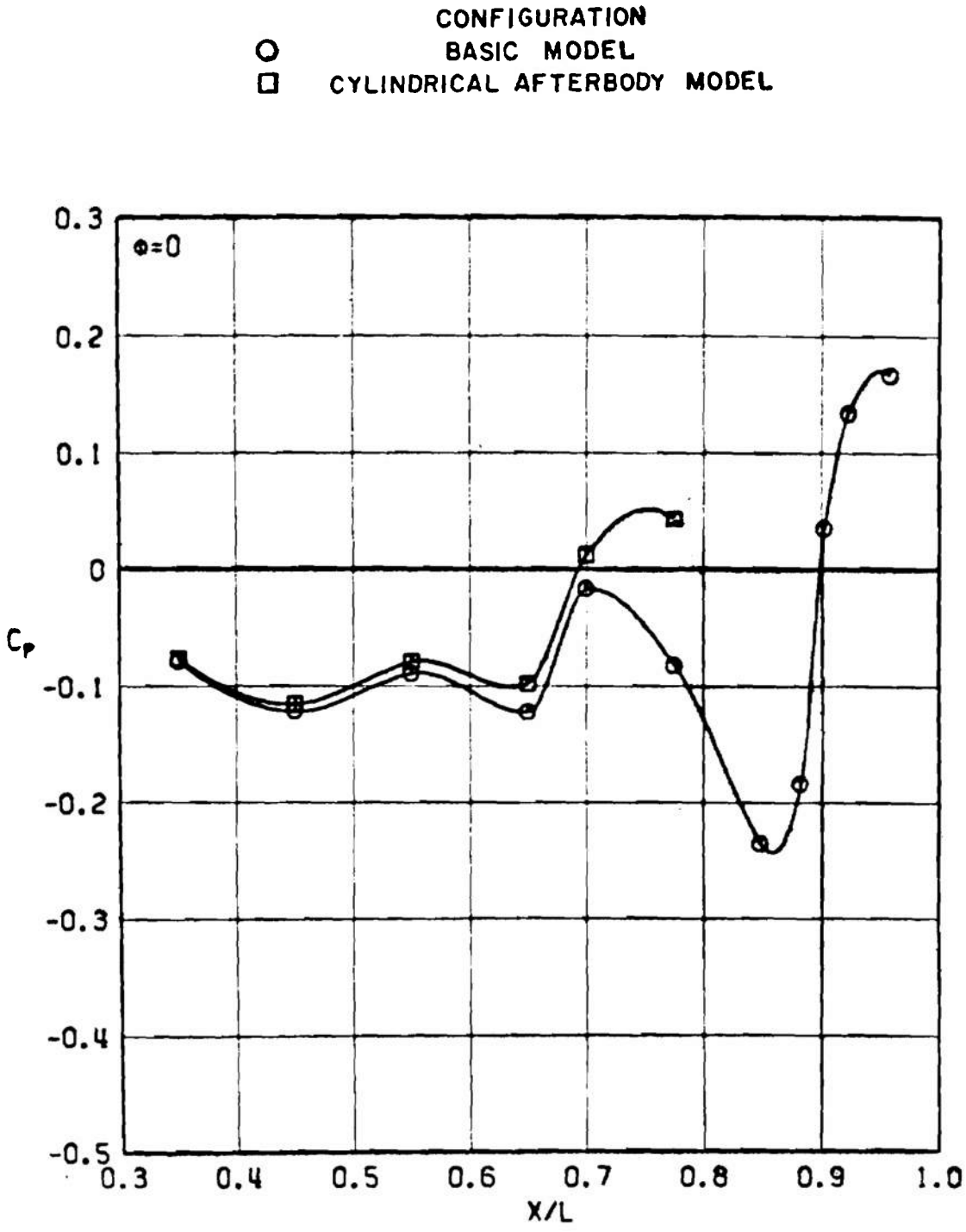

b. $M_\infty = 0.90$

Figure 50. Continued.

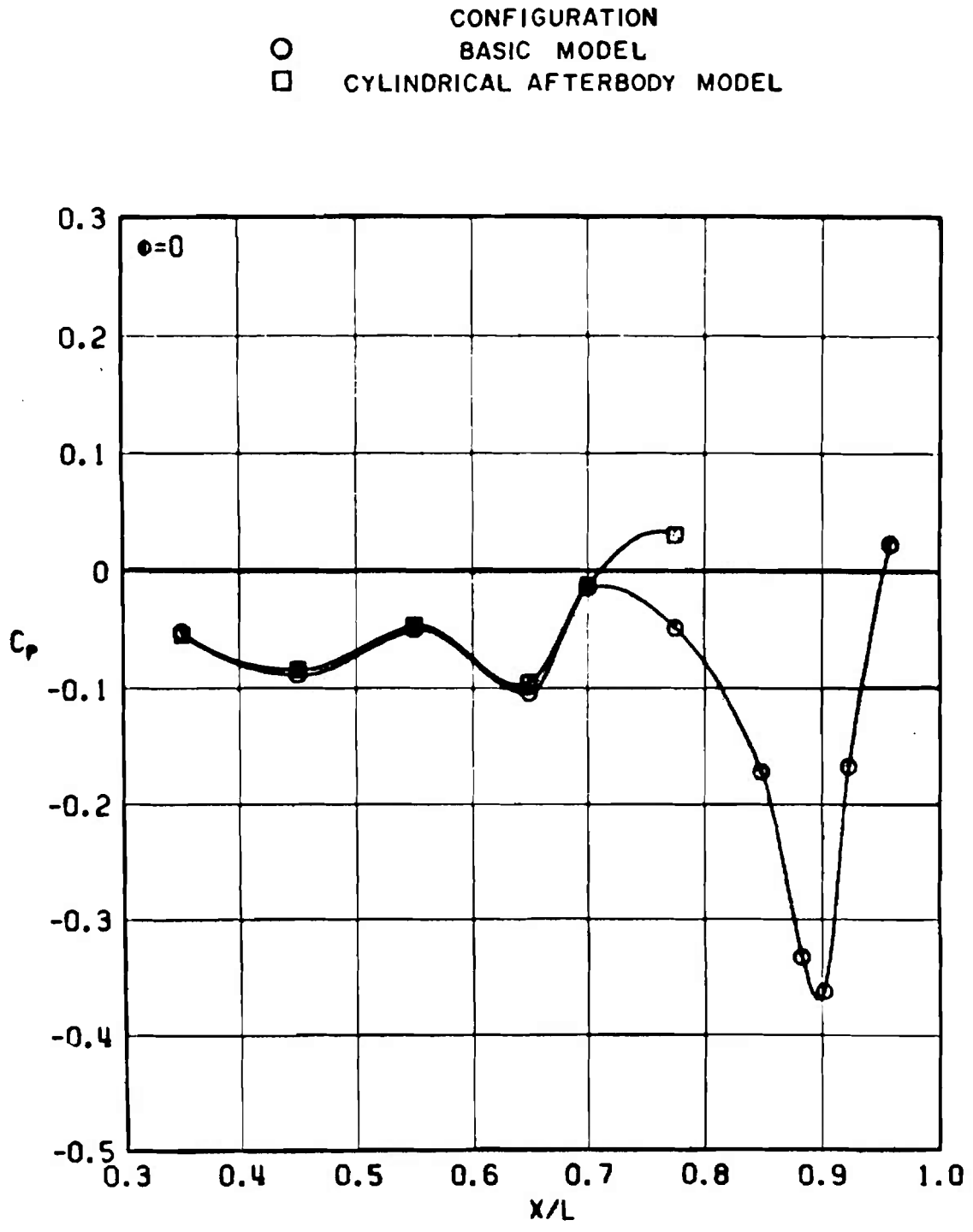

c. $M_\infty = 1.20$

Figure 50. Concluded.

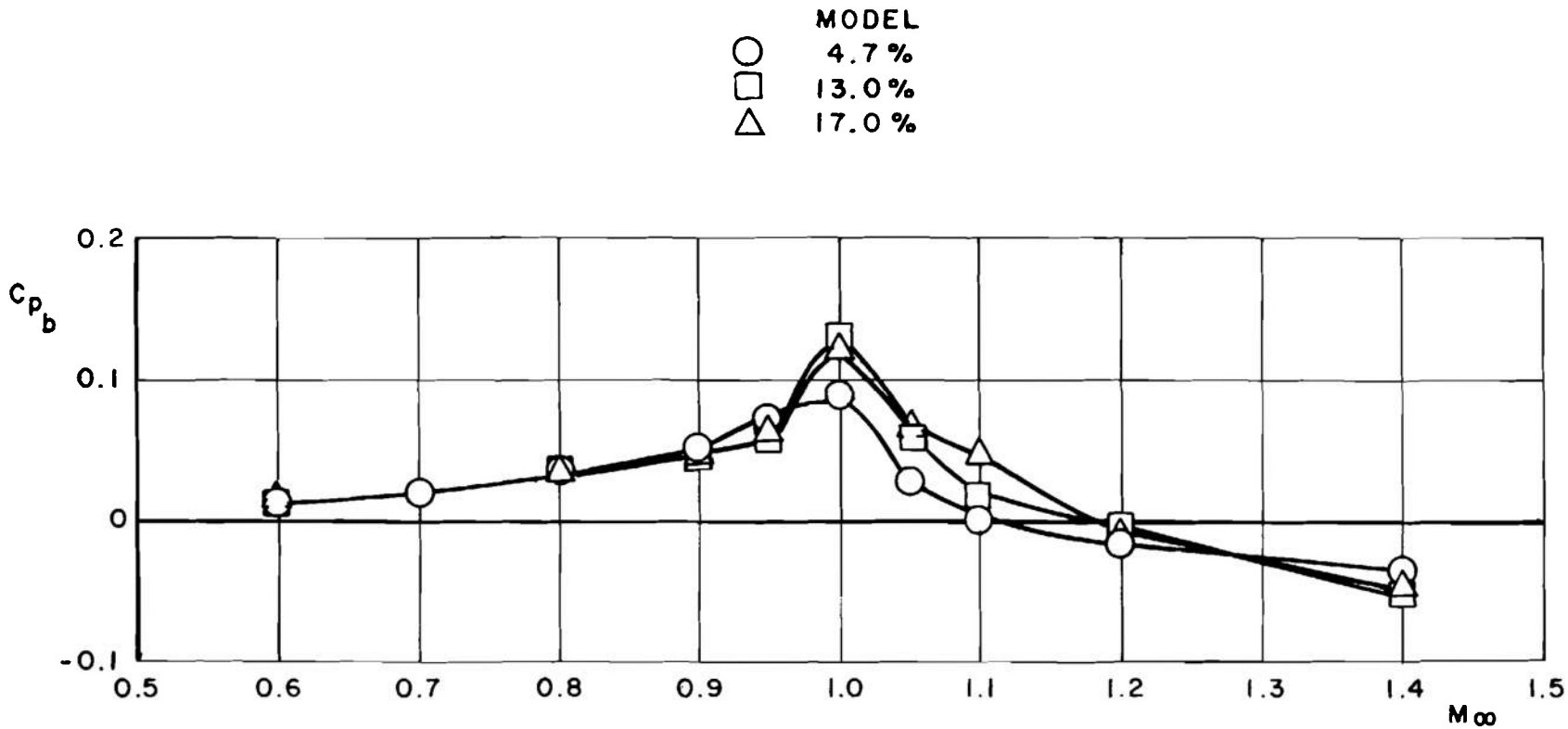

Figure 51. Base pressure coefficient for basic configuration.

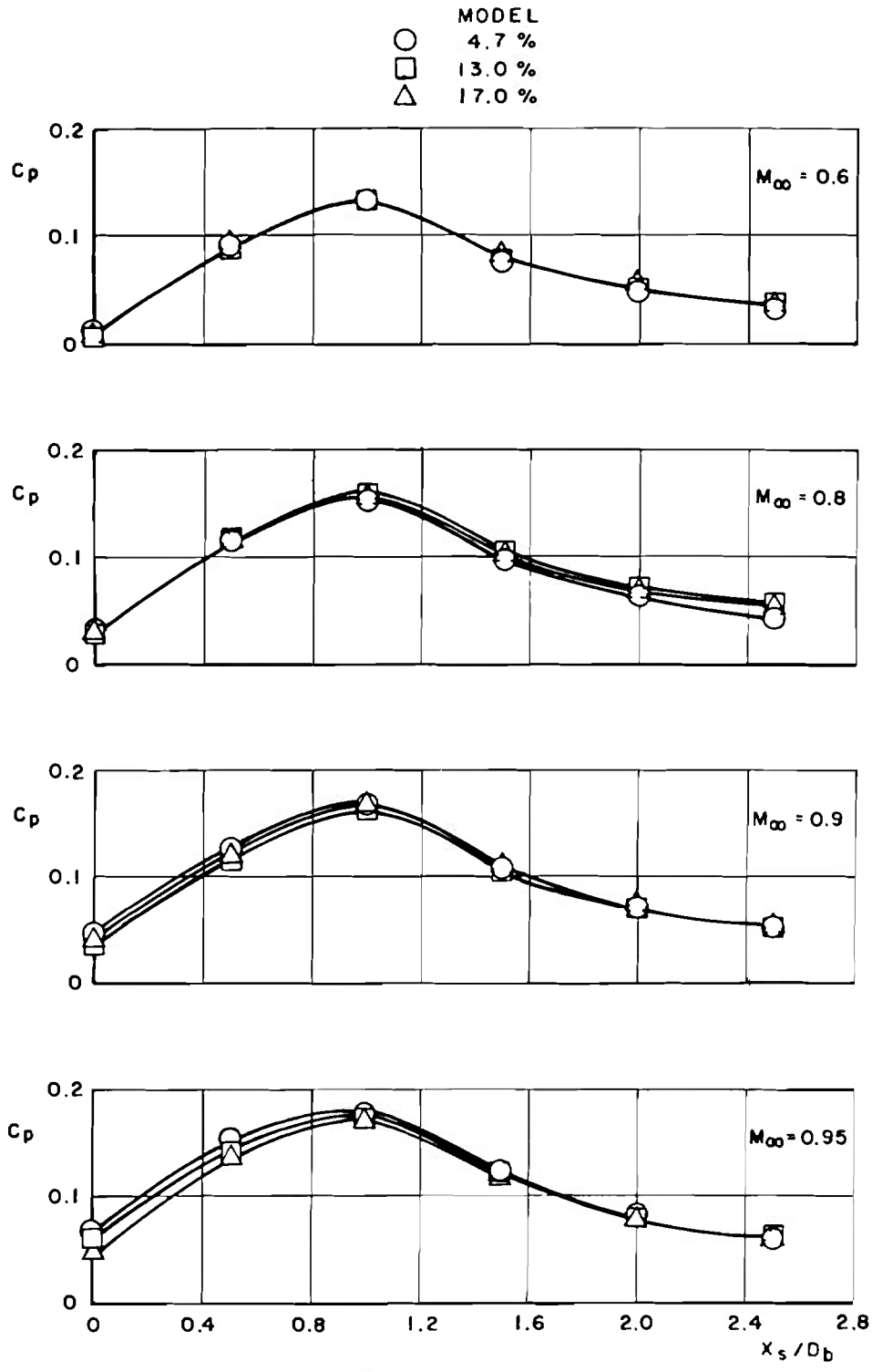

a. M_∞ = 0.6 to 0.95

Figure 52. Sting pressure distributions for basic configuration.

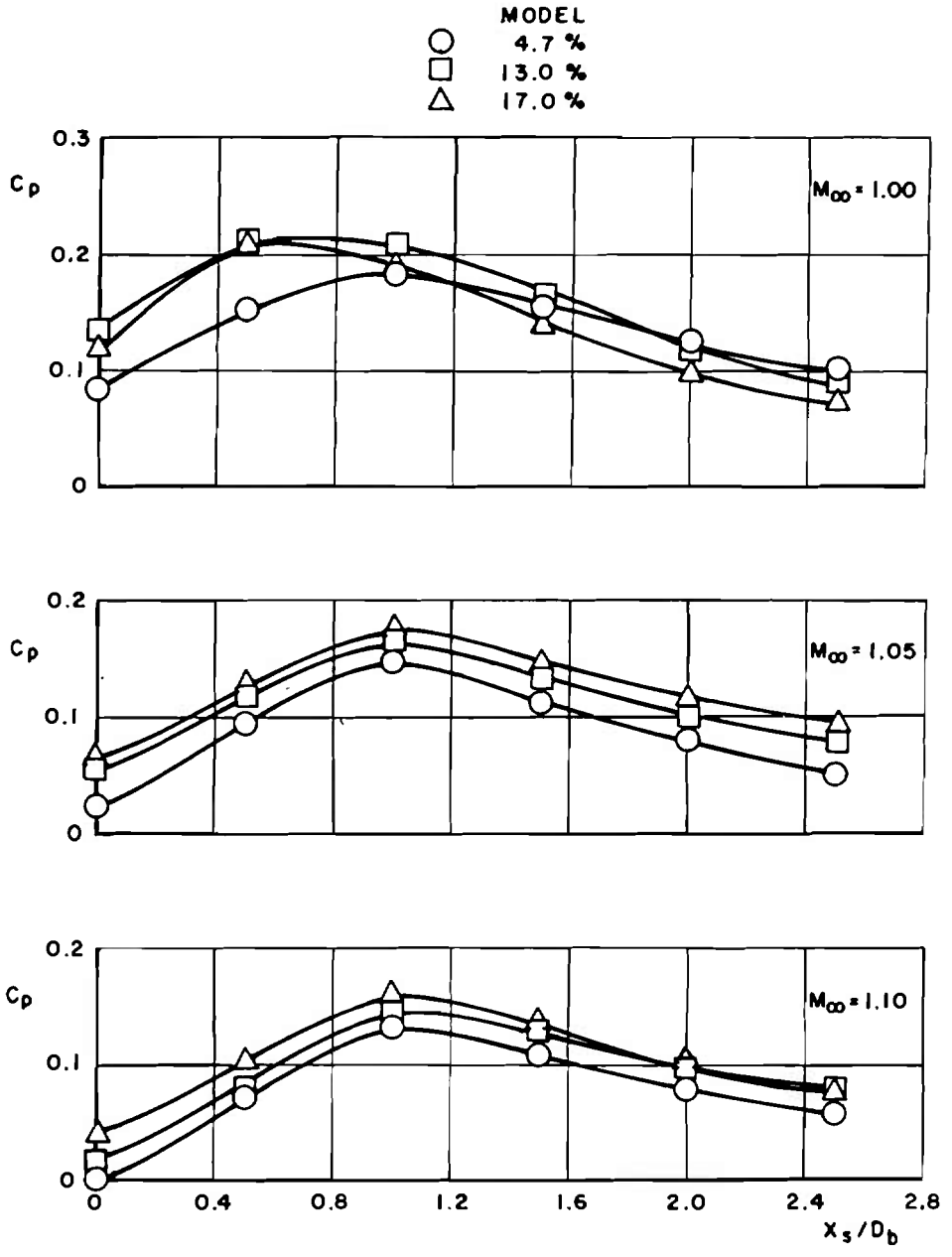

b. M_∞ = 1.00 to 1.10
Figure 52. Continued.

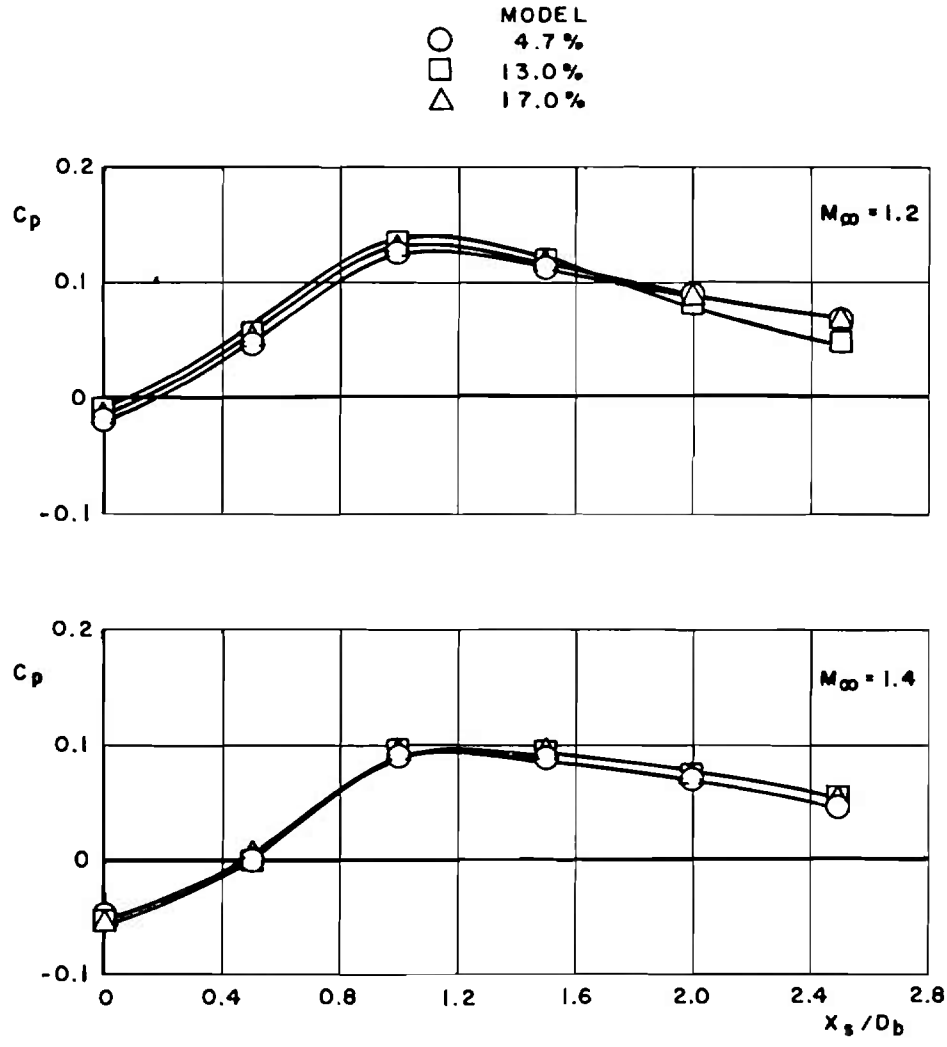

c. M_∞ = 1.2 and 1.4
Figure 52. Concluded.

Table 1. Radius Distribution of 17-percent Scale Model

NOTE: MS = Model Station, in.
RFUS = Radius of Fuselage, in.

MS	RFUS	MS	RFUS	MS	RFUS
19.769	0	---	---	---	---
20.060	0.1158	---	---	---	---
20.400	0.2501	34.000	3.6941	47.600	5.6236
20.740	0.3831	34.340	3.7380	47.940	5.6806
21.080	0.5147	34.680	3.7811	48.280	5.7364
21.420	0.6447	35.020	3.8234	48.620	5.7909
21.760	0.7731	35.360	3.8649	48.960	5.8443
22.100	0.8997	35.700	3.9059	49.300	5.8964
22.440	1.0244	36.040	3.9462	49.640	5.9474
22.780	1.1470	36.380	3.9859	49.980	5.9973
23.120	1.2674	36.720	4.0251	50.320	6.0461
23.460	1.3855	37.060	4.0638	50.660	6.0938
23.800	1.5011	37.400	4.1021	51.000	6.1404
24.140	1.6141	37.740	4.1407	51.340	6.1860
24.480	1.7243	38.080	4.1806	51.680	6.2306
24.820	1.8316	38.420	4.2216	52.020	6.2742
25.160	1.9360	38.760	4.2637	52.360	6.3168
25.500	2.0372	39.100	4.3068	52.700	6.3585
25.840	2.1354	39.440	4.3510	53.040	6.3993
26.180	2.2303	39.780	4.3963	53.380	6.4391
26.520	2.3219	40.120	4.4424	53.720	6.4782
26.860	2.4104	40.460	4.4895	54.060	6.5163
27.200	2.4957	40.800	4.5375	54.400	6.5537
27.540	2.5777	41.140	4.5863	54.740	6.5902
27.880	2.6568	41.480	4.6360	55.080	6.6259
28.220	2.7328	41.820	4.6864	55.420	6.6609
28.560	2.8060	42.160	4.7375	55.760	6.6952
28.900	2.8764	42.500	4.7893	56.100	6.7288
29.240	2.9442	42.840	4.8418	56.440	6.7616
29.580	3.0095	43.180	4.8949	56.780	6.7938
29.920	3.0725	43.520	4.9486	57.120	6.8253
30.260	3.1333	43.860	5.0028	57.460	6.8562
30.600	3.1921	44.200	5.0575	57.800	6.8865
30.940	3.2489	44.540	5.1127	58.140	6.9162
31.280	3.3040	44.880	5.1683	58.480	6.9453
31.620	3.3574	45.220	5.2242	58.820	6.9738
31.960	3.4092	45.560	5.2806	59.160	7.0018
32.300	3.4597	45.900	5.3372	59.500	7.0292
32.640	3.5089	46.240	5.3941	59.840	7.0562
32.980	3.5568	46.580	5.4512	60.180	7.0826
33.320	3.6036	46.920	5.5085	60.520	7.1086
33.660	3.6493	47.260	5.5660	60.860	7.1341

Table 1. Continued.

MS	RFUS	MS	RFUS	MS	RFUS
61.200	7.1591	78.200	8.0260	95.200	8.0566
61.540	7.1837	78.540	8.0332	95.540	8.0551
61.880	7.2079	78.880	8.0395	95.880	8.0531
62.220	7.2316	79.220	8.0452	96.220	8.0507
62.560	7.2550	79.560	8.0501	96.560	8.0479
62.900	7.2779	79.900	8.0545	96.900	8.0446
63.240	7.3005	80.240	8.0584	97.240	8.0410
63.580	7.3227	80.580	8.0618	97.580	8.0370
63.920	7.3446	80.920	8.0648	97.920	8.0327
64.260	7.3660	81.260	8.0674	98.260	8.0280
64.600	7.3872	81.600	8.0697	98.600	8.0229
64.940	7.4081	81.940	8.0717	98.940	8.0175
65.280	7.4286	82.280	8.0734	99.280	8.0117
65.620	7.4488	82.620	8.0748	99.620	8.0055
65.960	7.4687	82.960	8.0761	99.960	7.9990
66.300	7.4883	83.300	8.0771	100.300	7.9922
66.640	7.5076	83.640	8.0780	100.640	7.9849
66.980	7.5267	83.980	8.0787	100.980	7.9773
67.320	7.5454	84.320	8.0792	101.320	7.9693
67.660	7.5640	84.660	8.0796	101.660	7.9608
68.000	7.5823	85.000	8.0798	102.000	7.9519
68.340	7.6003	85.340	8.0800	102.340	7.9426
68.680	7.6181	85.680	8.0800	102.680	7.9327
69.020	7.6356	86.020	8.0799	103.020	7.9223
69.360	7.6530	86.360	8.0797	103.360	7.9114
69.700	7.6701	86.700	8.0795	103.700	7.8998
70.040	7.6870	87.040	8.0792	104.040	7.8875
70.380	7.7037	87.380	8.0788	104.380	7.8743
70.720	7.7201	87.720	8.0783	104.720	7.8602
71.060	7.7364	88.060	8.0777	105.060	7.8450
71.400	7.7525	88.400	8.0771	105.400	7.8282
71.740	7.7684	88.740	8.0765	105.740	7.8113
72.080	7.7842	89.080	8.0757	106.080	7.7954
72.420	7.7997	89.420	8.0750	106.420	7.7802
72.760	7.8151	89.760	8.0742	106.760	7.7656
73.100	7.8303	90.100	8.0733	107.100	7.7514
73.440	7.8453	90.440	8.0724	107.440	7.7376
73.780	7.8602	90.780	8.0715	107.780	7.7242
74.120	7.8750	91.120	8.0705	108.120	7.7111
74.460	7.8895	91.460	8.0695	108.460	7.6984
74.800	7.9040	91.800	8.0685	108.800	7.6860
75.140	7.9182	92.140	8.0674	109.140	7.6740
75.480	7.9324	92.480	8.0663	109.480	7.6623
75.820	7.9464	92.820	8.0652	109.820	7.6509
76.160	7.9603	93.160	8.0640	110.160	7.6400
76.500	7.9740	93.500	8.0629	110.500	7.6295
76.840	7.9870	93.840	8.0617	110.840	7.6195
77.180	7.9985	94.180	8.0604	111.180	7.6102
77.520	8.0088	94.520	8.0592	111.520	7.6018
77.860	8.0179	94.860	8.0579	111.860	7.5948

Table 1. Concluded.

MS	RFUS	MS	RFUS	MS	RFUS
112.200	7.5910	129.200	7.2947	146.200	4.4939
112.540	7.5910	129.540	7.2733	146.540	4.4622
112.880	7.5909	129.880	7.2504	146.880	4.4323
113.220	7.5908	130.220	7.2259	147.220	4.4043
113.560	7.5906	130.560	7.1995	147.560	4.3782
113.900	7.5904	130.900	7.1710	147.900	4.3542
114.240	7.5901	131.240	7.1403	148.240	4.3323
114.580	7.5897	131.580	7.1072	148.580	4.3126
114.920	7.5893	131.920	7.0713	148.920	4.2952
115.260	7.5888	132.260	7.0326	149.260	4.2802
115.600	7.5883	132.600	6.9907	149.600	4.2678
115.940	7.5877	132.940	6.9455	149.822	4.2678
116.280	7.5869	133.280	6.8967		
116.620	7.5862	133.620	6.8441		
116.960	7.5853	133.960	6.7877		
117.300	7.5843	134.300	6.7273		
117.640	7.5833	134.640	6.6628		
117.980	7.5821	134.980	6.5943		
118.320	7.5808	135.320	6.5218		
118.660	7.5794	135.660	6.4453		
119.000	7.5779	136.000	6.3651		
119.340	7.5763	136.340	6.2813		
119.680	7.5744	136.680	6.1942		
120.020	7.5724	137.020	6.1038		
120.360	7.5703	137.360	6.0147		
120.700	7.5679	137.700	5.9249		
121.040	7.5652	138.040	5.8461		
121.380	7.5623	138.380	5.7657		
121.720	7.5591	138.720	5.6840		
122.060	7.5555	139.060	5.6037		
122.400	7.5490	139.400	5.5271		
122.740	7.5420	139.740	5.4539		
123.080	7.5336	140.080	5.3837		
123.420	7.5240	140.420	5.3164		
123.760	7.5141	140.760	5.2516		
124.100	7.5031	141.100	5.1893		
124.440	7.4933	141.440	5.1293		
124.780	7.4831	141.780	5.0715		
125.120	7.4726	142.120	5.0158		
125.460	7.4615	142.460	4.9621		
125.800	7.4500	142.800	4.9104		
126.140	7.4379	143.140	4.8607		
126.480	7.4252	143.480	4.8127		
126.820	7.4119	143.820	4.7666		
127.160	7.3979	144.160	4.7223		
127.500	7.3832	144.500	4.6798		
127.840	7.3675	144.840	4.6391		
128.180	7.3510	145.180	4.6001		
128.520	7.3334	145.520	4.5630		
128.860	7.3146	145.860	4.5276		

NOMENCLATURE

A	Model cross-sectional area
A_{BASE}	Model base area, ft^2
A_{MAX}	Maximum cross-sectional area of model, fuselage plus wings, ft^2
A_{TUNNEL}	Cross-sectional area of test section, ft^2
b	Wing span, ft
C_{AF}	Axial-force coefficient
C_D	Drag coefficient
C_{DF}	Friction drag coefficient
C_{DFF}	Fuselage friction drag coefficient
C_{DFW}	Wing friction drag coefficient
C_{DMF}	Measured drag coefficient minus total friction drag coefficient, $C_D - C_{DF}$
$C_{D_{PAFT}}$	Aft-end pressure drag coefficient
C_m	Pitching-moment coefficient
C_{m_α}	Pitching-moment curve slope
C_N	Normal-force coefficient
C_{N_α}	Normal-force curve slope
C_p	Local pressure coefficient
C_{p_b}	Average base pressure coefficient
$\bar{c}$	Mean aerodynamic chord, ft
D_b	Model base diameter, ft
D_s	Sting diameter at model exit plane, ft
k	Grit particle height, in.

L	Length of model, ft
M_∞	Free-stream Mach number
p_∞	Free-stream static pressure, psfa
q_∞	Free-stream dynamic pressure, psf
R	Radius of fuselage, ft
R_e	Unit Reynolds number, ft^{-1}
R_{e_L}	Characteristic Reynolds number, based on model length
S	Wing reference area, ft^2
t	Wing thickness, ft
V_f	Fuselage probe boundary-layer velocity, ft/sec
V_w	Wing probe boundary-layer velocity, ft/sec
V_1	Velocity at the boundary-layer free-stream edge, ft/sec
X	Length along model centerline from fuselage nose, ft
X_s	Length along sting from model exit plane, ft
y	Boundary-layer rake probe height, measured from surface, ft
α	Model angle of attack, deg
ϕ	Circumferential position of pressure tap location with respect to top of fuselage, deg